PREDICTION OF LONG-TERM CREEP FOR NUCLEAR CONCRETE STRUCTURES

A Dissertation

by

AISHWARYA BARANIKUMAR

Submitted to the Office of Graduate and Professional Studies of
Texas A&M University
in partial fulfillment of the requirements for the degree of

DOCTOR OF PHILOSOPHY

Chair of Committee,	Zachary Grasley
Committee Members,	Dan Zollinger
	Joseph Bracci
	Chandler Benjamin
Head of Department,	Robin Autenrieth

December 2020

Major Subject: Civil Engineering

ABSTRACT

Creep is a long-term deformation that can cause redistribution of stresses, large deformations and prestress or post-tensioning losses in prestressed or post-tensioned structures, respectively. A major challenge in quantifying the effect of creep in concrete structures is that creep of concrete is known to continue for decades. Additionally, concrete creep research in the past, has focused primarily on uniaxial response. However, in biaxially prestressed concrete structures, multiaxial stress state can complicate the behavior of the viscoelastic material. Significant creep strains may be induced in directions transverse to each principle stress due to Poisson's effect. In this dissertation, a unique, miniature version of the standardized concrete creep frame is designed that is amenable to placing in climate chambers and temperature ovens. This enables the use of the time-temperature superposition principle to predict long-term basic creep of mature portland cement mortar from short-term creep experiments conducted at multiple elevated temperatures. The 3D basic creep response of mature cement mortar is examined using the miniaturized confined compression creep test that allows direct determination of the full stress and infinitesimal strain tensors in a single test, which enables the determination of Viscoelastic Poisson's Ratio (VPR). The VPR and the basic creep compliance of cement mortar can be used to upscale to concrete creep using advanced computational composite models. To validate the model, few concrete creep tests are conducted at room and elevated temperatures. The primary finding from this dissertation is that a basic creep compliance master curve of cement mortar can be developed for nearly 60 years at 20°C using experimental creep data obtained at higher temperatures for test durations of 600

days. From the confined compression experiment, the VPR of sealed, mature cement mortar is found to be nearly constant and equal to the elastic at room temperature, while the VPR gradually increases with time when measured at 60°C. Excellent agreement between the upscaled simulated concrete creep and experimental data was found for a period of 25 years.

DEDICATION

To my husband, Narain,

for his support, care and love

and to our kids, Avyukth and Advik

for giving us a world full of happiness.

ACKNOWLEDGEMENTS

First and foremost, I would like to thank my academic advisor, Dr. Zachary Grasley for giving me an opportunity to work with him and mentoring me throughout the program. He has always motivated and supported me in my professional as well as personal life. Under his guidance, I have learnt to make right engineering judgments, academic integrity, and confidence to deal with any challenges on the way.

I would like to express my sincere thanks to my committee members, Dr. Joseph Bracci, Dr. Dan Zollinger and Dr. Chandler Benjamin for their time and valuable comments throughout the course of this research. It was my pleasure to interact with each of them and have them on my committee.

I would also like to thank my research team members, Christa Torrence and Xijun Shi without whom I would not have been able to complete this project. They have been excellent team player and always willing to help me when needed. I thank all my teachers at Texas A&M University for transferring their knowledge and educating me achieve high quality of work in my studies. Thanks to Knife River for providing materials and aggregates for use in this research.

Finally, I would like to thank my entire family for their affection, patience and encouragement throughout my graduate studies. Special love to my mom and dad who have inspired me to become what I am today.

CONTRIBUTORS AND FUNDING SOURCES

Contributors

This work was supervised by a dissertation committee consisting of Dr. Zachary Grasley, Dr. Joseph Bracci and Dr. Dan Zollinger of the Department of Civil & Environmental Engineering and Dr. Chandler Benjamin of the Department of Mechanical Engineering.

The mix design for Section 2.4.1 and 4.2.1 was provided by Électricité de France (EDF). I am grateful to Dr. Jeffery Bullard of the Department of Civil & Environmantal Engineering for providing his insights on the activation energy discussion presented in section 2.7.1.

All other work conducted for the dissertation was completed by the student independently.

Funding Sources

Graduate study was funded by U.S. Department of Energy (DOE) Nuclear Energy University Programs (NEUP) and Oak Ridge National Lab in support of project 16-10457, “Experimentally Validated Computational Modeling of Creep and Creep-Cracking for Nuclear Concrete Structures”. Its contents are solely the responsibility of the authors and do not necessarily represent the official views of the DOE or Oak Ridge National Lab.

NOMENCLATURE

a/c	aggregate to cement content
B	dilatational compliance
β_{Ts} , β_{Th}	Arrhenius factors
β_{Tc}	shift factor
c	cement content
C_0	basic creep compliance
C_d	drying creep compliance
D	effective cross-section thickness
E	Young's modulus
E^c	Young's modulus of stainless steel
E_i	spring constants
ε_0	initial applied strain
ε_{au}	autogenous shrinkage
ε^f	free shrinkage strain
ε_h	hoop strain
ε_{kk}	volumetric strain
ε_{rr}	radial strain
ε_{sh}	drying shrinkage
$\varepsilon_{\theta\theta}$	tangential strain
ε_{zz}	axial strain
f'_c	compressive strength
G	shear modulus
γ_e	effective shear strain
h	relative humidity
H(t)	Heaviside or unit step function
J	uniaxial creep compliance
K	bulk modulus

L	deviatoric compliance
μ_i	viscosity of dashpots
υ	Poisson's ratio
υ^c	Poisson's ratio of stainless steel
R	universal gas constant
R_T	multiplicative factor
ρ	density
σ_0	initial applied stress
σ_{kk}	volumetric stress
σ_m	mean (dilatational) stress
σ_{rr}	radial stress
$\sigma_{\theta\theta}$	tangential stress
σ_{zz}	axial stress
s	transform variable in Laplace domain
t	present age
t'	age at loading
t_0	age when drying starts
T	temperature
τ_e	effective shear stress
τ_i	retardation times
τ_m	relaxation times
τ_{sh}	shrinkage half-time
u_r	radial displacement
U_c	activation energy
w	water content
w/c	water to cement ratio
v/s	volume to surface area ratio

TABLE OF CONTENTS

Page

LIST OF FIGURES

Page

LIST OF TABLES

Page

1. INTRODUCTION

1.1. Problem Statement

The United States (US) currently has 97 nuclear power plants in operation, which contribute to nearly 20 percent of the national electricity requirements. Due to the demand for energy and the need to reduce carbon emissions, there is a request to increase the design life of nuclear power plants (U.S. Energy Information Administration, 2017). Nuclear power plants have an initial 40-year design life, with the ability to renew the license for an additional 20 years with approval from Nuclear Regulatory Commission (NRC). There is also a provision to renew the second license extending the operating life of nuclear facilities to 80 years. With more than 50% of the nuclear power plants operating past their original design life, it is important to evaluate long-term structural integrity of these aging structures. Figure 1-1 shows the number of operating nuclear power plants and their current ages.

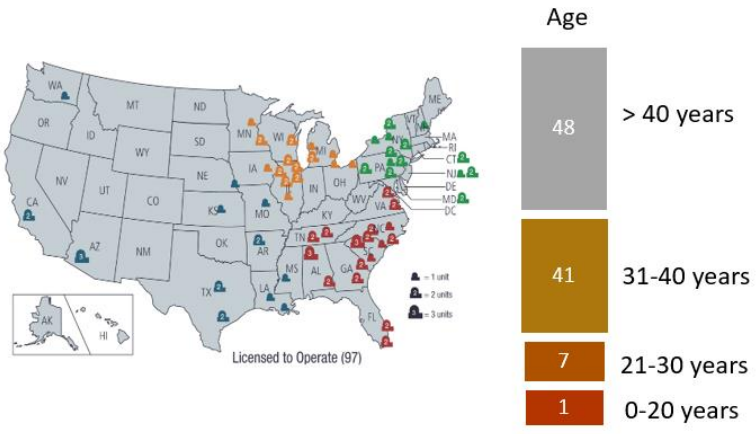

Figure 1-1 Number of operating nuclear power plants and their ages (data from U.S. NRC Datasets, 2019).

The containment structure made of concrete and steel usually 1-1.5 meters (3-5 feet) thick serves as a biological shield between the nuclear reactor and the environment (Figure 1-2). It provides the last layer of safety in case of an accident. There is a need for thorough safety assessments of these containment structures before nuclear power plants can be relicensed. In February 2013, Duke Energy decided to decommission the Crystal River 3 nuclear power plant in Florida due to cracks formed in the containment structure during a maintenance operation. This billion-dollar loss, instigated the need to identify the causes for the failure of the structure and according to an article published by Georgia Institute of Technology, one of the contributing causes for the failure was presumed to be concrete creep (Georgia Institute of Technology, 2015).

The main objective of this research is to understand the aging-related degradation in concrete structures. Creep is a viscoelastic phenomenon that causes concrete to deform for decades under a constant stress. Since the nuclear plants are post-tensioned containment facilities, creep causes post-tensioning losses which reduces the tensile force in the tendons to fall below the original design. Creep depends on several factors such as mix design of concrete, temperature and humidity conditions, curing methods etc.

Creep is generally modeled in terms of a single creep coefficient, however, in nuclear structures, there is a 3D state of stress that complicates the response, despite the isotropy of concrete. Given the geometry and structural detailing in US containment structures, accurate modeling of structural-scale creep and creep-cracking will be aided only by full 3D treatment of both the material and structure.

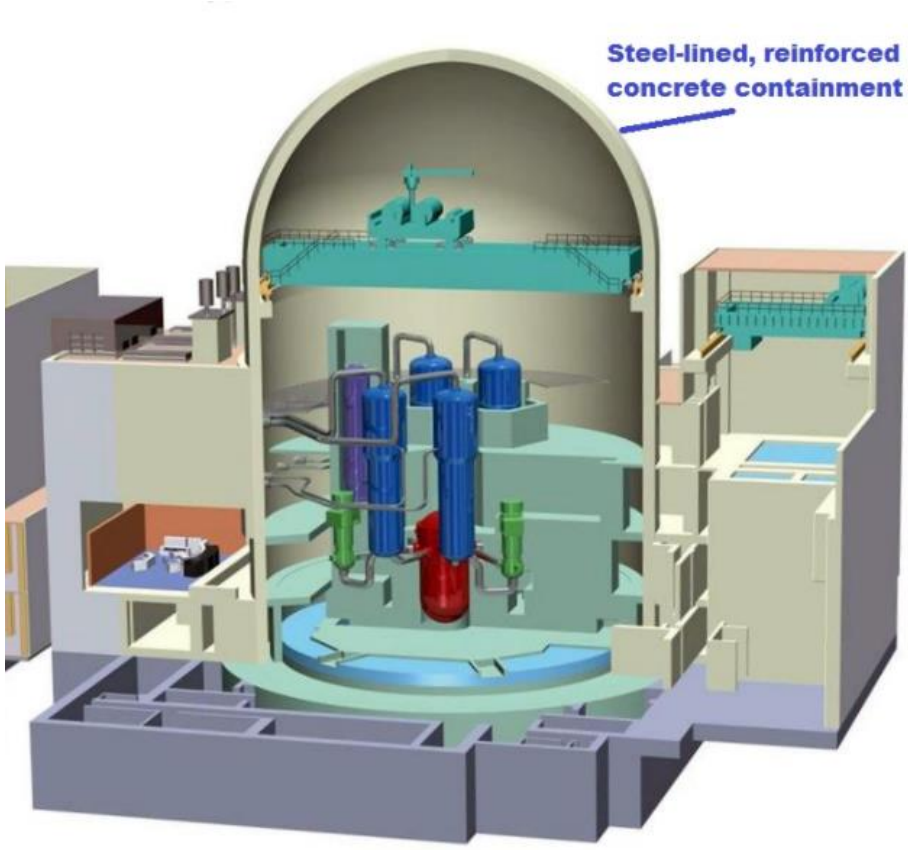

Figure 1-2 Nuclear power plant and its concrete containment structure (adapted from U.S. NRC Datasets, 2019).

1.2. Primary Challenges

To define the scope of research, it is important to identify the challenges in the study of concrete creep and understand how these factors influence creep. These include:

1. Creep proceeds for decades and is difficult to predict from short-term tests
2. Creep is temperature dependent
3. Creep is moisture dependent
4. Concrete ages

5. Concrete is nonlinear
6. Creep is a 3D problem

Concrete creep is known to continue for decades and is speculated to continue indefinitely (Brooks, 2005). A direct, long-term measurement of creep is unattainable given the short time period for the project. Furthermore, concrete creep is temperature dependent. Nuclear concrete undergoes harsh service conditions involving steep temperature and pressure gradients during their lifetime. Hence, determining the dependence of creep on temperature is important for accurately predicting nuclear concrete creep. To address these two challenges, a novel step was taken in the study. Firstly, experiment on concrete creep was substituted by cement mortar creep. It is believed that – since concrete creep occurs almost entirely within the cement paste phase due to the typically linearly elastic behavior of aggregates – the creep experiments can be captured from cement mortar specimens. The focus on cement mortar rather than concrete allows the use of smaller sized test samples compared to traditional concrete creep tests and enables more tests to be run simultaneously with enhanced resolution while minimizing experimental error. Secondly, unique miniature versions of conventional creep frames were built that were much more amenable to placing in climate chambers than larger concrete creep frames. To measure the effect of high temperatures on mortar creep, tests were performed at elevated temperatures (up to 80°C). Concrete creep increases as a function of temperature (Nasser and Neville 1965; McDonald 1975; Ladaoui et al. 2011; Vidal et al. 2015). This introduces the possibility of predicting long-term creep at room temperature by measuring short-term creep at high temperatures using the Time-

Temperature Superposition (TTS) principle. The TTS principle was first noted by Schwarzl (Schwarzl et al. 1952), who recognized that an increase in temperature generally increases the kinetics of most deformation processes in viscoelastic materials. In thermo-rheologically simple materials, this implies that during similar deformation processes at different temperatures, the same sequence of molecular events occurs with different speed and can be correlated using temperature dependent shift factors. The results from the creep tests at different temperatures were shifted to fit along the axis of logarithmic time scale to obtain a creep master curve. The creep measurements from mortar were upscaled to predict concrete creep behavior using a computational algorithm from a concurrent study (Torrence, et al. 2019a and 2019b) .

Concrete creep is moisture dependent and concrete ages with time. Most U.S. nuclear plants have a liner on the interior of their containment facility which minimizes the effect of drying. Experimental measurements of a 30-year-old nuclear wall with liner suggested the internal Relative Humidity (RH) never drops below 80% (Åhs and Poyet, 2015; Oxfall et al., 2013). Throughout the study, creep experiments were carried out on cement mortar/concrete samples that were sealed to prevent drying. Bazant's B3 model and B4 model were also used to assess if drying occurred in the samples based on the free shrinkage strain. It is well understood that concrete ages with time, which alters the properties of the material. The creep rate reduces when stress is applied on aged concrete. However, aging is most critical in the first 28 days after mixing and since post-tensioning for containment walls are not applied at early ages, these effects can be approximated as second order and can be ignored.

Concrete behaves nonlinearly at higher stress levels. But, according to Neville and Dilger non-linearity of cement mortar arises only after the stress/strength is greater than 0.80 (Neville and Dilger, 1970). According to Mindess et al., concrete creep is linearly proportional to stresses up to 50% of its ultimate strength (Mindess et al., 2003). Concrete creep is generally modelled in terms of uniaxial creep compliance. However, nuclear structures are subjected to a 3D state of stress. Significant creep strains may be induced in directions transverse to each principle stress due to Poisson's effect. In this study, 3D creep response of cement mortar was achieved using a novel, confined compression experiment that allows direct determination of the full stress and infinitesimal strain tensors in a single test.

1.3. Research Scope and Tasks

The main goal of this research is to understand the creep behavior of massive containment structures for decades to enable safe and long-term operation of these facilities. For this purpose, creep tests were performed on cement mortar samples at different temperatures in miniaturized creep frames. A constitutive model was developed for the uniaxial creep compliance. Simultaneously, confined creep test was also performed on cement mortar samples to analyze and model the 3D creep response. The 3D constitutive properties of cement mortar were upscaled to predict concrete creep behavior using advanced computational composite models that account for the presence of aggregates, their geometry, and distribution as obtained through innovative experimental tomography of real concrete aggregates. This is elaborated in a companion dissertation (Torrence et al. 2019a and 2019b) and is outside the scope of this work. Creep tests were also conducted

in the laboratory on concrete samples at room temperature and elevated temperatures up to 60 °C to validate the concrete creep model upscaled from the mortar data. The concrete creep model developed from computational approach was used as an input in Grizzly code, a simulation tool for aging processes and the behavior of aged nuclear power plant components, as part of the follow-up work done at the Idaho National Laboratory (INL). Also part of the broader project scope but not part of this dissertation, three concrete wall sections with varying thicknesses, reinforcement ratios and post-tensioning loads were constructed for validating the structural code. The scope of work presented in this dissertation in conjunction with other connected research activities provide improved analysis and prediction of remaining life of existing concrete containment structures, post-tensioning losses, effects of creep on structural capacity, and the likely impact of repair activities on stress fields and crack potential.

The tasks involved to complete the scope of this dissertation are summarized below and depicted in Figure 1-3:

1. Design of ten miniaturized creep loading frames for cement mortar samples.
2. Instrumentation and data collection of uniaxial creep test on cement mortar.
3. Estimation of drying creep and basic creep components from the total compliance function using B3 and B4 models if applicable.
4. Development of a constitutive model to predict several decades of creep compliance of cement mortar through short term tests using TTS principle.
5. Design of a novel confined creep test to capture the 3D constitutive properties of cement mortar.

6. Development of bulk and shear compliance functions as well as viscoelastic Poisson's ratio of cement mortar from the confined creep test.
7. Conducting creep test on concrete specimens to validate the upscaling scheme of cement mortar to concrete properties using advanced computational models.

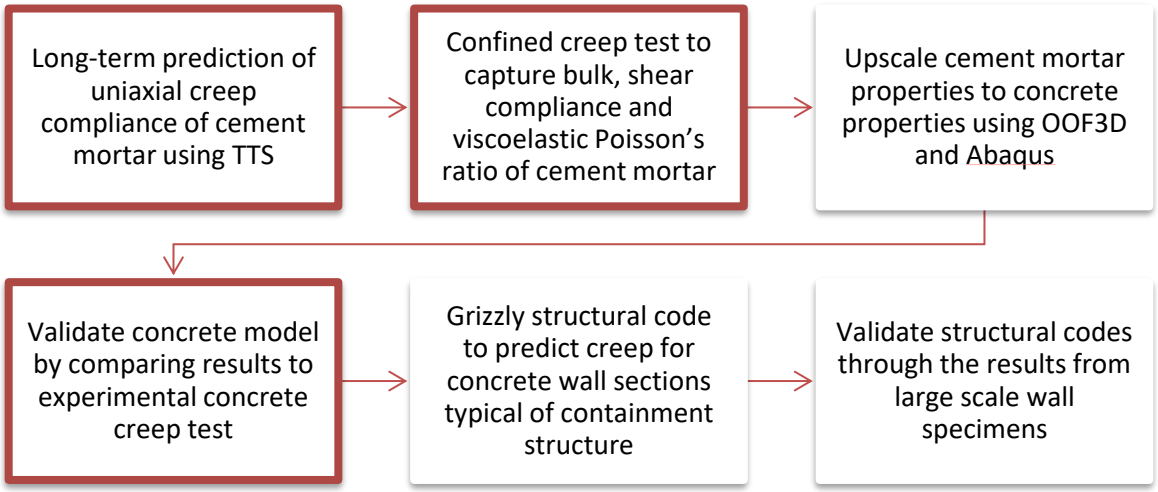

Figure 1-3 Flowchart of the overall project scope. The highlighted sections depict the scope of this dissertation.

1.4. Dissertation Outline

The dissertation is divided into five sections.

Chapter 1 presents the background information and the necessity for the proposed research by outlining the problem statement. Primary challenges in the study are identified and the approach taken to mitigate the problems is discussed. Finally, the overall project scope and objectives of this dissertation are summarized.

Chapter 2 presents a comprehensive literature review on uniaxial creep tests on cementitious materials. The experimental method followed to conduct uniaxial creep test on cement mortar specimens in a miniaturized creep frame at different temperatures is described. The utilization of TTS principle to obtain a basic creep compliance master curve is outlined. A brief review of the B3 model and B4 model to assess the drying creep compliance is presented.

Chapter 3 describes the confined creep test performed at different temperatures to quantify the 3D creep response of cement mortar. The results obtained on the 3D constitutive properties of cement mortar such as bulk compliance, shear compliance and viscoelastic Poisson's ration are presented and discussed.

Chapter 4 outlines the concrete creep experiments and shows the comparison of experimental results to simulated results.

Chapter 5 presents a summary of the work done, the key conclusions and contributions from the research and provides recommendations for future work.

References

1. Åhs, M. and Poyet, S.: The prediction of moisture and temperature distribution in a concrete reactor containment. Tech. report. Lund University (2015).
2. Brooks, J.J. (2005). "30-year creep and shrinkage of concrete," Magazine of Concrete Research, 57, No. 9: p. 545-556.
3. Georgia Institute of Technology. PhD student Bradley Dolphyn studying the concrete cracks that shut down Crystal River nuclear power plant. *https://ce.gatech.edu/category/crystal-river-3* (2015).

4. Ladaoui, W., Vidal, T., Sellier, A. and Bourbon, X.: Effect of a temperature change from 20 to 50ºC on the basic creep of HPC and HPFRC. Mater. Struct. **44** (9), 1629-1639 (2011).
5. Mc Donald, J. E.: Time dependent deformation of concrete under multiaxial stress conditions. In: Technical Report C-75-4 Concrete Laboratory, US Army Engineering Waterways Experiment Station, Vicksburg, MS (1975).
6. Mindess, S, Young, F. J. and Darwin, D. Concrete. 2nd. ed. Pearson Education, Inc. (2003).
7. Nasser, K. W. and Neville, A. M.: Creep of Concrete at Elevated Temperature. ACI J. Proc. **62** (12), 1567-1579 (1965).
8. Neville, A. M. and Dilger, W.: Creep of Concrete: Plain, Reinforced, Prestressed. North-Holland, Amsterdam (1970).
9. Oxfall, M., Johansson, P. and Hassanzadeh, M.: Moisture profiles in concrete walls of a nuclear reactor containment after 30 years of operation. Lund university (2013).
10. Schwarzl, F. and Staverman, A. J.: Time-Temperature Dependence of Linear Viscoelastic Behavior. J. Appl. Phys. **23** (1952).
11. Torrence, C., Baranikumar, A. and Grasley, Z.: Nuclear concrete microstructure generation and analysis of long-term performance. 19th International Conference on Environmental Degradation of Materials in Nuclear Power Systems – Water Reactors, Boston, August 18-22, American Nuclear Society. (2019a).

12. Torrence, C.E., Baranikumar, A. and Grasley, Z.: Homogenization of concrete in nuclear power plants. 25th International Conference on Structural Mechanics in Reactor Technology, Charlotte, August (2019b).
13. U.S. Energy Information Administration – EIA – U.S Nuclear industry (2018). *https://www.eia.gov/energyexplained/nuclear/us-nuclear-industry.php*
14. U.S. Nuclear Regulatory Commission – NRC Datasets (2019) *https://www.nrc.gov/reading-rm/doc-collections/datasets/*
15. Vidal, T., Sellier, A., Ladaoui, W., and Bourbon, X.: Effect of temperature on basic creep of High-Performance Concretes heated between 20ºC and 80ºC. J. Mater. Civil Eng. **27** (7) (2015).

2. UNIAXIAL CREEP RESPONSE OF CEMENT MORTAR

In this chapter, after a brief introduction on creep, a detailed literature review on creep of cementitious materials at varying temperatures is discussed. The focus of this chapter is to detail the utilization of Time Temperature Superposition Principle to predict several decades of creep compliance from short term experiments at elevated temperatures.

2.1. Background

A viscoelastic material such as concrete has the characteristics of an elastic spring as well as viscous dashpot. When such a material is subjected to constant stress, there is an instantaneous elastic response followed by time-dependent creep strain. When the material is unloaded from stress, there is an instantaneous elastic recovery followed by creep recovery. In most cases, there is a considerable portion of total creep that is irreversible (Figure 2-1).

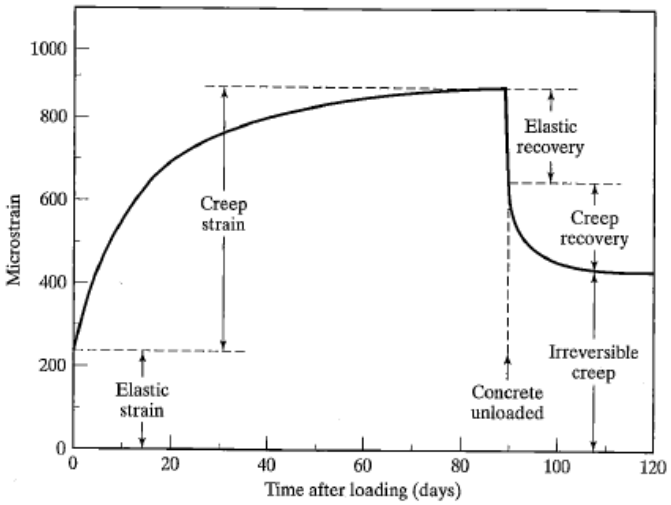

Figure 2-1 Typical creep behavior of plain concrete (adapted from Mindess, Young and Darwin book, 2003).

Creep can be subdivided into basic creep and drying creep. Basic creep is the creep occurring under conditions of no change in moisture content of the loaded specimen. Drying creep is the creep, in addition to basic creep, resulting under conditions of a change in moisture content of the loaded specimen. Drying creep is also referred to as the Pickett effect (Pickett, 1942). Figure 2-2 illustrates this concept where the sum of strains due to drying shrinkage and basic creep is always less than the strain due to creep in a sample undergoing simultaneous loading and drying (Bažant, 1993).

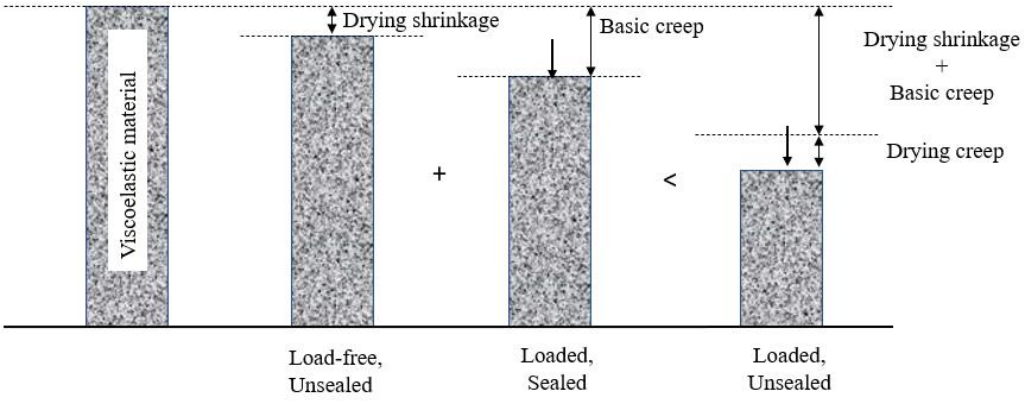

Figure 2-2 Representation of Pickett effect (adapted from Bažant, 1993).

Different combinations of a spring and dashpot elements may be used to represent stress and corresponding strain component for a viscoelastic material. Mechanical models are equivalent to writing down a differential equation which relates stress and strain with respect to time. However, mechanical model has an advantage over the equation, as the behavior of the viscoelastic material can be inferred from a glance at the model. The two most common mechanical models used to represent the compliance function are the

Maxwell model and Kelvin-Voigt model. The important criteria in selecting a model is that, the model chosen should satisfactorily represent the behavior of the material. For example, a Maxwell chain which consists of parallel arrangement of number of Maxwell components (spring and dashpot in series) do not accurately predict creep as the strain function in that model increases linearly with time under constant stress (Figure 2-3 (a) and (b)). But in most polymers, the strain rate decreases with time. The creep compliance for a Maxwell chain can be expressed as:

$$J(t) = \sum_{i=1}^{n} \frac{1}{E_i} \left(1 + \frac{E_i}{\mu_i} t \right) \tag{1}$$

where E_i refers to the spring constant and μ_i refers to the viscosity of the dashpots. The term μ_i / E_i can be denoted as τ_m called the relaxation time. The relaxation time is the time the material takes for the relaxation modulus to drop to 1/e or 0.368 times the initial value. On the other hand, a Kelvin-Voigt chain which is a series arrangement of number of Kelvin-Voigt components (spring and dashpot in parallel) is suitable for predicting creep response of viscoelastic material (Figure 2-3 (c) and (d)). The compliance of a Kelvin chain can be expressed as:

$$J(t) = \sum_{i=1}^{n} \frac{1}{E_i} \left(1 - e^{-\frac{E_i}{\mu_i} t} \right) \tag{2}$$

where the term μ_i / E_i can be denoted as τ_i called the retardation time. The retardation time is the time the material takes for the creep compliance to reach 0.632 times the final value. Since Kelvin-Voigt model cannot represent instantaneous elastic

response, in most cases a spring is added in series to the Kelvin chain to accurately represent the behavior of the material.

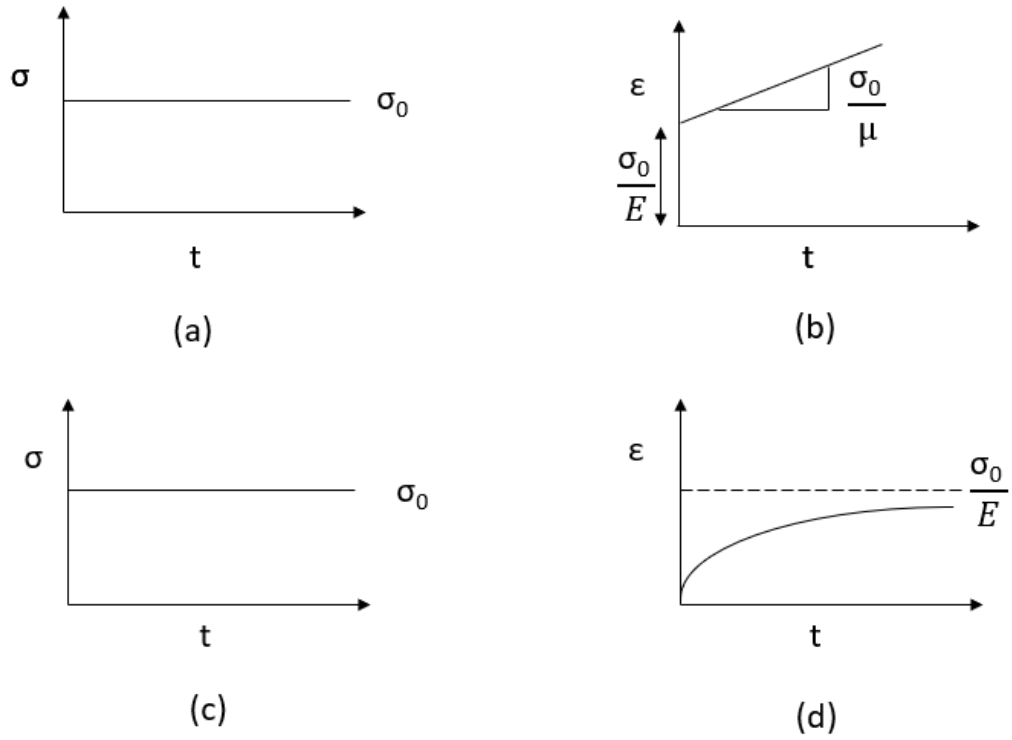

Figure 2-3 (a), (b) Representation of Maxwell model under constant stress and its corresponding strain output, (c), (d) Representation of Kelvin-Voigt model under constant stress and its corresponding strain output.

As creep continues indefinitely and the compliance function in Kelvin model asymptotes at later ages, an even better way to describe the compliance is using the logarithmic function which is writing the exponential function in eqn.(1) in logarithmic form such as:

$$J(t) = \sum_{i=1n}^{n} \frac{1}{E_i} Log\left(1 + \frac{E_i}{\mu_i} t\right) \tag{3}$$

2.2. Literature Review

Creep is a phenomenon that causes viscoelastic materials such as concrete to deform as a logarithmic function of time under constant stress (Aili 2017). Several studies have been conducted over the past few decades to predict concrete creep (Tulin 1965; Jordaan 1974; Bažant 1988; Brooks 2005). In post-tensioned structures such as nuclear containment facilities and hydraulic dams, creep can cause redistribution of stresses, large deformations and prestress losses that ultimately compromise the safety of the structure. As creep occurs indefinitely (Brooks 2005), laboratory measurements of long-term creep are both challenging and time consuming; this serves as motivation for researchers to develop more effective methods to characterize or predict long-term creep of concrete. There are numerous studies in the literature that discuss the effects of temperature on creep of concrete. Nasser and Neville found that creep of concrete at room temperature (21ºC) can be 3 to 4 times the initial deformation within the first 1 to 2 years and that at elevated temperatures, such as 96ºC, creep effects are further amplified. Nasser and Neville found that for samples with a stress-strength ratio of 35% loaded at 14 days of age and 15 months under load, the creep at 72ºC was 1.75 times greater than that at 21ºC and the creep at 96ºC was 1.95 times higher than that at 21ºC (Nasser and Neville 1965). In comparison, McDonald showed that for samples at a stress-strength ratio of 31% loaded at 90 days of age and 12 months under load, the compressive creep of concrete at 66ºC was 1.79 times that observed at 23ºC (McDonald 1975). Bažant summarized the temperature effect on concrete creep from the literature and used the microprestress-solidification theory to fit the data considering the influence of temperature (Bažant et al. 2004). More recently,

researchers (Ladaoui et al. 2011; Vidal et al. 2015) have analyzed the effect of temperature ranging between 20ºC and 80ºC on the basic creep of High-Performance Concrete (HPC). The companion studies concluded that the basic creep of HPC doubled at a stress-strength ratio of 30% and 10 months under load when the temperature was increased from 20ºC to 50ºC.

It is hence well-established that concrete creep increases as a function of temperature. This introduces the possibility of predicting long-term creep at room temperature by measuring short-term creep at high temperatures using the Time-Temperature Superposition (TTS) principle. The TTS principle was first noted by Schwarzl (Schwarzl et al. 1952), who recognized that an increase in temperature generally increases the kinetics of most deformation processes in viscoelastic materials. TTS is effectively used to model the temperature-dependent mechanical properties of thermorheologically simple polymers wherein temperature changes significantly impact creep. Thermorheologically simple materials are those materials whose temperature dependence for viscoelastic processes is fully captured by the temperature dependence of relaxation/retardation times (Drozdov 1998; Christensen 2003; Hernández 2017). For such materials, by experimentally measuring creep strain at different temperatures, a creep master curve can be generated by shifting the data along a logarithmic time axis. To best of the author's knowledge, none of the studies in open literature have explicitly utilized the TTS principle to predict long-term concrete creep.

In the current study, the use of the TTS principle to model the temperature dependence of basic creep in mature cement mortars (where aging effects are less

significant) are assessed, and thus to predict long-term creep from short-term experiments conducted at elevated temperatures. It is believed that – since concrete creep occurs almost entirely within the cement paste phase due to the typically linearly elastic behavior of aggregates – the assessment of the viability of TTS to mortar creep will be applicable to concrete. First, the applicability of TTS to mature, cement-based materials exhibiting basic creep is evaluated using existing data and models from the literature. Next, an experimental study is performed on cement mortar samples to demonstrate the utility of TTS to predict long-term mortar creep from short term tests conducted at multiple elevated temperatures. The focus on cement mortar rather than concrete allows the use of smaller sized test samples compared to traditional concrete creep tests and enables more tests to be run simultaneously with enhanced resolution while minimizing experimental error. A smaller creep frame can be designed and used to fit in climatic chambers and tests can more readily be run at different temperatures. The testing modifications reduced the overall cost and time involved in conducting the experiments while enhancing the resolution of creep measurements.

2.3. Initial Assessment of the TTS Principle to Predict Creep

As an initial step to verify the applicability of developing a creep master curve for cement mortar using TTS, basic creep data obtained from a recent study (Vidal et.al 2015) was fitted using the TTS principle to predict long-term creep. The basic axial creep data used was obtained on HPC using Type I cement with stress/strength ratio of 35% loaded at 300 days of age and 10 months under load at 20ºC, 50ºC and 80ºC. The creep compliance was computed from the basic creep strain and applied stress. The data obtained for creep

compliance at high temperatures was then shifted to a reference room temperature (20ºC) using a temperature shift factor to obtain a creep compliance master curve (Figure 2-4). The resulting smooth curve with overlapping data from differing temperatures illustrated that TTS was successfully applied to predict creep compliance for nearly 30 years using basic creep data obtained during the initial 300 days.

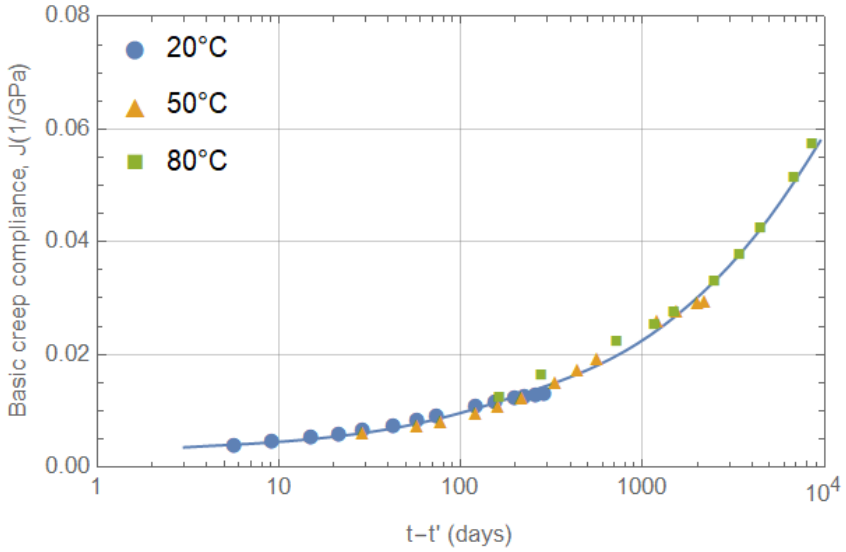

Figure 2-4 Basic creep compliance, J (t,t') master curve at 20ºC developed using TTS principle applied to data from Vidal et al. 2015.

In addition, the B4 model (Bažant et al. 2014) was used to generate basic creep compliance curves for mature concrete (loaded at 56 days of age) at three different temperatures (20ºC, 50ºC and 80ºC); the results are plotted in Figure 2-5. It is clear from the figures that the B4 model – which is based on fitting a large database of concrete creep test results – predicts a temperature dependence of basic creep that indicates a thermorheologically simple behavior of the mature concrete. This should not be surprising given that the B4 model quantifies the temperature effects on concrete creep as a multiplier

(determined by an Arrhenius function of temperature) on creep time (to create a reduced time) – this is essentially equivalent to using a multiplier on relaxation/retardation times.

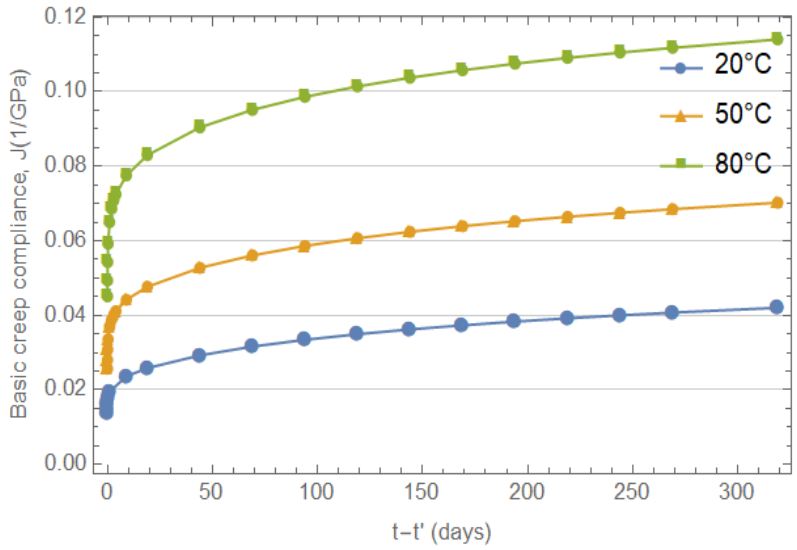

(a)

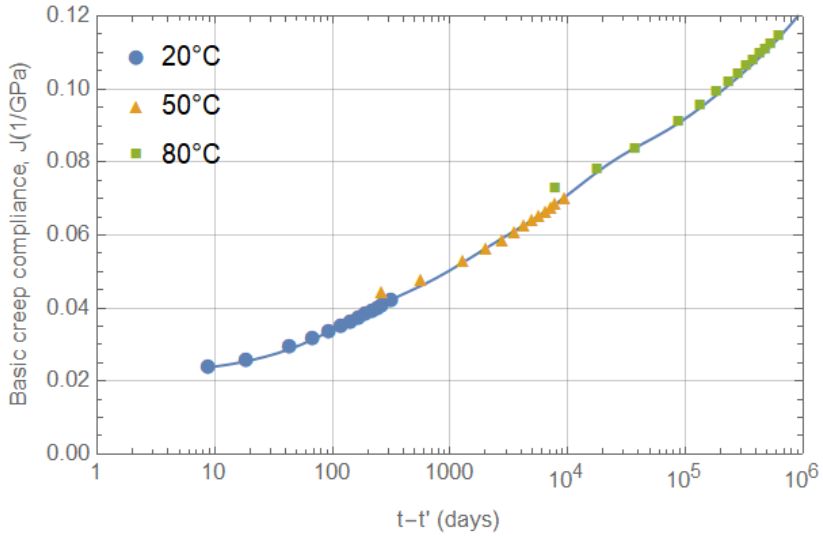

(b)

Figure 2-5 a) Basic creep compliance of concrete using B4 model at different temperatures. (b) Basic creep compliance master curve at 20ºC on log time scale using TTS principle.

These initial analyses of a recent dataset of concrete creep at multiple temperatures and the B4 model of concrete creep both indicate that mature concrete, exhibiting only basic creep, may be well approximated as behaving in a thermorheologically simple fashion. However, it should be noted that at early ages concrete likely does not behave in a thermorheologically simple fashion given the strong influence of hydration and other aging mechanisms (Grasley 2006 and Grasley and Leung 2011). Furthermore, at temperatures below the freezing and above the boiling points of water the TTS principle will not be applicable given that the temperature effects generate phase changes and initiate new mechanisms of time-dependent deformation (Rahman et al. 2016) rather than simply influence the kinetics of mechanisms active in the intermediate temperature range.

2.4. Experimental Design

Given the positive indications of the applicability of TTS to cementitious materials from the assessment of experimental data from the literature along with the B4 model, an in-depth experimental program was carried out on the temperature-dependent creep of cement mortars.

2.4.1. Cement Mortar Mix Design

The cement mortar mix design was selected to closely resemble the Vérification Réaliste du Confinement des Réacteurs (VeRCoRs) mortar mix used by Électricité de France (EDF). The mortar samples were prepared using Type I/II cement and river sand. The river sand used was sieved to pass the 2.38 mm sieve and dried for 24 hours before mixing. The water to cement ratio by mass (w/c) for the mix was kept at 0.52 (SSD condition) and the sand to cement ratio by mass was 2.12. About 422.5 mL of water reducing admixture

‘Pozzolith 80’ was added per 100kg of cement. The mixture proportions are shown in Table 2-1 and referenced in (EDF 2014).

Table 2-1 Mixture proportions in SSD condition.

Materials	Unit	Mix Quantity
Cement (Type I/II)	kg/m^3	601
	lb/yd^3	1013
River Sand	kg/m^3	1263
	lb/yd^3	2129
Water	kg/m^3	323
	lb/yd^3	544.4
Pozzolith 80	l/m^3	2.54
	oz/yd^3	66

2.4.2. Sample Preparation

2.4.2.1. Creep Samples

Cement mortar was mixed in accordance with ASTM C305-99 and immediately cast into 50 mm x 100 mm (2 in. x 4 in.) cylindrical molds with embedded vibrating wire gages (50 mm or 2 in. gage length) from Geokon. The theory of operation of vibrating wire gage is detailed in Appendix B - Data acquisition. Fishing line was used to suspend the gage axially at the center of each mold (see Figure 2-6 (a)). The cylinders were filled in three equal increments and tapped after each increment to minimize air voids. Once filled, the cement mortar samples were retained in the mold to prevent moisture loss until just prior

to the time of testing after 28 days. The demolded samples were immediately sealed with one layer of adhesive-backed aluminum foil to minimize drying. Sulfur capping compound was used to ensure the ends of the sample were smooth and concrete plugs were attached to both ends of the sample to ensure uniform compressive stress throughout the cross-section per the St. Venant's principle. Figure 2-6 (b) shows the set up of samples ready for the creep experiment.

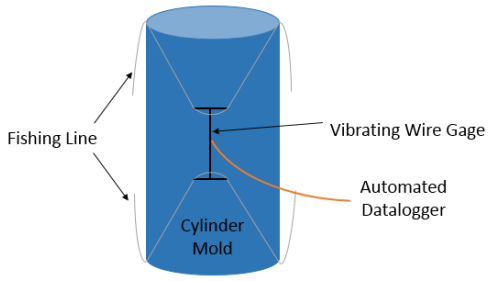

(a)

(b)

Figure 2-6 (a) Graphical representation of suspending vibrating wire gage at the center of the mold using fishing line (b) Cement mortar samples sealed up and sulfur capped.

2.4.2.2. Free Strain Samples

In addition to the uniaxial creep test, companion cylindrical specimens having dimensions of 50 mm x 100 mm (2 in. x 4 in.) were fabricated to record the free strain due to shrinkage at each temperature for the entire duration of the creep test. The age and test conditions of these load-free specimens were the same as those used in the creep tests. An embedded vibrating wire gage was used to record the free strain with time.

2.4.3. Fabrication of Creep Frame

A unique, miniature version of the standard ASTM C512 concrete creep frame was designed and fabricated exclusively for the cement mortar samples as shown in Figure 2-7. The total height of the scaled down frame is 45 cm (18 in.) as supposed to the approximately 180 cm (6 ft.) tall standard concrete creep frame. The diameter of the frame is 10 cm (4 in.). The creep frame has a compression spring at the bottom of the frame which helps to maintain a constant load. Above the spring is a plate with a ball bearing at the center to ensure minimum eccentricity in loading. An inline load cell is placed just below the sample to record the load levels in the frame. Although stress levels are intended to be constant during a creep test, the actual stress level was recorded periodically to account for any load loss. A 5 ton mini hydraulic jack was used to apply the initial axial force. Threaded rods and nuts are provided in the frame to maintain a constant load after removal of the jack. Most importantly, the newly designed creep frame is amenable to placing in climate chambers and temperature ovens required to perform thermally accelerated creep tests.

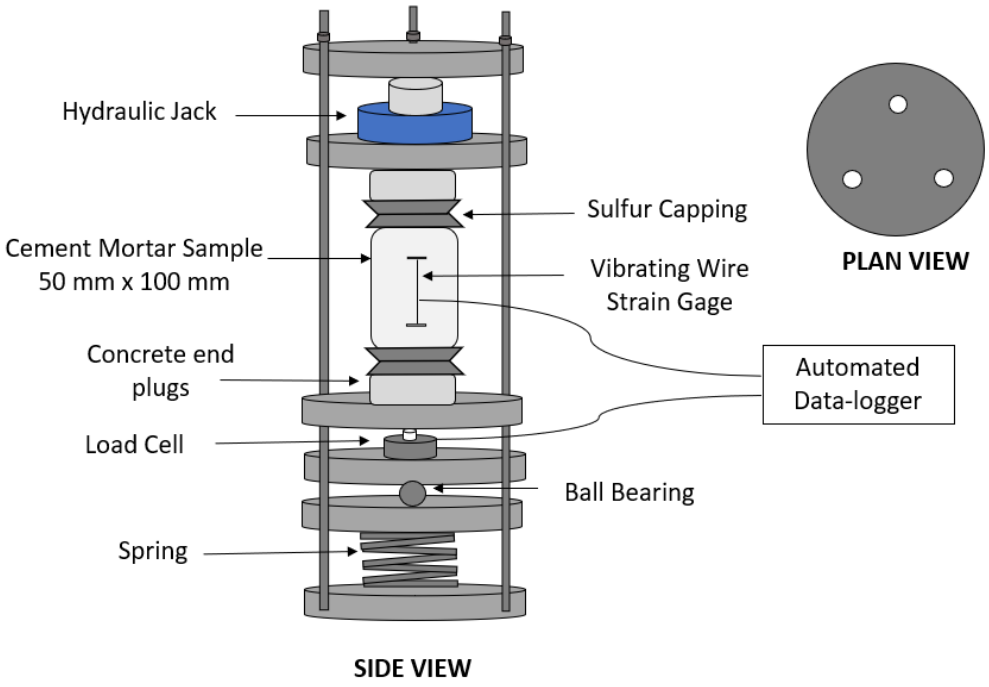

Figure 2-7 Miniaturized cement mortar creep test frame. This frame is 45 cm (18 in.) in total height and is a scaled down version of ASTM standard concrete creep frame, which is approximately 180 cm (6 ft.) in height.

2.4.4. Uniaxial Creep Test setup

The previously described miniaturized creep frame was used to run the uniaxial creep test. The cement mortar samples were loaded at 28 days of age using a hydraulic jack to a constant load of 775 kg (1700 lbs.) which corresponded to 10% of 28-day compressive strength of the mortar. At this loading age and stress magnitude, the mature cement mortar is approximated as a non-aging, linearly viscoelastic material.

The load was approximated as a stepwise load function given the very short time span of load application relative to the overall duration of the creep test. The axial strain from the vibrating wire gage as well as the load readings from the load cell were recorded

every 30 minutes using a CR300 Data logger, AM16/32B Multiplexer and a 2-Channel Vibrating-Wire Analyzer (AVW200) purchased from Campbell Scientific. As alluded to earlier, creep tests were run at three different temperatures: 20°C (reference temperature), 60°C and 80°C. Three replicates of cement mortar samples were used at each temperature and were heated to the respective test temperature before starting the creep test (to avoid the accumulation of thermal strains during creep). The experiments were conducted in environmental chambers maintaining a constant temperature (Figure 2-8). The relative humidity was consistent at 50% in the 20°C chamber and below 10% in the 60°C and 80°C chambers.

Figure 2-8 Uniaxial creep test setup using the miniaturized creep frame inside an environmental chamber maintaining constant temperature and humidity.

2.5. Results and Discussion

2.5.1. Cement Mortar Mix Properties

The compressive strength ($f_c^{'}$) and elastic Young's modulus (E) of the cement mortar were measured at ages of 3, 7, 14, 28 and 90 days in accordance with the test procedures outlined in ASTM C39 and ASTM C469 respectively. The mortar was mixed according to ASTM C305-99 and immediately cast into 100 mm x 200 mm (4 in. x 8 in.) cylindrical molds. The cylinders were filled in three equal increments and tapped after each increment to minimize air voids. All samples were kept in the mold until the testing time. Axial deformation was measured using an extensometer with a 100 mm (4 in.) gage length.

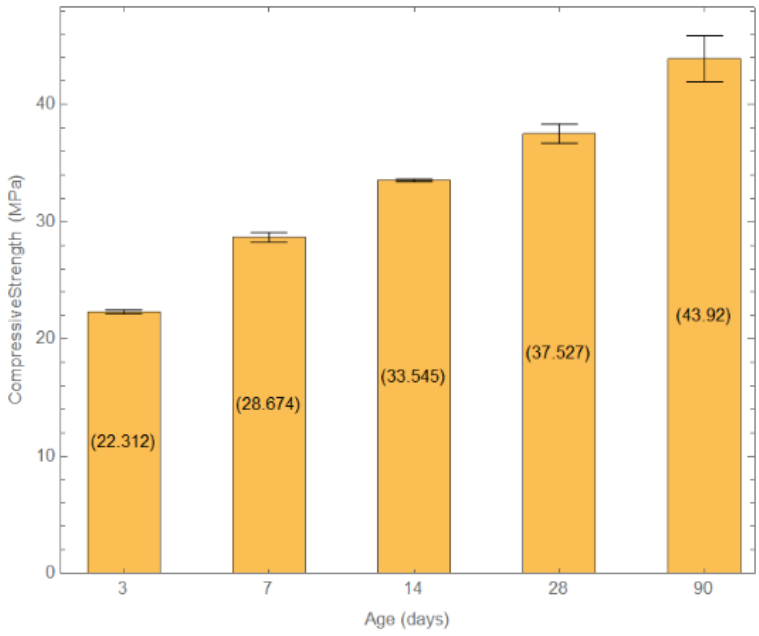

Figure 2-9 Average compressive strength of mortar at different ages along with the standard error for each measurement.

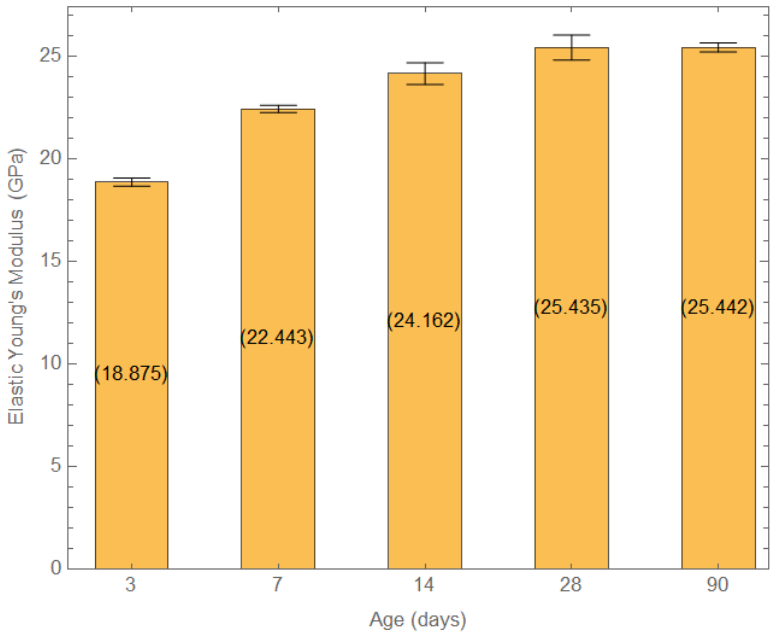

Figure 2-10 Average elastic Young's modulus of mortar at different ages along with the standard error for each measurement.

Three replicates of the mortar samples were tested at each age. The evolution of mean values of $f_c^{'}$ and E of cement mortar with age is shown in Figure 2-9 and Figure 2-10 along with the standard error for each measurement. As expected, the strength increases with age whereas the elastic modulus increases for the first 28 days and then stays constant after that. It is known that the degree of hydration plays a role in influencing the elastic properties (Boumiz. Et al., 1996). Since the hydration reaction ceases after 28 days, there is no increase in the elastic stiffness of the cement mortar at 90 days.

2.5.2. Free Strain

The free strain (or free shrinkage) data obtained at the different test temperatures on the companion specimens is shown in Figure 2-11. Although the samples were sealed using aluminum foil, the authors propose that the free shrinkage recorded is a combination of

autogenous and drying shrinkage (the foil does not provide a perfect seal). The relative magnitudes of autogenous and drying shrinkage decomposed using the B4 model is shown in the later section. The free strain at 60ºC was higher compared to that at 20ºC, which may be explained by higher drying at the higher temperature (measured mass loss data confirmed this trend). However, the free strain measured at 80ºC was less than measured at 60ºC; measured mass loss data followed a similar trend. Thus, additional drying occurred at 60ºC versus at 80ºC despite similar humidity in each chamber. While the authors cannot be certain of the explanation for these trends, it may be that one chamber has increased convection versus the other. Regardless of the proper explanation, subsequent discussion in this paper will show that the effect of drying on creep is small at all three temperatures.

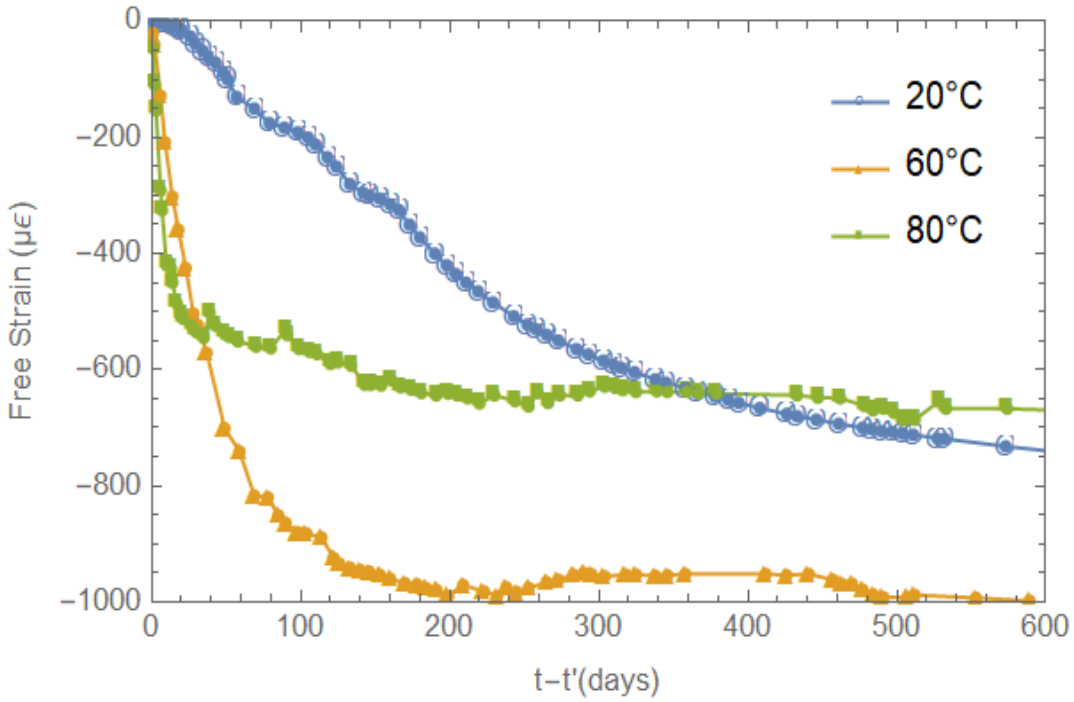

Figure 2-11 Free strain (autogenous+drying shrinkage) data with time at different temperatures. Here t refers to the present age and t' refers to the age when creep test began.

2.5.3. Uniaxial Creep test

The stress applied was calculated as a function of time using the load recorded from the load cell and the cross-sectional area of the samples. If load loss was observed, it was accounted for while modeling creep compliance, as described later in this section. Significant load loss was observed in the cement mortar samples at the higher temperatures (60°C and 80°C) due to appreciable creep deformation. The samples at 80°C were reloaded if the load dropped to below 50% of the initial load applied. Figure 2-12 (a) shows a representative fitted stress function of a mortar sample at 20°C. At this temperature, load was fairly constant at room temperature with at most 10% load loss over

the 600 days test period. If a second load application was required, as was the case with few samples at 80°C, sigmoidal function was used to fit the entire stress history and the creep compliance was modelled using the Boltzmann's superposition principle for the two applications of load.

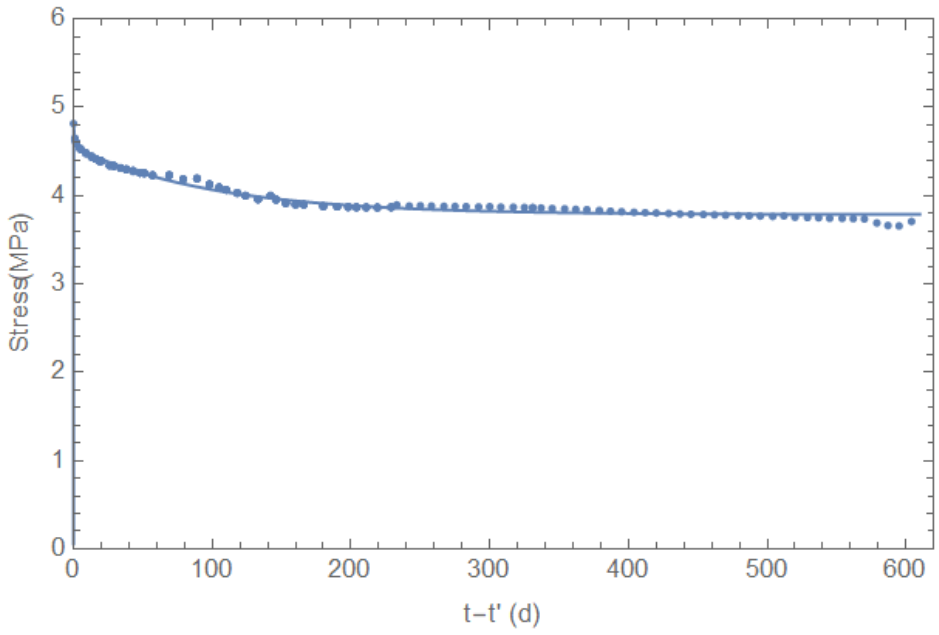

(a)

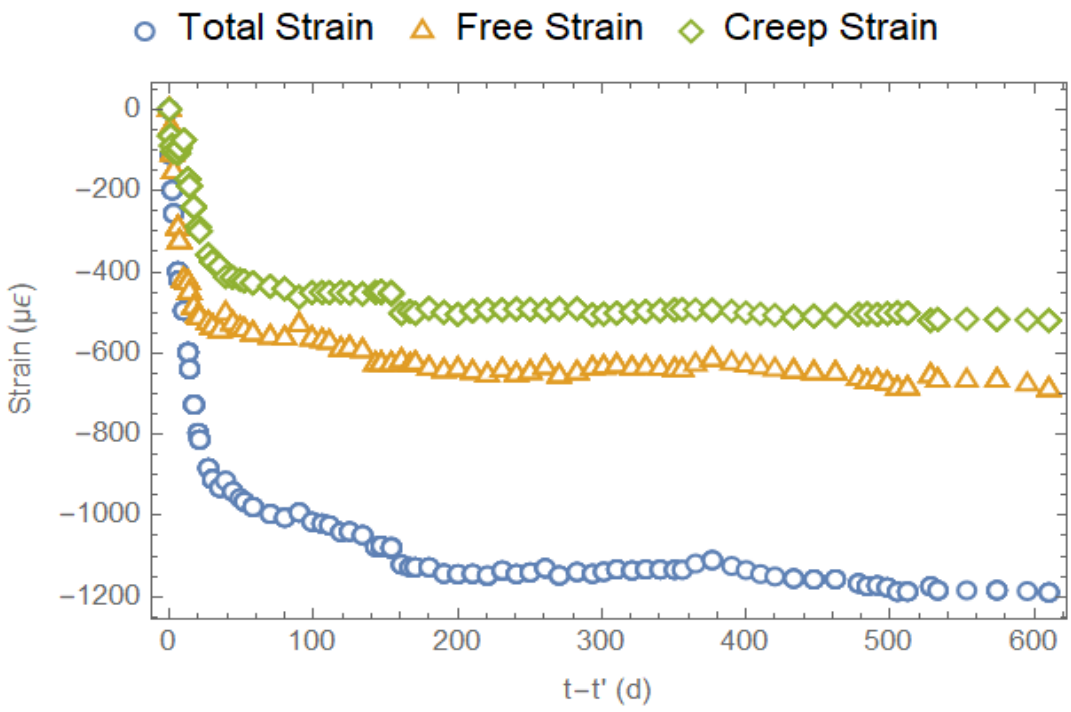

(b)

Figure 2-12 (a) Fitted stress with respect to time under load for a sample at 20°C. Note that the stress is reasonably constant with at most 10% load loss. (b) Graph showing total strain, free strain and creep strain for a sample under load as a function of time.

Figure 2-12 (b) shows the different components of strain in the mortar sample from a creep test. The strain readings represent the average strains recorded for the three replicate specimens. The vibrating wire gage at the center of the sample records the total strain. The free strain reading was constantly monitored in an unloaded specimen at the same age and test conditions. Despite the fact that all samples were sealed with an aluminium foil to restrict drying, the authors believe that the free strain measured was mostly from drying shrinkage since autogenous shrinkage is unlikely in a mix design with 0.52 w/c ratio. If drying did occur in the samples during the test as anticipated, the

measured creep strain is the sum of basic creep and drying creep in accordance to the Pickett effect. This issue will be addressed later in the paper. The creep strain in Figure 2-12 (b), which is the primary point of interest in this study, is the difference between the total strain and free strain.

It was observed that after 600 days, the creep strain at 60ºC was 1.51 times higher than that at 20ºC and the creep strain at 80ºC was 2.40 times higher than that at 20ºC. These multipliers are similar to those recorded in existing literature (Nasser and Neville 1965; McDonald 1975). Using the B4 model, creep at 60ºC and 80ºC was 1.32 times and 1.88 times higher respectively than the corresponding value at 20ºC. The average creep strains obtained at the different test temperatures are plotted in Figure 2-13.

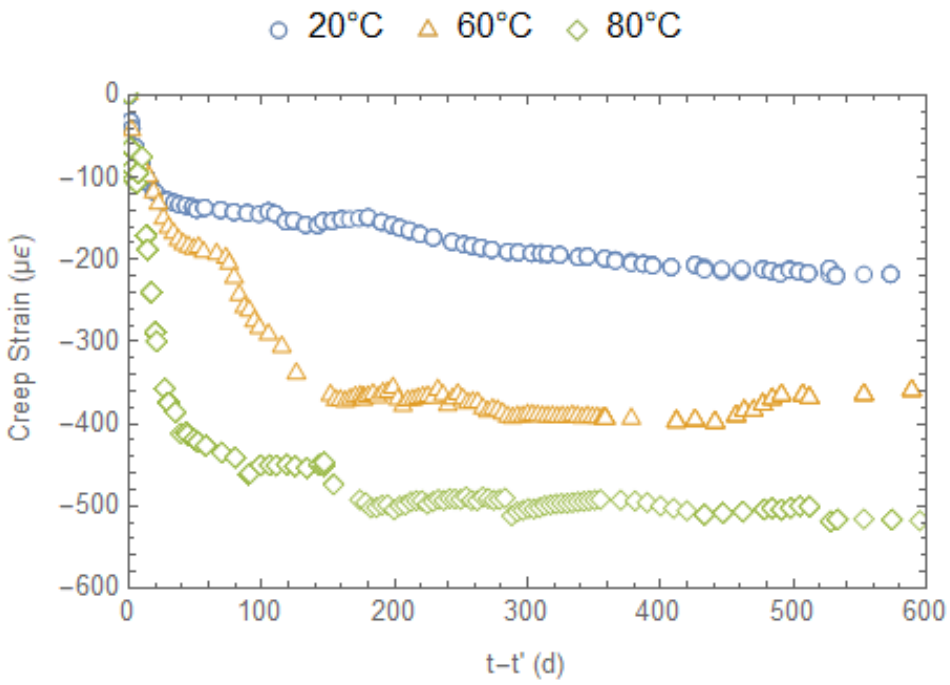

Figure 2-13 Average creep strain data at different temperatures. The creep strain at 60ºC is 1.51 times higher and the creep strain at 80ºC is 2.40 times higher than that at 20ºC after 600 days of testing.

2.5.3.1. Analysis of methods for determining $J(t)$ from creep results

Since there is significant load loss encountered in creep tests conducted at elevated temperatures, a more informative way to compare the creep test results at varying temperatures (rather than plotting creep strain) is to assess the creep compliance, $J(t)$. The creep compliance at a constant load is given by dividing the measured creep strain by the applied stress, but the stress-strain relationship is of the integral or differential type for a non-constant stress history. For a non-aging, linearly viscoelastic material, the axial strain ($\varepsilon(t)$) is related to the axial stress $\sigma(t)$ according to

$$\varepsilon(t) = \int_0^t J(t-t') \frac{\partial \sigma(t')}{\partial t'} dt' , \qquad (4)$$

where t is the present time and t' is the dummy time variable. In order to determine $J(t)$ using the constitutive expression given in eq. (4) it is necessary to fit the measured stress history to a time dependent function, take the derivative of that function (in terms of the dummy time variable), multiply the derivative by a presumed function for $J(t)$ - including phenomenological fit coefficients – and then integrate the product over time. The resulting time dependent function is fit to measured strain data to determine the phenomenological fit coefficients included in $J(t)$. The fitted spring constants and retardation times used in the Kelvin chain is shown in Table 2-2.

Table 2-2 Spring constants and retardation times used in the Kelvin chain at different temperatures.

(a) 20ºC

Specimen 1		Specimen 2	
τ_i	J_i(1/GPa)	τ_i	J_i(1/GPa)
1	0.0058	1	0.0051
10	$3.198*10^{-9}$	10	$5.036*10^{-10}$
100	$2.832*10^{-9}$	100	$4.513*10^{-9}$
1000	0.1196	1000	0.1525

(b) 60ºC

Specimen 1		Specimen 2	
τ_i	J_i(1/GPa)	τ_i	J_i(1/GPa)
1	$6.623*10^{-10}$	1	$1.412*10^{-9}$
10	0.0175	10	0.0342
100	0.0211	100	$2.932*10^{-9}$
1000	$3.938*10^{-10}$	1000	$2.826*10^{-9}$

(c) 80ºC

Specimen 1		Specimen 2	
τ_i	J_i(1/GPa)	τ_i	J_i(1/GPa)
1	0.0111	1	$1.416*10^{-9}$
10	0.0558	10	0.0398
100	$3.857*10^{-9}$	100	$1.873*10^{-9}$
1000	0.0344	1000	$1.416*10^{-9}$

For a relatively constant stress history, eq. (4) may be approximated in two different ways. The first method (simple division method) neglects the load history effects and strains are simply divided by their respective stress values at each time increment such that

$$J(t) \approx \frac{\varepsilon(t)}{\sigma(t)}. \tag{5}$$

The compliance obtained by the simple division method is also called the Specific creep compliance. The Specific creep compliance plotted on a log time scale is shown in Figure 2-14.

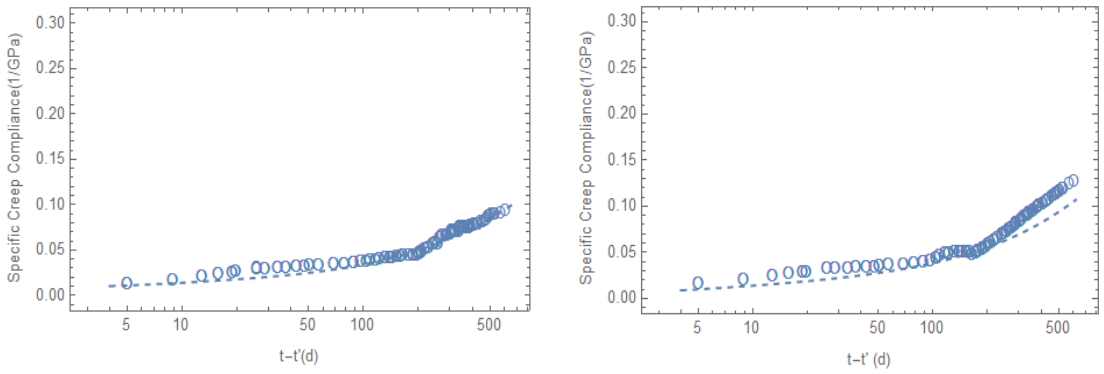

(a) 20ºC

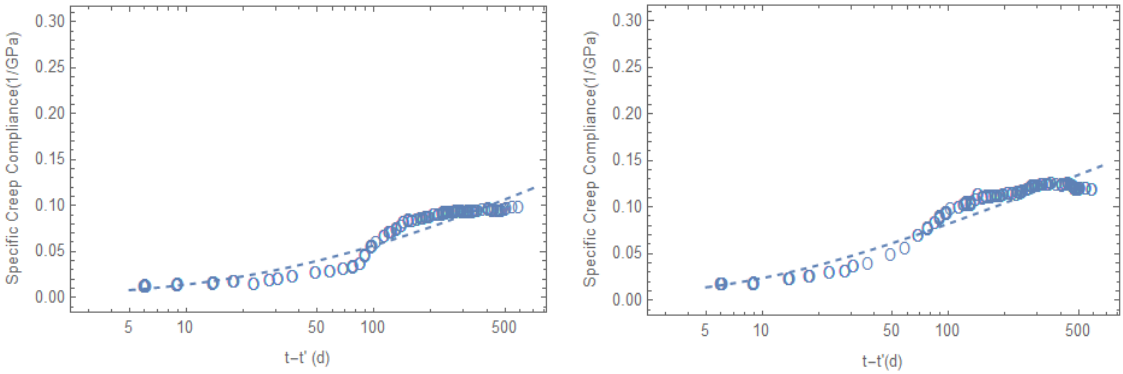

(b) 60ºC

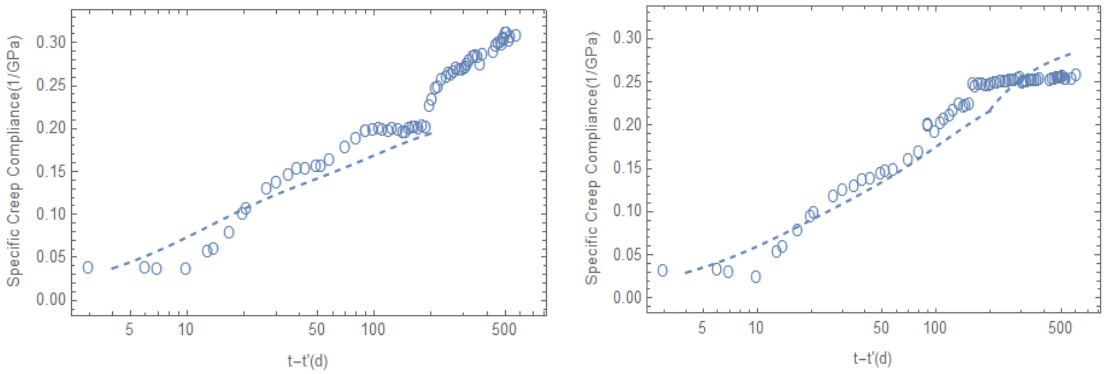

(c) 80ºC

Figure 2-14 Specific creep compliance on a log time scale for three different temperatures.

The second method (constant stress method) completely neglects the time variance in the stresses and considers the stress to be constant and equal to the initially applied stress (σ_0) such that

$$J(t) \approx \frac{\varepsilon(t)}{\sigma_0}. \tag{6}$$

The constant stress method is the method used by most researchers to calculate creep compliance. This dissertation shows the error obtained in utilizing method 2 over the constitutive equation method. Figure 2-15 shows the graph of the compliance function at different temperatures obtained using the three methods described by eqs. (4) - (6). The creep compliance clearly increases with increasing temperatures due to larger creep strains. There is insignificant variation in the $J(t)$ calculated using the three methods at 20ºC; this implies that either of the approximate methods may be used to simplify the calculations when the experiments are performed at room temperature. At higher temperatures, though, the magnitude of creep in the samples is higher causing force relaxation in the loading frame leading to greater stress decay. Assuming the load to be constant in such cases while calculating $J(t)$ can cause significant errors. There was a 42% and 60% error in predictions at 60ºC and 80ºC, respectively, while estimating $J(t)$ at 600 days after loading using the constant stress method (Figure 2-16). In comparison, the simple division method yielded only 3% and 10% error while estimating $J(t)$ at 600 days after loading at 60ºC and 80ºC respectively.

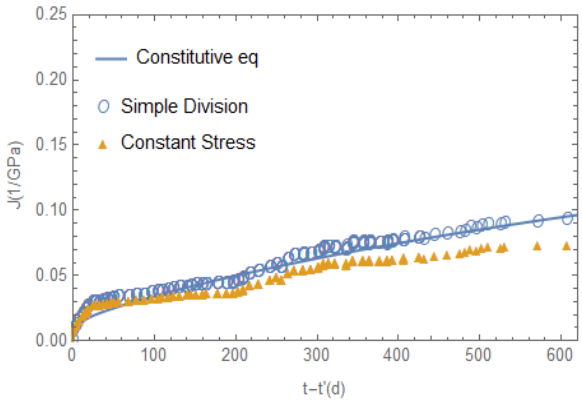

(a) 20ºC

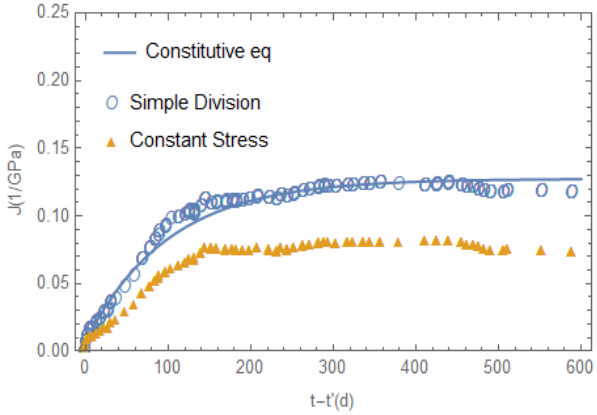

(b) 60ºC

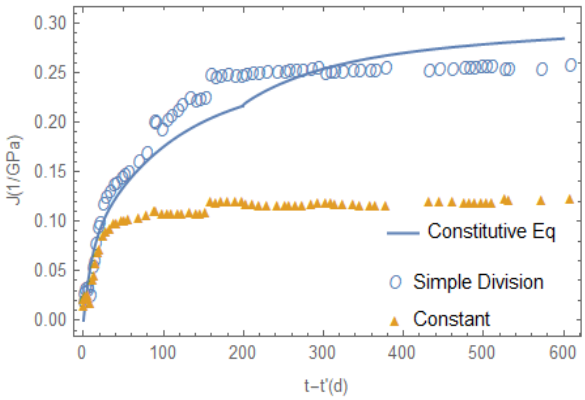

(c) 80ºC

Figure 2-15 Creep compliance functions at 20ºC, 60ºC and 80ºC calculated using three methods, (i) simple division, (ii) constant stress, and (iii) fitted constitutive equation (most accurate method to obtain $J(t)$).

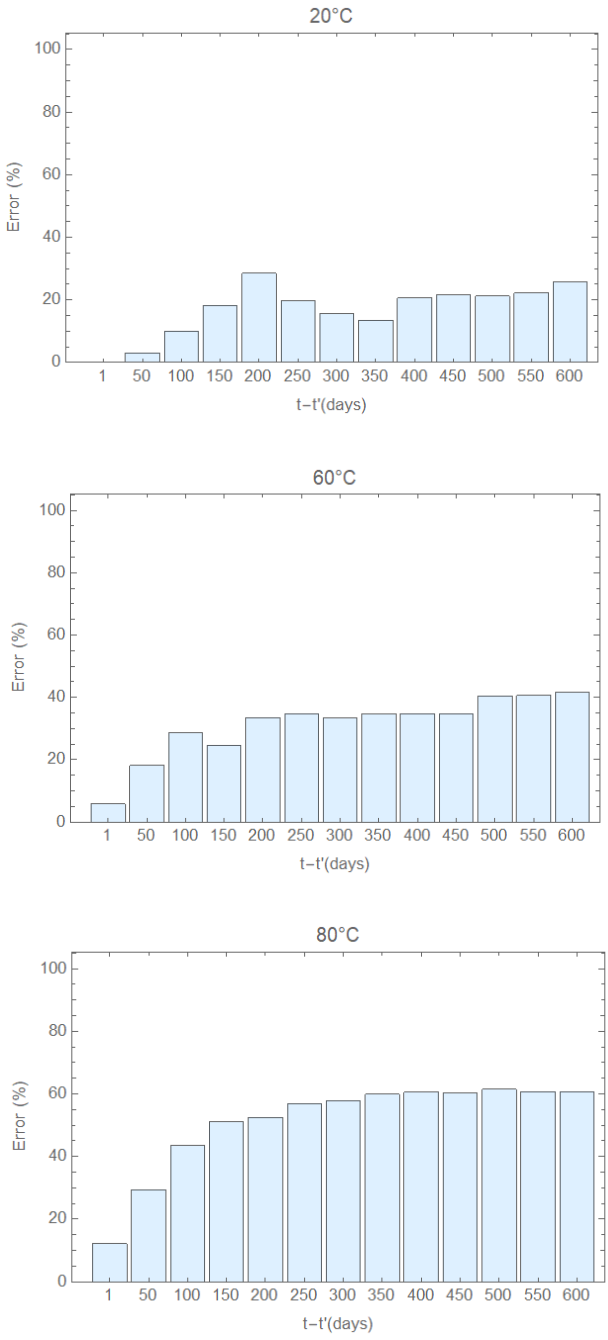

Figure 2-16 Error bars showing the increase in error with time if a constant load was assumed in estimating $J(t)$.

2.6. Evaluation of the Significance of Drying Creep in Mortar Experiments

As stated previously, the presence of free shrinkage strains in the adhesive-backed aluminum foil coated samples indicated that there was likely some external drying or self-desiccation (internal drying). Any external or internal drying would result in the presence of drying creep. Drying creep is the creep, in addition to basic creep (i.e., creep with no moisture change in the pore network), resulting under conditions of a change in moisture content of the loaded specimen. Drying creep is also referred to as the Pickett effect (Pickett 1942).

To assess significance of the drying creep component in our experiments, the B4 model was used. Using the model, the internal moisture history of the samples was back calculated using the constitutive equation relating the free strain to the average humidity history in the B4 model (Bažant et al. 2014). Then using the mix design composition and humidity profile, the basic and drying creep components of compliance were subsequently estimated using the B4 model in order to assess their relative magnitude.

2.6.1. Back Calculation of Humidity Profile

A major incorporation in the B4 model compared to its predecessor B3 model (Bažant and Baweja 2000) is that the total free strain, $\varepsilon_{sh,total}(t,t_0)$ is represented as the sum of drying shrinkage, $\varepsilon_{sh}(t,t_0)$ and autogenous shrinkage, $\varepsilon_{au}(t,t_0)$ (Bažant et al. 2014). However, the B4 model uses only the drying shrinkage in the back calculation of spatially averaged relative humidity, h. This approach was recently updated stating that individual shrinkage components cannot be modelled independently and must be considered coupled (Rahimi-Aghdam et al. 2017). Furthermore, as shown by Leung and Grasley both drying and

autogenous shrinkage (from self-desiccation) are caused by pore pressure reductions associated with reductions in the internal *h* (Grasley and Leung 2011). Hence, the authors herein use the total free strain obtained from experiments in the back calculation of humidity profile according to

$$h = \sqrt[3]{1 - \left(\frac{\varepsilon_{sh,total}(t,t_0)}{\varepsilon_{sh\infty}(t_0) \cdot S(t)} \right)}. \tag{7}$$

Here, $\varepsilon_{sh\infty}(t,t_0)$ is the "ultimate shrinkage," which in the B4 model depends on the mix design composition and the effect of aging on elastic stiffness as represented by

$$\varepsilon_{sh\infty}(t_0) = -\varepsilon_{cem} \left(\frac{a/c}{6} \right)^{p_{\varepsilon a}} \left(\frac{w/c}{0.38} \right)^{p_{\varepsilon w}} \left(\frac{6.5c}{\rho} \right)^{p_{\varepsilon c}} k_{\varepsilon a} \frac{E(7\beta_{Th} + 600\beta_{Ts})}{E(t_0\beta_{Th} + \tau_{sh}\beta_{Ts})}, \tag{8}$$

where a/c is aggregate to cement ratio, w/c is water to cement ratio, c is cement content in kg/m^3, ρ is density of mix in kg/m^3, $k_{\varepsilon a}$ is an aggregate type correction factor typically assigned a value of 1.0, E is the elastic Young's modulus, β_{Th} and β_{Ts} represent the Arrhenius factors for estimating the equivalent age at different temperatures, t_0 is the time at the onset of drying and τ_{sh} is the shrinkage halftime depending on the effective cross-section thickness (D - calculated as twice the volume to surface ratio of the sample) and the rate of drying shrinkage. The parameter ε_{cem} and exponents $\rho_{\varepsilon a}, \rho_{\varepsilon w}, \rho_{\varepsilon c}$ depend on the cement type used.

$S(t)$ is a time curve dependent on present time (t), the time at onset of drying (t_0) and shrinkage halftime (τ_{sh}) according to

$$S(t) = \tanh\sqrt{\frac{t - t_0}{\tau_{sh}}}. \tag{9}$$

The variation of h in the mortar samples as a function of time and temperature is shown in Figure 2-17. Similar to the trend observed in Figure 2-11 for free strain, h or the internal moisture of the samples is expectedly lower at 60ºC compared to 20ºC. However, at 80ºC, h is higher than 60ºC and almost resembles the 20ºC plot beyond 300 days. This could be attributed to the fact that at temperatures above 60ºC, the enhanced formation and occupancy of hydration products around the pores suppresses moisture loss due to drying.

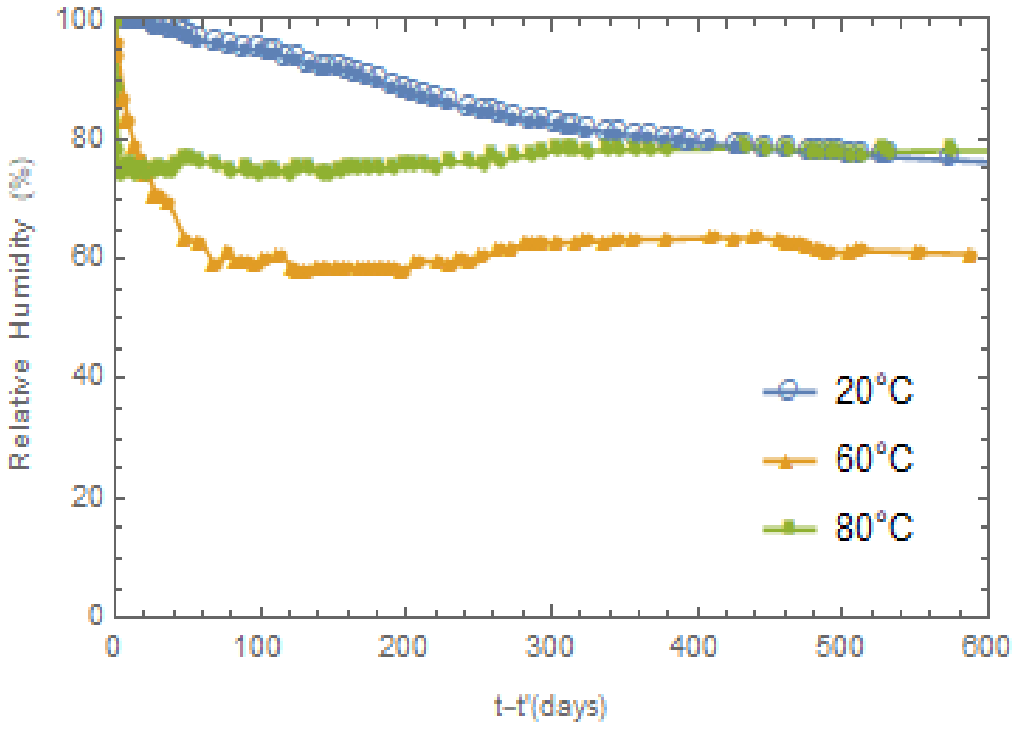

Figure 2-17 Spatially averaged relative humidity (h) **inside the mortar samples back-calculated using the free strain history.**

2.6.2. Basic and Drying Creep

According to the B4 model, the creep compliance of a specimen exposed to the atmosphere and undergoing drying during a creep test can be expressed using

$$J(t,t') = q_1 + R_T C_0(t,t') + C_d(t,t',t_0), \tag{10}$$

where, q_1 is the instantaneous strain due to unit stress, $C_0(t,t')$ is the compliance due to basic creep, $C_d(t,t',t_0)$ is the additional compliance due to drying, and R_T is a multiplicative factor for basic creep at elevated temperatures. Bažant's B4 model illustrates a step-by-step procedure to calculate the basic and drying creep compliance functions (Bažant et al. 2014). The compliance due to basic creep is calculated from the mix composition and design strength from

$$C_0(t,t') = q_2 Q(t,t') + q_3 \ln[1+(t-t')^n] + q_4 \ln(t/t'), \tag{11}$$

where, q_2, q_3 and q_4 are empirical constitutive parameters that represent the aging viscoelastic compliance, non-aging viscoelastic compliance and flow compliance respectively, as deduced from the solidification theory. The function, Q can be obtained by numerical integration and is a function of t and t'. The empirical parameter n is usually assumed to be 0.1. The multiplicative factor, R_T is given as

$$R_T = \exp\left[\frac{U_c^{'}}{R}\left(\frac{1}{293} - \frac{1}{T+273}\right)\right], \tag{12}$$

where $U_c^{'}$ is the effective activation energy for creep, R is the universal gas constant and T is the average test temperature in ^oC.

The compliance due to drying is given by

$$C_d(t,t',t_0) = q_5[\exp\{-8H(t)\} - \exp\{-8H(t_0')\}]^{1/2} \quad (13)$$

where, $$H(t) = 1-(1-h)S(t)\,. \quad (14)$$

Here, h is obtained from back calculation of free strain data, $S(t)$ is the time dependence function, q_5 is an empirical constitutive parameter and t_0' is the time when drying and loading act simultaneously.

The total compliance function was obtained using eq. (10). Figure 2-18 depicts a comparative representation of the total creep compliance and the basic and drying creep compliance components at 20ºC, 60ºC and 80ºC, as predicted by the B4 model.

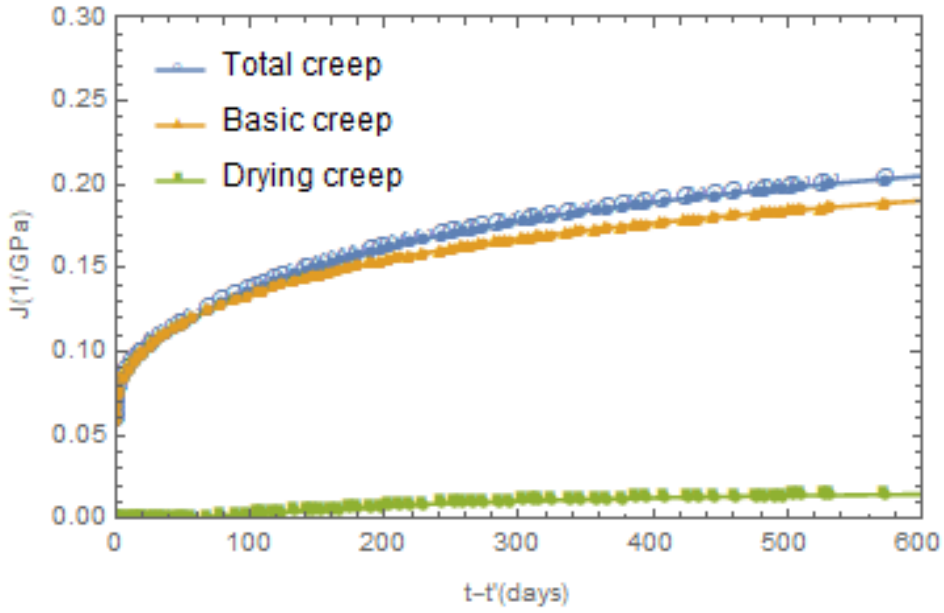

(a) 20ºC

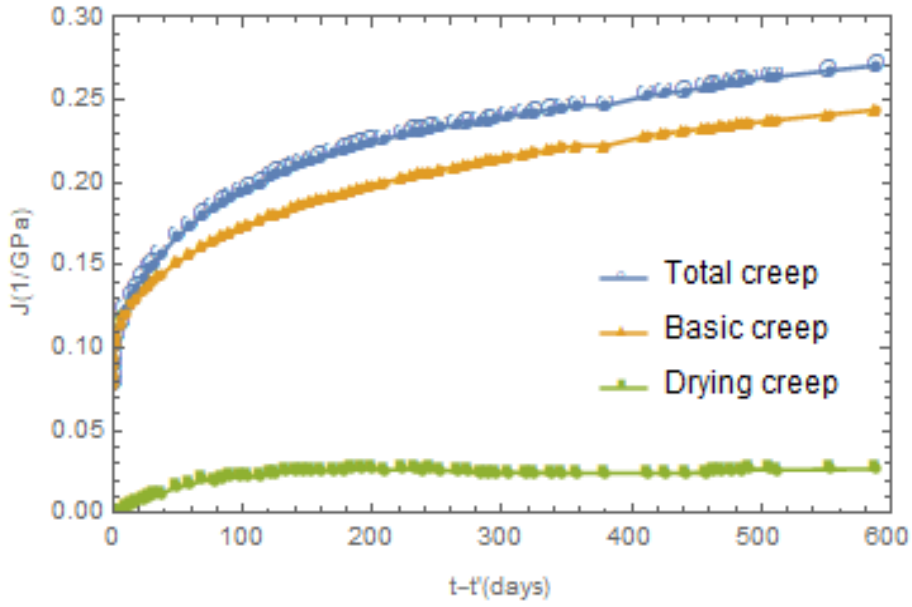

(b) 60ºC

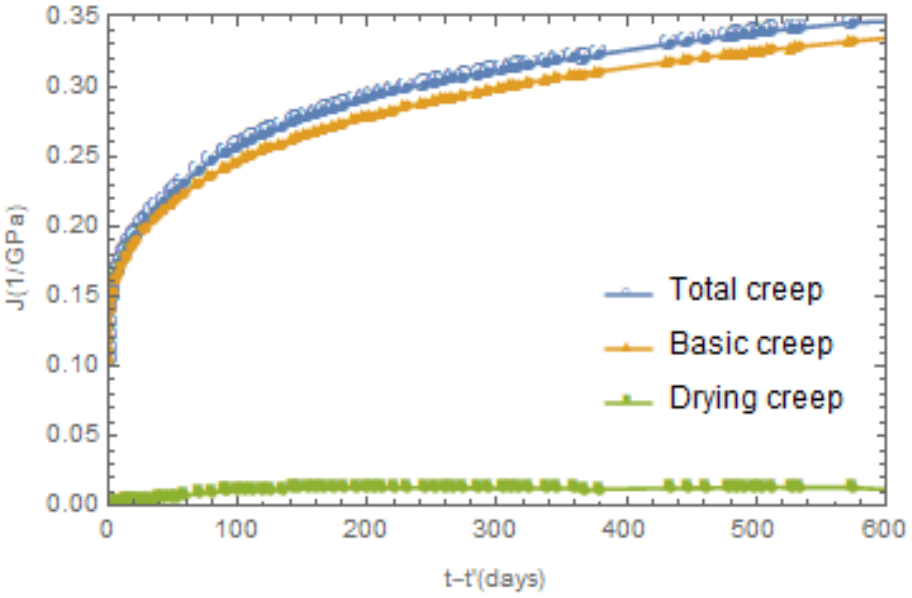

(c) 80ºC

Figure 2-18 B4 model used to depict the negligible impact of drying creep compliance in the calculation of total creep compliance.

From Figure 2-18, it is clear that the compliance due to drying is negligible compared to the total compliance function. The compliance function obtained from the creep experiments may thus be approximated as entirely due to basic creep compliance.

In addition to using the B4 model to evaluate the significance of drying creep in the mortar experiments, the experimentally measured basic creep compliance was compared against the basic creep compliance calculated using both the B3 and B4 model (Figure 2-19).

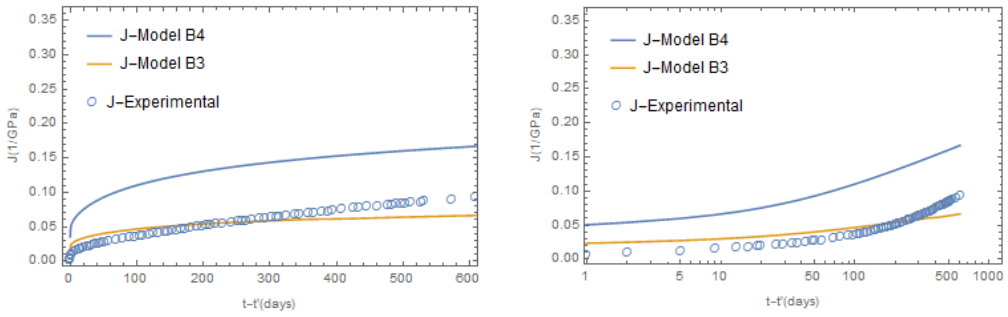

(a) 20ºC

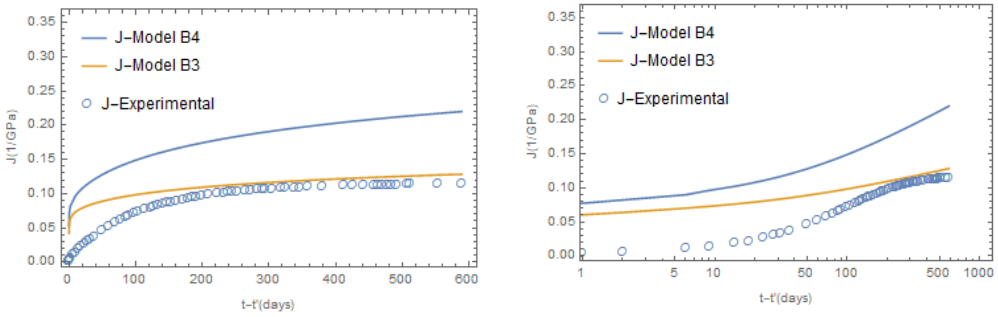

(b) 60ºC

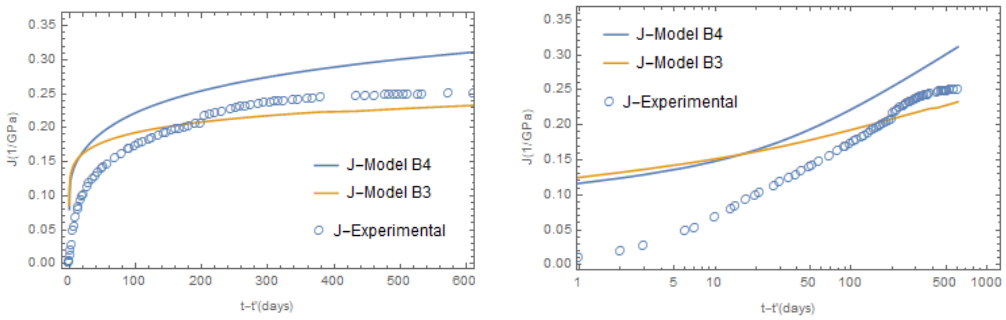

(c) 80ºC

Figure 2-19 The basic creep compliance from the experiment plotted against the basic creep compliance from the B3 and B4 model in regular and log time scale.

Figure 2-19 shows that the B3 model fits more accurately with the experimental data compared to the B4 model. This is explained in Fig. D10. (a). of the Creep and Hygrothermal Effects in Concrete Structures book (Bažant and Jirasek 2018), which shows that the total creep predicted using B4 model is always higher compared to the B3 model due to differences in the creep parameters used for predicting compliance. Another major finding is that neither B3 or B4 model seem to accurately predict long-term creep compliance of the mortar tested in the research reported here.

2.7. Creep Compliance Master Curve for Cement Mortar using TTS Principle

The basic creep compliance curves obtained at 20°C, 60°C and 80°C by fitting the experimental data using the constitutive equation method were plotted on a logarithmic time axis. All creep compliance curves were similar shapes, implying that the material was thermorheologically simple. Hence the creep compliance curves at 60°C and 80°C

were shifted laterally to the right using the TTS principle to obtain a creep compliance master curve at room temperature (20°C) as shown in Figure 2-20.

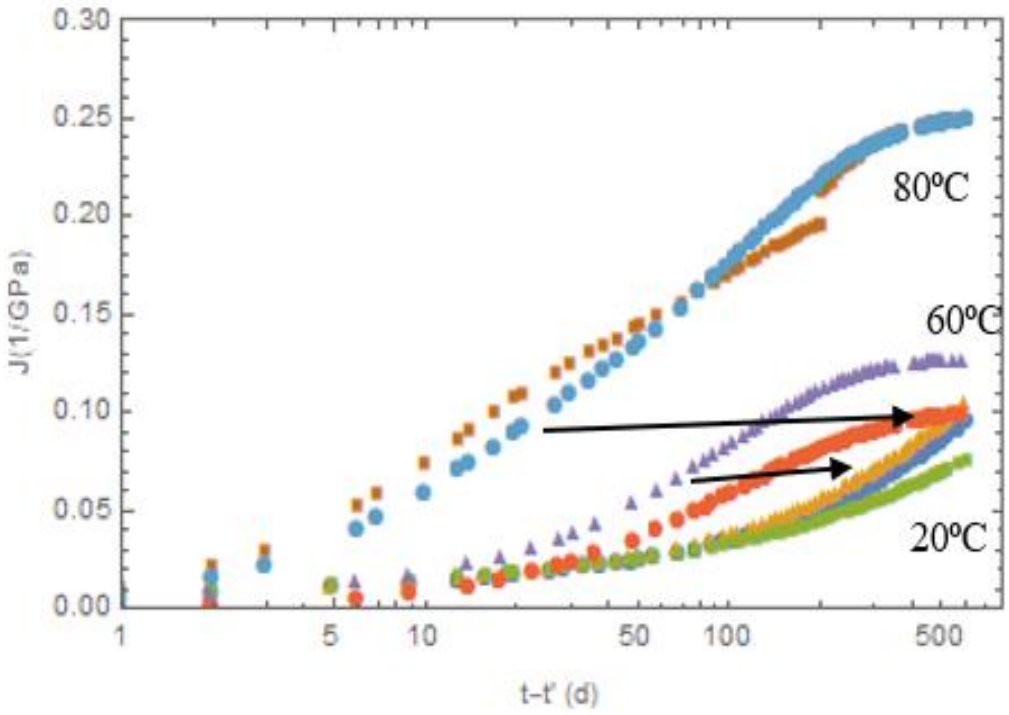

Figure 2-20 Creep compliance functions at 60°C and 80°C shifted along the logarithmic time axis to produce a creep compliance master curve at 20°C.

The temperature dependent shift factor, β_{Tc} that is needed to shift the curve laterally is calculated as

$$\beta_{Tc} = \frac{t}{t_r}, \qquad (15)$$

where t is the present time and t_r is the reduced time. In this study, a β_{Tc} value of 4 was calculated for 60°C and 37 for 80°C to shift the creep compliance data from higher temperatures to 20°C reference temperature (β_{Tc} =1 at 20°C) (Table 2-3).

Table 2-3 Shift factors for different temperatures for cement mortar with respect to the reference temperature.

Temperature	Shift Factor
20ºC	1
60ºC	4
80ºC	37

A creep compliance master curve was obtained to predict creep of cement mortar for up to 22,500 days ~ 60 years using creep experiments performed for 600 days. The shifted data was fitted into a five-unit logarithmic chain shown in equation 9. The unit of creep compliance has units of 1/GPa.

$$J(t) = 0.03055 Log\left[1 + \frac{t}{10000}\right] + 0.01273 Log\left[1 + \frac{t}{1000}\right] + 0.03434 Log\left[1 + \frac{t}{100}\right] - 3.9327 x10^{-10} Log\left[1 + \frac{t}{10}\right] + 0.00248 Log\left[1 + t\right] \quad (16)$$

The creep compliance master curve is presented in Figure 2-21. The master curve allows for predicting creep in structures for several decades beyond the range of the original results obtained using laboratory creep experiments.

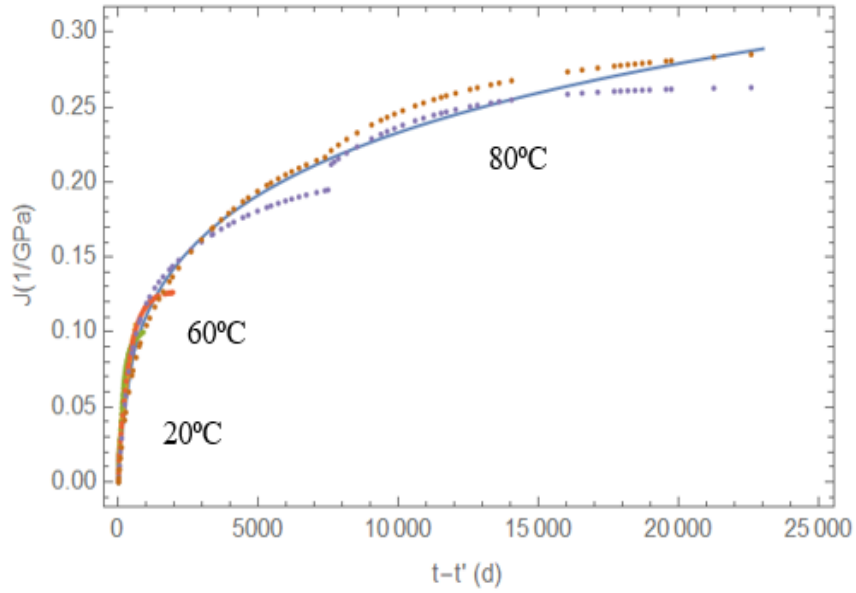

(a)

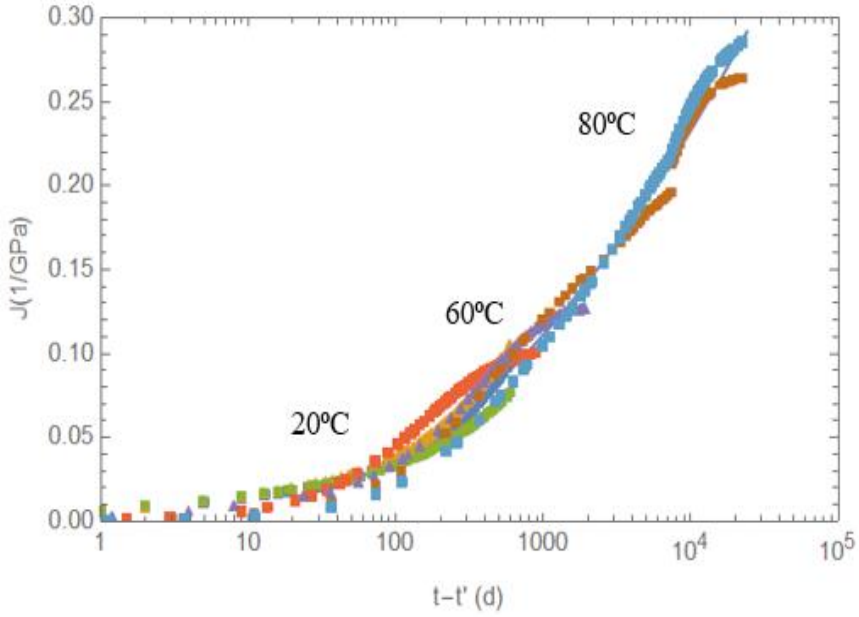

(b)

Figure 2-21 Creep compliance master curve in (a) normal time scale and (b) logarithmic time scale.

2.7.1. Implications for Understanding Creep Mechanism

The effect of temperature on the kinetics of chemical or deformation processes is often modeled by the Arrhenius function according to

$$\beta_{Tc} = \exp\left[\frac{U_c}{R}\left(\frac{1}{293} - \frac{1}{T}\right)\right], \tag{17}$$

where R is the universal gas constant (8.314 J/mol.K), T is temperature in kelvins, and U_c is an activation energy. The experimentally determined shift factors at two different temperatures yielded a best fit ($R^2 = 0.88$) activation energy of 46.4 kJ/mol (Figure 2-22). This activation energy is consistent with hydration of a typical Portland cement (after the first few hours of mixing), with a carefully measured activation energy of 48.3 ± 2.1 kJ/mol (Thomas 2012). While others have noted that the activation energy for hydration and creep are similar, the implication of this similarity does not seem to have been thoroughly discussed. It has been proposed that, after the first few hours of mixing, the kinetics of the hydration reaction – and thus the activation energy – are controlled by the diffusion of ions or water through the hydration product shell (Rahimi-Aghdam et al. 2017). Li et al. (Li et al. 2018) suggested that long-term creep of cementitious materials occurs largely due to stress-induced dissolution of the hydration products, a concept that was experimentally supported by Maradian et al. (Moradian et al. 2018) and Pignatelli et al. (Pignatelli et al. 2016). Li et al. argue that stress-induced dissolution occurs because of an upset in the thermodynamic equilibrium between hydration products and pore solution speciation due to the addition of a strain energy term. The magnitude of the internal energy gradient influencing the kinetics of the dissolution process in such a situation is a function

of the diffusion rate of the ions or water through the hydration products. Thus, if both hydration and creep are rate controlled by diffusion through hydration products, it is sensible that the activation energy for both processes are nearly identical.

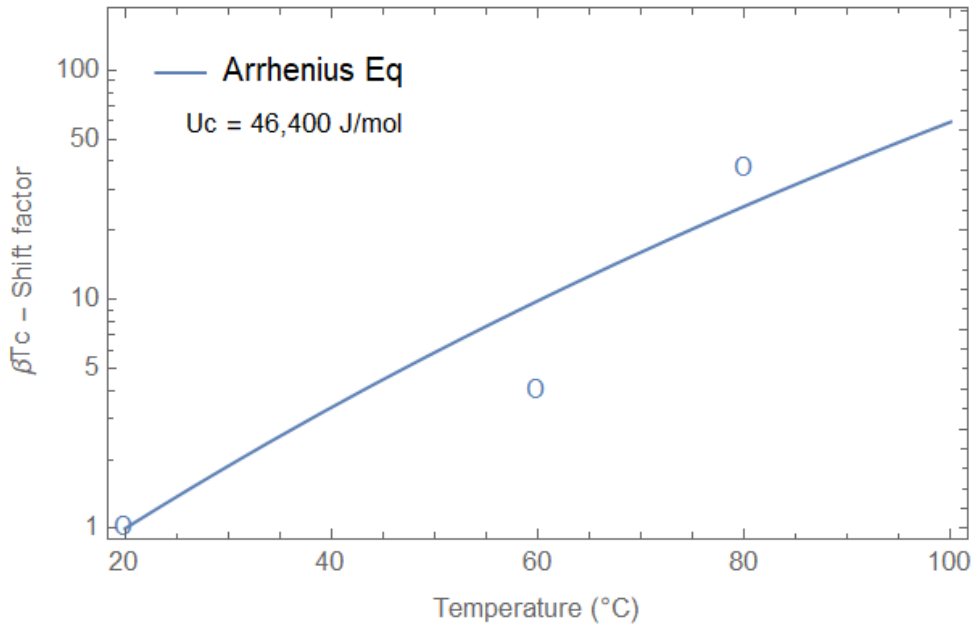

Figure 2-22 The experimentally determined shift factor with Arrhenius equation at activation energy of U_c = 46.4 Kj/mol yielded a best fit of R^2 =0.88.

2.8. Summary and Conclusions

In this study, the long-term creep response of cement mortar was examined by conducting creep tests using a mix design resembling the VeRCoRs mortar used by EDF. A custom-built miniaturized creep frame was designed to fit inside climatic chambers and allow creep tests to be run at 20°C, 60°C and 80°C for 600 days. The use of cement mortar mixes in lieu of concrete combined with the reduction in creep frame size reduced the cost and time involved in conducting the creep experiments while improving the resolution of the measurements. The following conclusions may be drawn:

- The magnitude of creep strain measured after 600 days increased by a factor of 1.50 and 2.40 at 60ºC and 80ºC, respectively, compared to the creep strain at 20ºC.
- Creep compliance was calculated using three methods for all test conditions based on the measured creep strain and the applied stress. Neglecting the time variance in stress (constant stress method) did not significantly impact the accuracy of creep compliance predictions at 20ºC but resulted in a 42% and 60% error (600 days after loading), respectively, at 60ºC and 80ºC. Similarly, the simple division method resulted in up to 10% error in creep compliance at higher temperatures. At higher temperatures, it is recommended to properly account for the stress history during the experiment by utilizing the convolution integral constitutive equation when calculating the compliance.
- The Bažant B4 model was applied to illustrate that drying of the mortar samples during the creep tests was negligible and hence the total creep compliance measured was almost entirely due to basic creep. The relative humidity inside the cement mortar sample was back-calculated using the free strain data. Although some free strain was observed due to moisture loss, it did not correlate with significant drying creep.
- For the first time, the TTS principle was successfully used to generate a creep compliance master curve to predict mortar creep response for up to 22,500 days (nearly 60 years) at a reference temperature of 20°C. A constitutive equation for creep compliance was also proposed to accompany the master curve. By

running creep tests at 80°C, creep at 20°C was predicted at 37 times the time duration of the 80°C test using temperature shifting. In summary, this study demonstrates that the TTS principle can be effectively deployed to predict long term creep of cement-based materials.

- The activation energy for mortar creep is essentially the same as the activation energy for cement hydration. Since hydration rate is suggested to be diffusion controlled, the implication is that long-term creep rate may also be diffusion controlled. Such a hypothesis is in agreement with the stress-induced dissolution mechanism of creep previously proposed.

References

1. Aili, A.: Shrinkage and creep of cement-based materials under multiaxial load: poro-mechanical modeling for application in nuclear industry. Mater. Université Paris-Est. (2017).
2. Bažant, Z. P.: Theory of Creep and Shrinkage in Concrete Structures: A Precis of Recent Developments. Reprinted from Mechanics Today, **2** (1), 1-93 (1975).
3. Bažant Z. P., Panula, L.: Practical prediction of time-dependent deformations of concrete. Mater. Struct. (RILEM, Paris) **11**, 307–316, 317–328, 415–424 (1978).
4. Bažant, Z. P.: Mathematical Modeling of Creep and Shrinkage of Concrete. Wiley, Chichester (1988).
5. Bažant, Z. P., and Xi, Y.: New test method to separate microcracking from drying creep: Curvature creep at equal bending moments and various axial forces. Proc., 5th

International RILEM Symposium on Creep and Shrinkage of Concrete (ConCreep 5), held at U.P.C., Barcelona (1993).

6. Bažant, Z. P. and Baweja, S.: Creep and Shrinkage Prediction Model for Analysis and Design of Concrete Structures: Model B3. Am. Concrete Institute, Michigan, 1–83 (2000).
7. Bažant, Z. P., Cusatis, G. and Cedolin, L.: Temperature Effect on Concrete Creep Modeled by Microprestress-Solidification Theory. J. Eng. Mech. **130** (6), 691-699 (2004).
8. Bažant Z. P., Hubler, M., Wendner, R.: Model B4 for creep, drying shrinkage and autogenous shrinkage of normal and high-strength concretes with multi-decade applicability. TC-242-MDC multi-decade creep and shrinkage of concrete: material model and structural analysis. RILEM Mater Struct. (2014).
9. Bažant, Z. P., Jirasek, M.: Creep and Hygrothermal Effects in Concrete Structures. Sol. Mech. Appl. **225** (2018).
10. Brooks, J. J.: 30-year creep and shrinkage of concrete. Mag. Concr. Res. **57** (9), 545-556 (2005).
11. Christensen, R.: Theory of Viscoelasticity, Dover (2003).
12. Drozdov, A.: Viscoelastic Structures - Mechanics of Growth and Aging, Academic Press, (ISBN 0-12-388589-2) (1998).
13. EDF: Vercors an experimental mock-up of a reactor containment building. http://researchers.edf.com/research-activities/generation/vercors-an-experimental-mock-up-of-a-reactor-containment-building-290900.htm (2014).

14. Grasley, Z. C.: Measuring and Modeling the Time-dependent Response of Cementitious Materials to Internal Stresses. Ph.D, Univ. of Ill. (2006).
15. Grasley, Z. C., Leung, C. K.: Desiccation shrinkage of cementitious materials as an aging, poroviscoelastic response. Cem. Concr. Res., **41** (1), 77-89 (2011).
16. Grasley, Z. C., Jones, C. A., Li, X., Garboczi, E. J., Bullard, J. W., ed.: Elastic and viscoelastic properties of calcium silicate hydrate. NICOM 4: 4th Int. Symp. Nanotechnol. in Constr. May 20-22 (2012).
17. Hernández, W. P., Castello, D, A., Roitman, N., Magluta, C.: Thermorheologically simple materials: A bayesian framework for model calibration and validation. J. Sound Vib., **402**, 14-30 (2017).
18. Jordaan, I. J.: Analysis of creep in concrete structures under general states of stress, seminar on concrete structures subjected to triaxial stresses. Italy, 111-118 (1974).
19. Ladaoui, W., Vidal, T., Sellier, A. and Bourbon, X.: Effect of a temperature change from 20 to 50ºC on the basic creep of HPC and HPFRC. Mater. Struct. **44** (9), 1629-1639 (2011).
20. Li, X., Rahman, S. and Grasley, Z. C.: Modeling creep and relaxation caused by phase dissolution. B. Antoun (ed.) Challenges in Mech. Time-Depend Mater. **2**, 73-81 (2016a).
21. Li, X., Rahman, S. and Grasley, Z. C.: Computationally implemented modeling of creep of composite materials caused by phase dissolution. Comput. Mater. Sci. **125**, 61-71 (2016b).

22. Li, X., Grasley, Z. C., Bullard, J. W., Feng, P.: Creep and relaxation of cement paste caused by stress-induced dissolution of hydrated solid components. J. Am. Ceram. Soc. **101**, 4237– 4255 (2018).
23. Mc Donald, J. E.: Time dependent deformation of concrete under multiaxial stress conditions. In: Technical Report C-75-4 Concrete Laboratory, US Army Engineering Waterways Experiment Station, Vicksburg, MS (1975).
24. Mindess, S, Young, F. J. and Darwin, D. Concrete. 2nd. ed. Pearson Education, Inc. (2003).
25. Moradian, M., Ley, M. T., Grasley, Z. C.: Stress induced dissolution and time-dependent deformation of portland cement paste. Mater. & Des. **157**, 314-325 (2018).
26. Nasser, K. W. and Neville, A. M.: Creep of Concrete at Elevated Temperature. ACI J. Proc. **62** (12), 1567-1579 (1965).
27. Neville, A. M.: Theories of Creep in Concrete. ACI J. Proc. **52** (1955).
28. Pickett, G.: The Effect of Change in Moisture Content on the Creep of Concrete Under a Sustained Load. ACI J. **38**, 333-355 (1942).
29. Pignatelli, I., Kumar, A., Alizadeh, R., Pape, Y. L., Bauchy, M., Sant, G.: A dissolution-precipitation mechanism is at the origin of concrete creep in moist environments. J. Chem. Phys. **145** (2016).
30. Rahimi-Aghdam, S., Bažant, Z. P., Qomi, M. A.: Cement hydration from hours to centuries controlled by diffusion through barrier shells of CSH. J. Mech. Phys. Sol. **99**, 211–224 (2017).

31. Rahman, S., Grasley, Z. C., Masad, E., Zollinger, D., Iyengar, S., Kogbara, R.: Simulation of mass, linear momentum, and energy transport in concrete with varying moisture content during cooling to cryogenic temperatures. Transp. Porous Media, **112** (1), 139-166 (2016).
32. Schwarzl, F. and Staverman, A. J.: Time-Temperature Dependence of Linear Viscoelastic Behavior. J. Appl. Phys. **23** (1952).
33. Sjöberg, E. L.: A fundamental equation for calcite dissolution kinetics. Geochim. Cosmochim. Acta, **40**, 441-447 (1976).
34. Thomas, J.J.: The Instantaneous Apparent Activation Energy of Cement Hydration Measured Using a Novel Calorimetry-Based Method. J. Am. Ceram. Soc. **95** (10), 3291–3296 (2012).
35. Torrence, C., Baranikumar, A. and Grasley, Z. C.: Nuclear concrete microstructure generation and analysis of long-term performance. 19th International Conference on Environmental Degradation of Materials in Nuclear Power Systems – Water Reactors, Boston, Am. Nucl. Soc. (2019).
36. Tulin, L. G. Creep of Portland cement mortar as a function of time. Iowa state university (1965).
37. Vidal, T., Sellier, A., Ladaoui, W., and Bourbon, X.: Effect of temperature on basic creep of High-Performance Concretes heated between 20ºC and 80ºC. J. Mater. Civil Eng. **27** (7) (2015).
38. Wang, J., Yan, P., Yu, H.: Apparent activation energy of concrete in early age determined by adiabatic test. J Wuhan Univ. Tech. Mater. Sci. **22** (3), 537–541 (2007).

39. Zhou, Q., Beaudoin, J. J.: Effect of applied hydrostatic stress on the hydration of Portland cement and C3S. Adv. Cem. Res. **15**, 9- 16 (2003).

3. CONFINED CREEP RESPONSE OF CEMENT MORTAR

This chapter focusses on the confined creep test and modeling of the 3D creep response of cement mortar. The properties and models developed in this chapter is used as input to model concrete response to creep using computational approach in an companion study.

3.1. Introduction

Though creep of concrete has been a subject of interest for several decades, attention has mainly been devoted to creep under a uniaxial stress condition. However, in reinforced and prestressed structures, a three-dimensional state of stress generally exists, which can complicate the response of the structure. To understand the behavior of concrete under multiaxial compression, the Poisson's ratio of the viscoelastic material plays a crucial role to determine the long-term deformation response and durability performance of concrete (Bernard et al., 2003).

Some investigators have studied the viscoelastic/viscoplastic Poisson's ratio (VPR) of concrete, but the results reported from different studies are contradictory. For example, it has been suggested that VPR is an increasing, decreasing, and constant function of time in separate studies. Such uncertainty arises mainly from the fact that the VPR is measured or calculated differently by different researchers. Ross was the first to conduct creep tests on concrete under 2D loading and suggested that the creep Poisson's

ratio (CPR)[1] is close to zero (Ross, 1954). His experiments showed that creep in the direction of major stress in 2D testing reaches a magnitude of the same order as that under simple 1D stress of same intensity. A few years later, Gopalakrishnan reported that under multiaxial stress conditions, the CPR was lower than the uniaxial Poisson's ratio and that there was no variation in CPR with time (Gopalakrishnan et al., 1969). The CPR was calculated separately for each direction using the knowledge of the uniaxial compliance. Gopalakrishnan also argued that the CPR was a function of the magnitude of stress.

Jordaan and Illston calculated CPR as the ratio of the total mechanical strains (i.e., the sum of elastic and creep strains) in the axial and lateral directions (Jordaan and Illston, 1969). They proposed four different expressions for calculating CPR under different loading conditions (uniaxial, biaxial, triaxial with uniaxial system, triaxial with octahedral shear stresses). The effective Poisson's ratio for all cases remained constant and equal to the Poisson's ratio in an elastic state (Jordaan and Illston, 1969). In 1974, Parrott measured the lateral strains from uniaxial tests on cement paste to determine the Poisson's ratio (Parrott, 1974). He used the creep strains (the total strain minus the elastic and shrinkage strains) to calculate the CPR. The CPR was found to be a constant value equal to 0.13 (Parrott, 1974). Kesler found that the CPR of concrete that was sealed during loading to be almost equal to the elastic Poisson's ratio, however it was considerably smaller if allowed to dry under load (Kesler, 1977). Lakes demonstrated that composite structures

[1] Note that CPR is determined by the negative ratio of transverse to axial strains in a constant stress (creep) test. As will be noted later in the paper, CPR is not generally equivalent to VPR.

may exhibit increasing or decreasing Poisson's ratio with time (Lakes, 1992). He also proposed that time dependent VPR need not be monotonic in nature, where a composite can be constructed that can have a decreasing Poisson's ratio with time initially followed by an increasing function. Hilton cited five different expressions for time-dependent Poisson's ratio and identified VPR's strong dependence on stress histories (Hilton, 2001). Grasley and Lange computed the VPR of sealed cement paste using the correspondence principle. They found that under multiaxial loading, the VPR of cement paste is relatively constant with time and then gradually increases as dilatational compliance comes to a halt (Grasley and Lange, 2007).

More recently in 2015, Aili used various multiaxial creep test data from literature to show the difference between the CPR and relaxation Poisson's ratio (RPR – equivalent to the VPR). In spite of the two Poisson's ratio not being equal (Tschoegl et al. 2002; Lakes and Wineman, 2006) the initial and long-term asymptotic values and their corresponding time derivatives were found to be the same (Aili et al., 2015). In another study, Aili found the VPR for a mature concrete to be constant and ranging between 0.15 and 0.20 (Aili et al., 2016). Charpin conducted a 10-year concrete creep study under uniaxial and biaxial conditions in which the evolution of the CPR was discussed. Their experimental data showed that the assumption of a constant Poisson ratio for concrete is reasonable (Charpin et al., 2015). In 2017, Charpin and Sanahuja established through examples, both theoretical and practical, that any evolution of Poisson's ratio: increasing, decreasing or non-monotonic is possible for concrete (Charpin and Sanahuja, 2017). In summary, there is a large scatter in the reported VPR from different studies at room

temperatures. A possible reason that could partly explain this large scatter in data is that the experiments were performed under varying test conditions. Also, the laboratory measurement of axial and lateral strains is challenging as they highly depend on the resolution of strain gages used. Overall, these conditions make multiaxial creep tests strenuous and time-consuming, thereby serving as a motivation for researchers to develop more effective methods to evaluate VPR.

Data on the Poisson's ratio of concrete at elevated temperatures are scarce and limited. At ambient temperature, the Poisson's ratio of concrete can vary between 0.15 and 0.20 (Atheel, 1981; Aili et al., 2016). A study by Ehm in 1985, suggests that the Poisson's ratio decreases with increasing temperatures due to weakening of the microstructure by breakage of bonds at higher temperatures (Ehm, 1985). For a concrete under confining pressure, as it would be in many nuclear power plant concrete structures, it has been hypothesized that Poisson's ratio at elevated temperature would be about the same as at room temperature (NRC, 2010).

All the above studies are either for elastic Poisson's ratio at elevated temperatures or VPR at room temperature. The authors have not found any data in the literature on VPR for concrete, mortar, or cement paste at elevated temperatures. In the current study, the authors utilize a confined creep test that can fully capture the 3D constitutive properties of cement mortar in a single experiment. As concrete creep is entirely due to the creep within the cement paste phase, since the behavior of aggregates is typically linear elastic (Bažant, 1975), the sensitivity of concrete creep to both temperature and multi-axial loading can be captured by cement mortar experiments. The focus on cement mortar

samples rather than concrete enables the use of smaller sized specimens with enhanced measurement resolutions. For this purpose, a smaller creep frame is designed that can fit in climatic chambers to facilitate testing at elevated temperature. The confined creep test allows the simultaneous measurement of bulk and shear compliance, which is used to determine the uniaxial compliance and VPR through intermodulus conversion via the correspondence principle (Grasley and Lange, 2007). The temperature-dependency of VPR is analyzed by running confined creep tests at room temperature (i.e., 20ºC) and elevated temperature (i.e., 60ºC). Hence, this research aims to improve the understanding of the viscoelastic behavior of cement mortar under multiaxial loading as a function of time and temperature.

3.2. Experimental Design

3.2.1. Mix Design

The cement mortar mix design used for the confined test is the same as that of the uniaxial creep test. The mixture proportions used are shown in Table 2-1 of chapter 2 and referenced in EDF (EDF, 2014).

3.2.2. Confined Creep Frame Design

Similar to the standard ASTM C512 concrete creep frames, a unique miniature version of the creep frame was designed and fabricated exclusively for cement mortar samples of dimensions 50 mm radius x 100 mm height (2 in. radius x 4 in. height) as shown in Figure 3-1. The total height of the scaled down frame is only 45 cm (18 in.) as opposed to approximately 180 cm (6 ft.) tall standard concrete creep frames. The diameter of the frame is 10 cm (4 in.), making the frames easier to be placed inside temperature ovens and

climate chambers. The creep frame has a compression spring at the bottom of the frame that helps to maintain a nearly constant load. Above the spring is a plate with a ball bearing at the center to ensure minimum eccentricity in loading. An inline load cell is placed just below the sample to record the load levels in the frame. Although load levels are intended to be constant during a creep test, the actual load level was recorded periodically to account for any load loss. A 5-ton mini hydraulic jack was used to apply the initial axial force. Threaded rods and nuts were used in the frame to maintain compression of the spring and a relatively constant load after removal of the hydraulic jack.

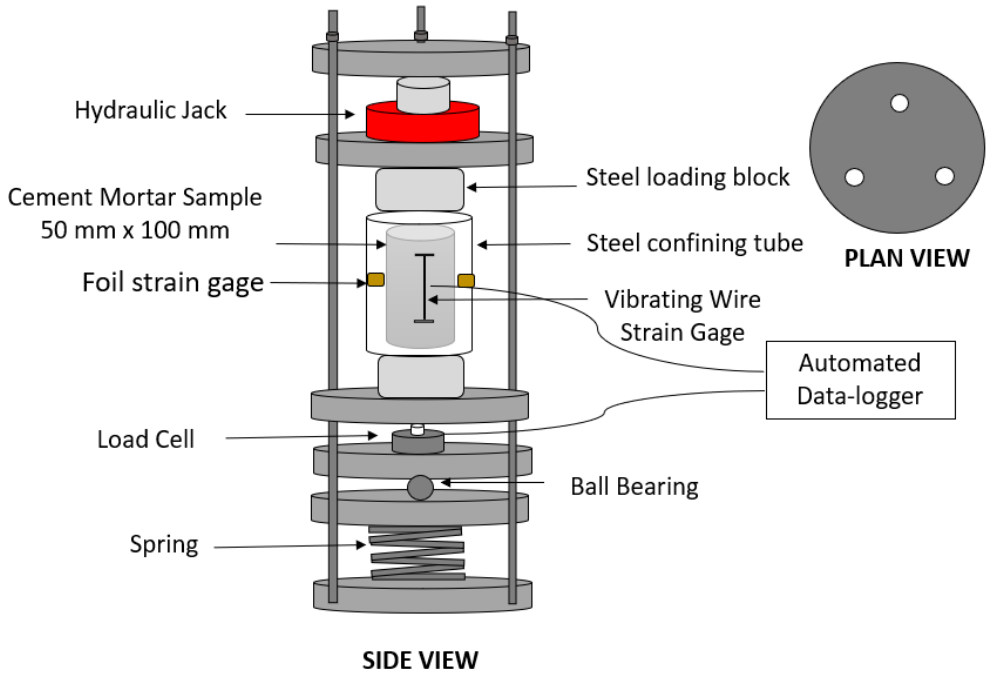

Figure 3-1 Miniaturized compressive creep test frame for cement mortar. This frame is 45 cm (18 in.) in total height and is a scaled down version of ASTM standard concrete creep frame which is approximately 180 cm (6 ft.) in height.

Cement mortar was mixed in accordance to ASTM C305-99 and immediately cast into a 304L stainless steel confining tube of 2 mm (0.07 in.) thickness (54 mm outer diameter and 50 mm inner diameter) and 100 mm (4 in.) height. Embedded vibrating wire gages with gage length of 50 mm (2 in.) from Geokon were mounted axially at the center of the confining tubes using fishing line before pouring the mix. The cylinders were filled in three equal increments and tapped after each increment to minimize air voids. Both ends of the confining tube were sealed using tightly fitted caps. After 24 hours, the end caps were removed, and the sample was pushed slightly outside the tube on either end separately to smoothly cut the surface using a diamond blade wet saw. This procedure ensures that the bond between the sample and the confining tube is broken and the contact between them can be approximated as frictionless. To measure the hoop strain, 4 sets of foil strain gages (C2A-13-250LW-120) from Micro Measurements were mounted on the outer radial surface of the steel tube. The foil strain gages were placed diametrically opposite to each other and in the circumferential direction. A steel loading block with a diameter of 49 mm (1.9 in.) and height of 50 mm (1.9 in.) was placed on both ends of the sample. The loading block diameter was slightly less than the inner diameter of the confining steel tube so that it can easily slide through the tube while also ensuring uniform compressive stress throughout the sample cross-section.

The cement mortar specimens were cured at room temperature for 28 days before starting the test. At 28 days, the samples were loaded using a hydraulic jack to a constant load of approximately 1905 kg (4200 lbs), which corresponded to 25% of 28-day compressive strength of mortar; f'_c = 37.23 MPa (5400 psi) at 28 days. At this loading age

and stress magnitude, the mature cement mortar was assumed to be a non-aging, linear viscoelastic material. The load was approximated as a stepwise load function given the very short time span of load application relative to the overall duration of the creep test. The axial strain from the vibrating wire gage as well as the load readings from the load cell were recorded every 30 minutes using a CR300 Data logger, AM16/32B Multiplexer and a 2-Channel Vibrating-Wire Analyzer (AVW200) from Campbell Scientific. The foil strain gages that read hoop strain were connected to a Student D4 data acquisition system from Micro Measurements using quarter bridge circuits. As mentioned earlier, creep tests were run at 20°C and 60°C. At 60°C, the creep frame and the sample were heated to the test temperature before starting the confined creep test (to avoid the accumulation of thermal strains during creep). The experiments were conducted in environmental chambers maintained at constant temperature (Figure 3-2). The relative humidity was consistent at 50% in the 20°C chamber and below 10% in the 60°C chamber.

Figure 3-2 Confined creep test setup using the miniaturized creep frame placed inside an environmental chamber maintaining constant temperature and humidity.

3.3. Computation of Viscoelastic Material Properties

The confined creep apparatus was first utilized by Ma and Ravi-Chandar and subsequently by Park and Roy (Ma and Ravi-Chandar, 2000; Park and Roy, 2004) to obtain the bulk and shear linear viscoelastic compliance functions simultaneously on the same specimen, under constant environmental conditions. Grasley and Lange (Grasley and Lange, 2007) were the first to use such an experimental setup on cementitious materials when they studied cement paste creep at room temperature. In this study, the confining steel cylinder

with an inner radius a of 25 mm (1 in.), an outer radius b of 27 mm (1.06 in.) and a height h of 100 mm (4 in.) was used. The material properties of the confining steel cylinder are known. The Young's modulus of stainless steel (E^c) is 193 GPa and Poisson's ratio (ν^c) is 0.29. The confined test set-up in the cylindrical polar coordinate system is shown in Figure 3-3.

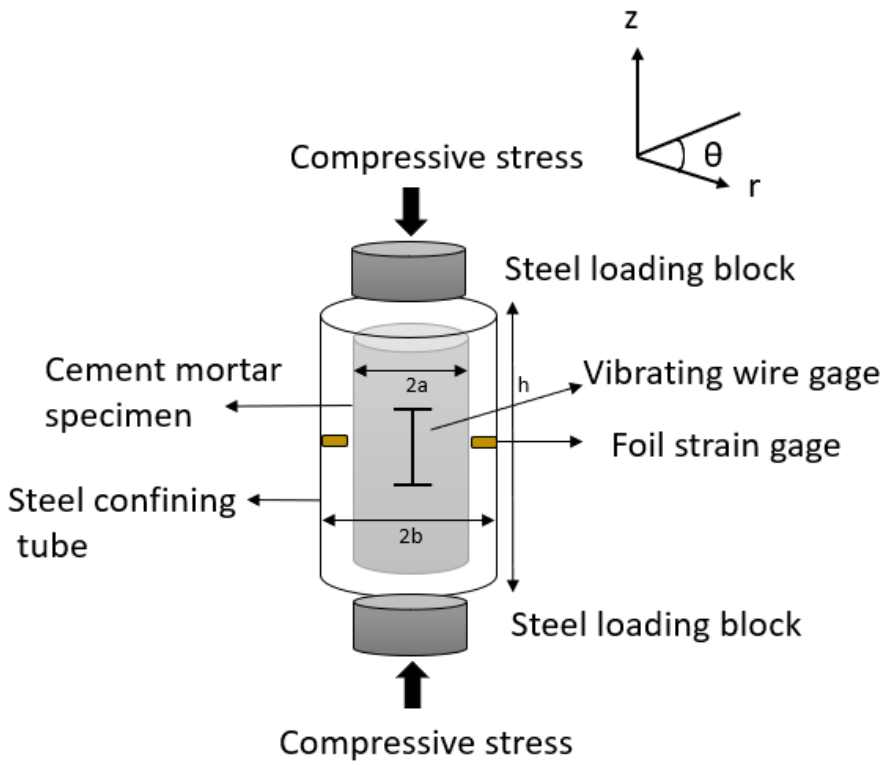

Figure 3-3 Confined compressive creep test set-up with inner radius a of 25 mm (1 in.), an outer radius b of 27 mm (1.06 in.) and a height h of 100 mm (4 in.).

The axial stress, σ_{zz}, experienced by the cement mortar sample under a constant load was calculated by dividing the load applied by the cross-sectional area of the sample such that

$$\sigma_{zz} = \frac{\text{Load applied}}{\pi a^2}. \quad (18)$$

The total axial strain as a function of time, $\varepsilon_a(t)$, was recorded using a vibrating wire gage. The mechanical axial strain, $\varepsilon_{zz}(t)$, was calculated as

$$\varepsilon_{zz}(t) = \varepsilon_a(t) - \varepsilon^{sh}(t), \quad (19)$$

where $\varepsilon^{sh}(t)$ is the free shrinkage strain. Since the specimens were sealed by the confining cylinder and the water to cement ratio was high enough to not contribute any significant autogenous shrinkage, free shrinkage strain was assumed to be negligible and ignored in the study. Figure 3-4 shows the free strain measured in a sample confined by a stainless steel tube to be far lower than that of a similar sample wrapped with a layer of adhesive backed aluminum foil.

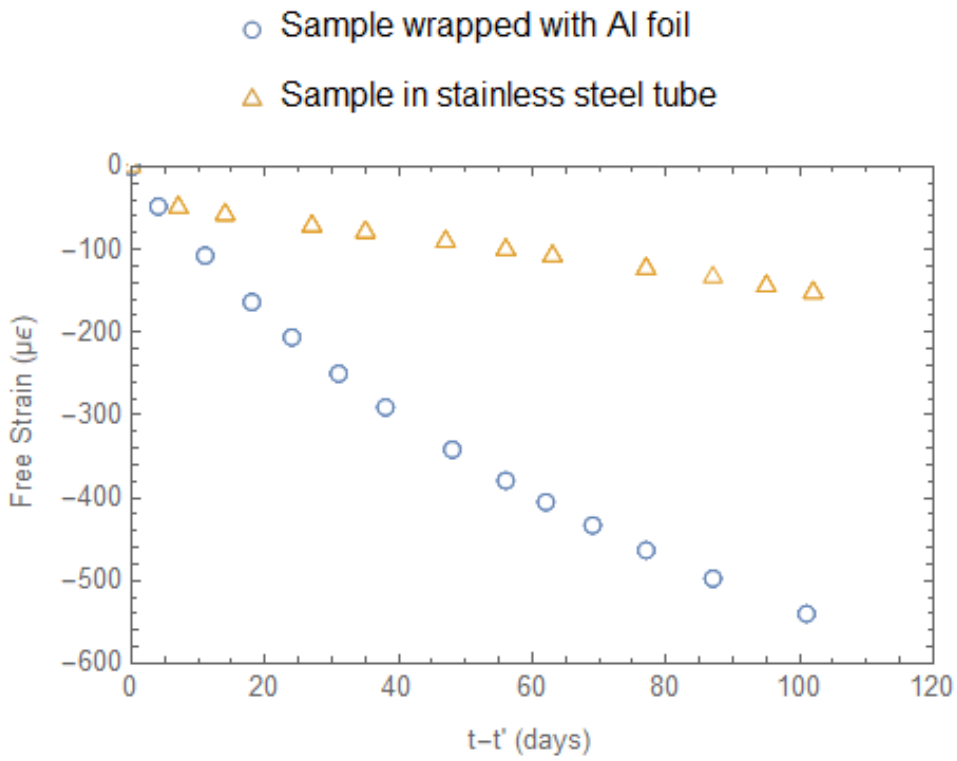

Figure 3-4 Free strain comparison of a sample in a stainless steel tube to sample wrapped with Al foil at 20°C. Here t refers to the present age and t' refers to the age when confined creep test started (i.e., 28 days).

When an axial stress is applied, the specimen tends to expand in the transverse direction due to Poisson's effect, resulting in a positive (or tensile) radial displacement (u_r). However, the confining cylinder restrains this deformation with a negative (or compressive) radial stress (σ_{rr}).

From the continuity conditions at the interface

$$\sigma_{rr}(a)=\sigma_{rr}^{c}(a) \tag{20}$$

and

$$u_r(a)=u_{rr}^{c}(a), \tag{21}$$

where superscript *c* denotes confining cylinder.

By measuring the hoop strain, (ε_h), on the outer surface of the confining cylinder using the foil strain gages, the radial displacement and radial stress of the confining cylinder on the inner surface, u_r^c and σ_{rr}^c, respectively, were computed by the Lamé solution as

$$u_r^c = \frac{\varepsilon_h}{2}\left[\left(1-\nu^c\right)a + \left(1-\nu^c\right)\frac{b^2}{a}\right]$$

and (22)

$$\sigma_{rr}^c(t) = -\frac{b^2-a^2}{2a^2}E^c\varepsilon_h(t). \quad (23)$$

The stress induced radial strain, $\varepsilon_{rr}(t)$, was calculated by dividing the radial displacement, u_r^c, by inner radius, a, and subtracting the free shrinkage strain such that

$$\varepsilon_{rr}(t) = \frac{\varepsilon_h(t)}{2}\left[\left(1-\nu^c\right) + \left(1-\nu^c\right)\frac{b^2}{a^2}\right] - \varepsilon^{sh}(t). \quad (24)$$

The axisymmetric strain-displacement relation gives $\varepsilon_{rr} = \varepsilon_{\theta\theta}$ and equilibrium equations require that radial and hoop components of stress are equal, i.e., $\sigma_{rr} = \sigma_{\theta\theta}$, where r and θ represent radial and tangential components, respectively. Since eqns. (18), (19), (23) and (24) representing the axial stress, axial strain, radial stress and radial strain, respectively, form the principal components of stress and strain, the full 3D constitutive response of the material was obtained from the confined experiment.

The deformation of the specimen was then separated into dilatational and deviatoric components. The volumetric stress, σ_m, in the specimen was determined as one-third the sum of the three normal stress components such that

$$\sigma_m(t) = \frac{\sigma_{kk}(t)}{3} = \frac{1}{3}\left[\sigma_{zz}(t) + \sigma_{rr}(t) + \sigma_{\theta\theta}(t)\right]$$

$$= \frac{1}{3}\left[\sigma_{zz}(t) + 2\sigma_{rr}(t)\right]. \quad (25)$$

Since the deformation gradients are small, the volumetric strain, ε_{kk}, was approximated as the sum of three normal strains such that

$$\varepsilon_{kk}(t) = \left[\varepsilon_{zz}(t) + \varepsilon_{rr}(t) + \varepsilon_{\theta\theta}(t)\right]$$

$$= \left[\varepsilon_{zz}(t) + 2\varepsilon_{rr}(t)\right]. \quad (26)$$

The deviatoric stress, τ_e, and deviatoric strain, γ_e, from the confined compression test were computed using

$$\tau_e(t) = \frac{1}{\sqrt{3}}\left|\sigma_{zz}(t) - \sigma_{rr}(t)\right| \text{ and} \quad (27)$$

$$\gamma_e(t) = \frac{2}{\sqrt{3}}\left|\varepsilon_{zz}(t) - \varepsilon_{rr}(t)\right|. \quad (28)$$

The constitutive equations for a non-aging, linear viscoelastic material, expressed in terms of dilatational and deviatoric components, is given by

$$\varepsilon_{kk}(t) = \int_0^t B(t-t')\frac{\partial \sigma_m(t')}{\partial t'}dt' \quad (29)$$

and

$$\gamma_e(t) = \int_0^t L(t-t')\frac{\partial \tau_e(t')}{\partial t'}dt', \quad (30)$$

where $B(t)$ and $L(t)$ are the bulk and shear compliances of the material, respectively. Here t refers to the present time and t' is the dummy integration time variable. Once the bulk and shear compliances were found, the uniaxial creep compliance, $J(t)$, was computed using intermoduli conversion via the correspondence principle such that

$$\bar{E}(s) = \frac{9\bar{K}(s)\bar{G}(s)}{3\bar{K}(s) + \bar{G}(s)}$$

and (31)

$$\bar{J}(s).\bar{E}(s) = \frac{1}{s^2}, \quad (32)$$

where $\bar{E}(s)$, $\bar{K}(s)$ and $\bar{G}(s)$ are Laplace transformed relaxation, bulk and shear modulus functions, respectively, and s is the complex variable in the Laplace domain. The Laplace transformed uniaxial creep compliance and the corresponding Laplace transformed relaxation moduli are each related as shown in eqn. (32).

3.4. Results and Discussion

3.4.1. Initial Loading

The confined creep test was performed on one specimen each at 20ºC and 60ºC. The stress/strength ratio applied was 0.25, which lies within the linearity range of the material according to the study by Neville and Dilger, who demonstrate that non-linearity of cement mortar arises only beyond a stress/strength ratio of 0.80 (Neville and Dilger, 1970). Figure 3-5 shows that when the compressive axial load was applied on the sample, the compressive axial strain was accompanied by an increase in tensile hoop strain.

As outlined earlier, using the measured hoop strain and material properties of the confining cylinder, the principal components of stress and strain were determined. Figure 3-6 shows the volumetric (or bulk) and shear stresses plotted against their corresponding volumetric (or bulk) and shear strains at 20ºC and 60ºC.

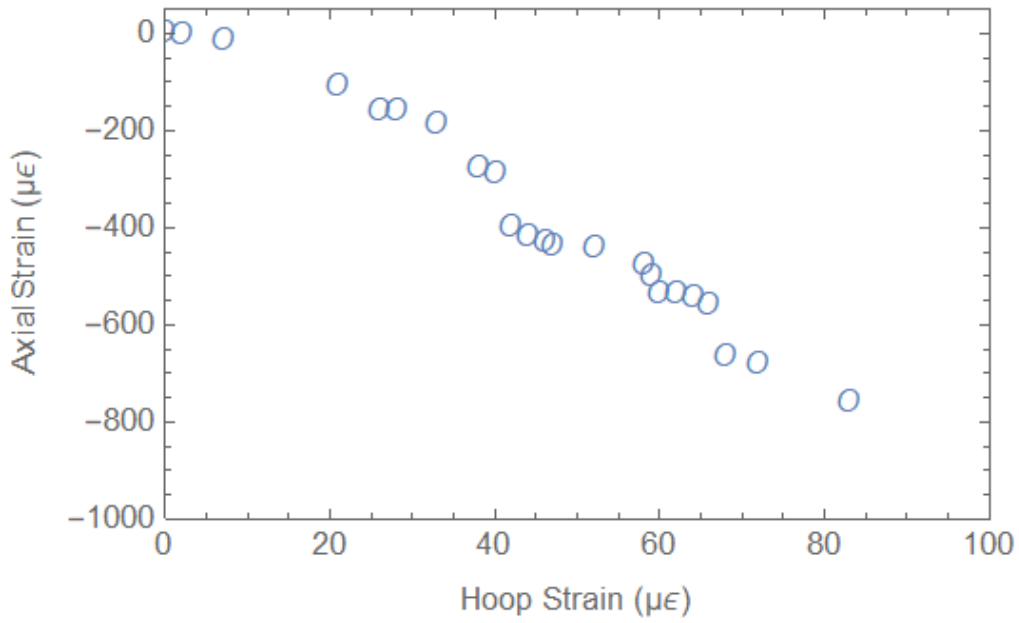

Figure 3-5 Variation of axial strain and hoop strain at initial loading. Data from specimen at 20ºC.

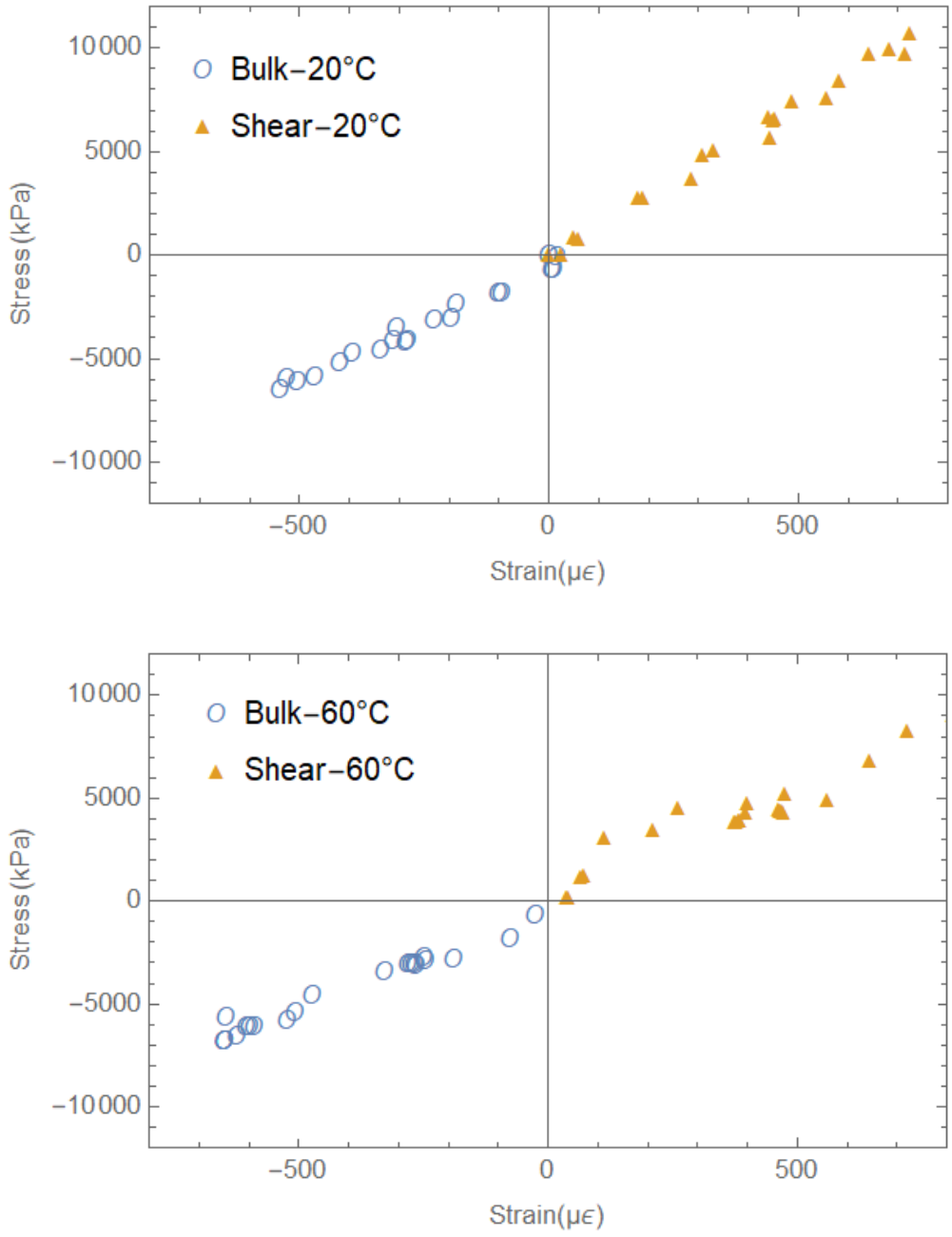

Figure 3-6 Volumetric (or bulk) and shear stress-strain data at initial loading at 20ºC and 60ºC.

It is clear from Figure 3-6 that the samples exhibited linear elastic behavior at the time of initial loading. The slope of these curves represents the elastic bulk and shear

modulus of cement mortar at the respective temperatures. The elastic bulk modulus, *K*, was calculated to be 13.6 GPa and the elastic shear modulus, *G*, was calculated to be 11.6 GPa at 20ºC. Using the intermodulus conversion, the elastic Young's modulus, *E*, was calculated to be 27.0 GPa. To validate the calculations, the *E* of three mortar cylinders (100 mm x 200 mm) were measured in accordance with ASTM C469. The average measured Young's modulus of the samples at 28 days was 25.4 ± 1.1 GPa. The predicted and measured elastic modulus values were hence found to be in reasonable agreement. Similarly, at 60ºC from Figure 3-6, *K* was calculated to be 11.0 GPa and *G* was calculated to be 9.4 GPa resulting in *E* of 21.8 GPa using intermodulus conversion. It is unclear why the Young's modulus was lower at 60ºC than at 20ºC, though other researchers have measured reductions in stiffness of concrete (Shoukry et al., 2011) and cement paste (Odelson et al., 2007) at elevated temperatures around 50ºC.

3.4.2. Analysis of Methods for Determining $B(t)$ and $L(t)$ from Confined Creep Test

The deformation from the confined experiment was separated into dilatational and deviatoric parts for the determination of dilatational and deviatoric compliance functions. Although the axial load was maintained relatively constant throughout the experiment, the volumetric and shear stress varied as a function of time and temperature as shown in Figure 3-7.

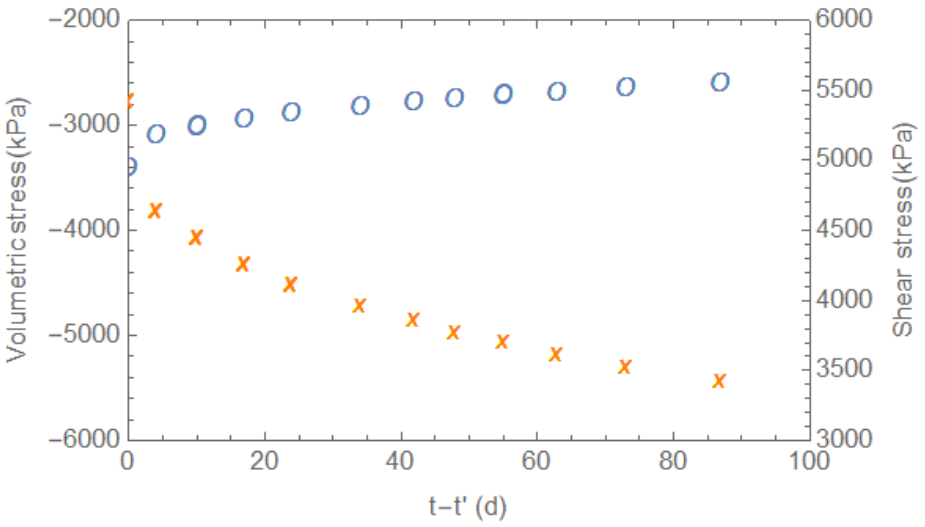

(a) 20ºC

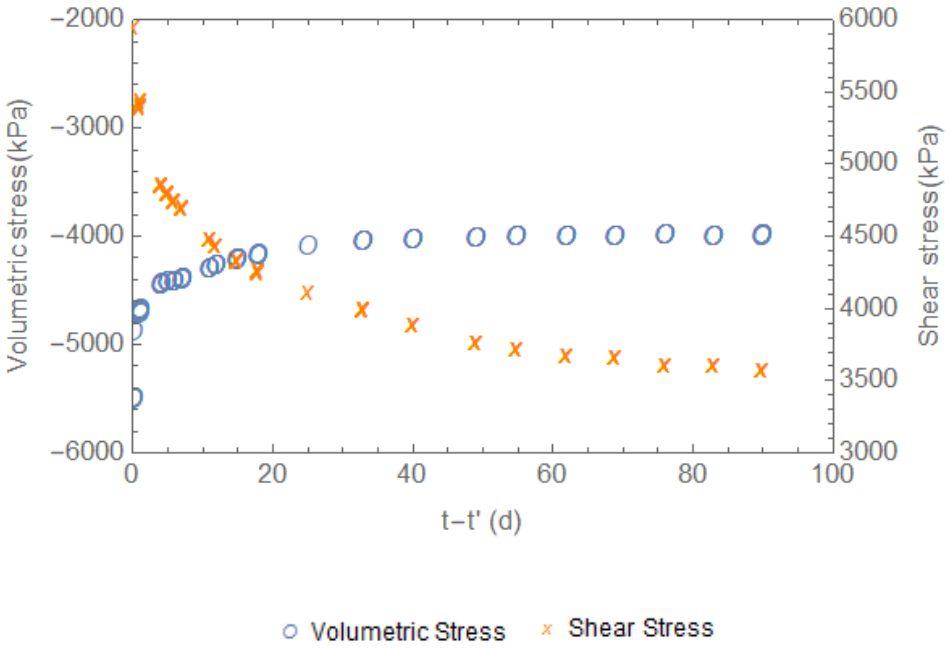

(b) 60ºC

Figure 3-7 The volumetric and shear stress as a function of time during the confined creep experiment at 20ºC and 60ºC. Here t refers to the present age and t' refers to the age when confined creep test started (i.e., 28 days).

It is clear from Figure 3-7. that shear stress showed significant decay with time compared to the volumetric stress at both temperatures. There was a 37% decay in shear stress compared to 24% decay in volumetric stress after 90 days of testing at room temperature. On the other hand, at 60ºC, there was a 49% decay in shear stress compared to 28% decay in volumetric stress after 90 days.

Since volumetric and shear strains are evolving along with the corresponding stresses during the experiment, a more informative way to assess the confined creep test results is to determine the bulk and shear compliance functions, since these functions are ostensibly independent of either stress or strain history. To understand the significance of stress decay in the confined test, the compliance function was estimated using three methods. The first method (simple division method) is an approximate method whereby load history effects are neglected, and strains are simply divided by their respective stress values such that

$$B(t) \approx \frac{\varepsilon_{kk}(t)}{\sigma_m(t)} \quad \text{and} \quad L(t) \approx \frac{\gamma_e(t)}{\tau_e(t)}. \tag{33}$$

The second method (constant stress method) completely neglects the time variance in the stresses and considers the stress to be constant and equal to the initially applied stresses such that

$$B(t) \approx \frac{\varepsilon_{kk}(t)}{\sigma_{m0}} \quad \text{and} \quad L(t) \approx \frac{\gamma_e(t)}{\tau_{e0}}. \tag{34}$$

The third method (“fitted”) employs the constitutive equations for a linear viscoelastic material to derive the compliance functions accounting for the time-dependency of the stresses and the history dependence of the strains. In order to determine

$B(t)$ and $L(t)$ using the constitutive expression given in eqns. (12) and (13), it is necessary to fit the measured stress history to a time dependent function, take the derivative of that function (in terms of the dummy time variable), multiply the derivative by a presumed function for $B(t)$ and $L(t)$ – including phenomenological fit coefficients – and then integrate the product over time. The resulting time dependent function was fit to the measured strain data to determine the phenomenological fit coefficients included in $B(t)$ and $L(t)$. This is the most fundamentally accurate of the three methods to determine the compliance functions. The other methods may be used for estimating compliance but do not yield precise calculations.

Figure 3-8 shows the graph of the compliance function obtained using these three methods. The $B(t)$ and $L(t)$ clearly increased at higher temperature due to larger creep strains. There was insignificant variation in the $B(t)$ and $L(t)$ calculated using the three methods at 20ºC, implying that either of the two approximate methods may be used to simplify the calculations when the experiments are performed at room temperature. At higher temperatures, however, the magnitude of creep in the samples caused force relaxation in the loading frame leading to greater time dependency of the stresses. Assuming the stress to be constant in such cases while calculating $B(t)$ and $L(t)$ can lead to significant errors. There was a 30% and 48% error while using the constant stress method to estimate $B(t)$ and $L(t)$, respectively, at 60ºC after 90 days of loading.

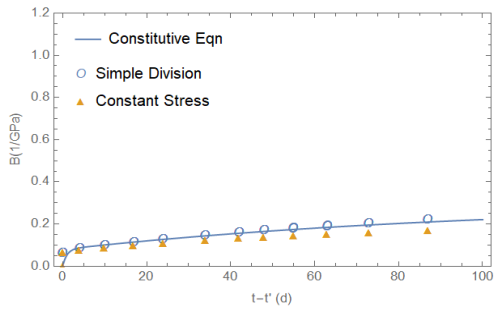

(a) Bulk compliance - 20ºC

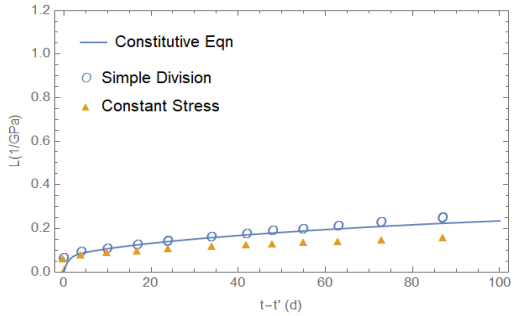

(b) Shear compliance - 20ºC

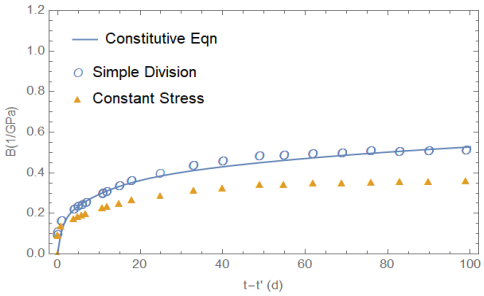

(a) Bulk compliance - 60ºC

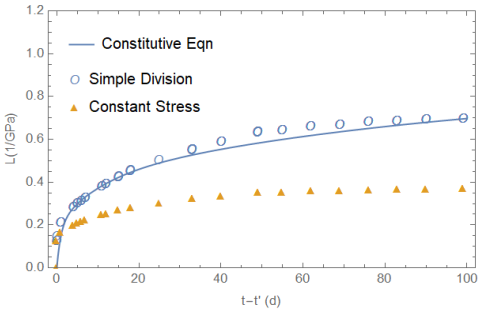

(b) Shear compliance - 60ºC

Figure 3-8 The bulk and shear compliance functions calculated using the three methods, (i) simple division, (ii) assuming load to be constant, (iii), fitting the compliance in the constitutive equation (most accurate).

Once the $B(t)$ and $L(t)$ were computed, they were transformed in to the Laplace domain to find the Laplace transformed bulk modulus, $\overline{K}(s)$ and shear modulus, $\overline{G}(s)$ from the relations

$$\overline{B}(s).\overline{K}(s)=\frac{1}{s^2} \quad \text{and} \quad \overline{L}(s).\overline{G}(s)=\frac{1}{s^2}. \tag{35}$$

The Laplace transformed relaxation modulus, $\overline{E}(s)$, and subsequently the Laplace transformed uniaxial creep compliance, $\overline{J}(s)$, were found using the intermodulus conversion expression shown in eqns. (31)-(32). The inverse Laplace transform was then

used to determine the compliance in the time domain. A graph depicting the predicted compliance through the intermodulus conversion compared to the measured compliance from uniaxial creep data at both temperatures are shown in Figure 3-9. It can be seen that the predicted compliance was reasonably close to the measured compliance data at 20ºC, whereas at higher temperature, the converted uniaxial compliance was significantly higher than the directly measured uniaxial compliance. A possible explanation is that the viscoelastic response is nonlinearly dependent on strain energy magnitude; this would be in keeping with the findings of Li et al., who simulated relaxation of cement pastes due to dissolution of hydration products (Li et al., 2018). In that work, dissolution was modeled as a function of local strain energy magnitude, which implies that application of confining stress can serve to enhance the axial relaxation rate. Experimental studies have verified that dissolution of minerals is accelerated under high local stress (Thomson, 1862; Morel, 2000; Croize et al., 2010; Moradian et al., 2018).

confined experiment.

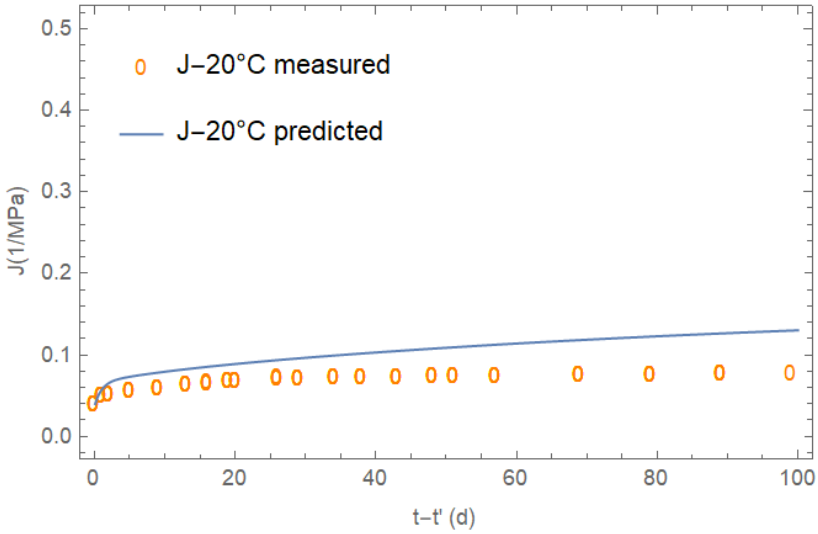

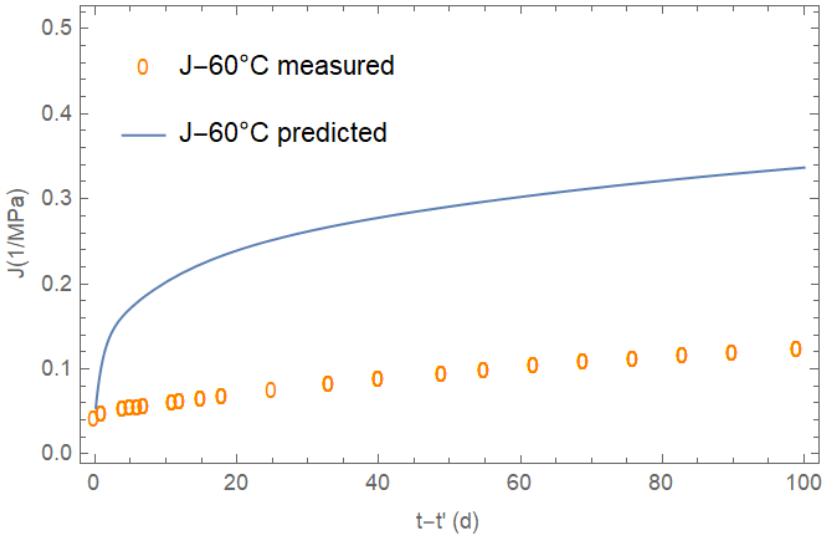

Figure 3-9 The predicted uniaxial creep compliance using intermodulus conversion.

The strain energy is the energy stored in the body undergoing deformation. To eliminate the effects of size, the strain energy is divided by the volume and commonly expressed as strain energy density. For uniaxial and confined tests, the strain energy is calculated as one-half times the dot product of stress and strain tensor.

For uniaxial test,

$$SE_{uniaxial} = \frac{1}{2}\begin{pmatrix} \sigma_{11}\sigma_{12}\ \sigma_{13} \\ \sigma_{21}\sigma_{22}\ \sigma_{23} \\ \sigma_{31}\sigma_{32}\ \sigma_{33} \end{pmatrix} . \begin{pmatrix} \varepsilon_{11}\varepsilon_{12}\ \varepsilon_{13} \\ \varepsilon_{21}\varepsilon_{22}\ \varepsilon_{23} \\ \varepsilon_{31}\varepsilon_{32}\ \varepsilon_{33} \end{pmatrix}$$

For confined test,

$$SE_{confined} = \frac{1}{2}\begin{pmatrix} \sigma_{rr}\sigma_{r\theta}\ \sigma_{rz} \\ \sigma_{\theta r}\sigma_{\theta\theta}\ \sigma_{\theta z} \\ \sigma_{zr}\sigma_{z\theta}\ \sigma_{zz} \end{pmatrix} . \begin{pmatrix} \varepsilon_{rr}\varepsilon_{r\theta}\ \varepsilon_{rz} \\ \varepsilon_{\theta r}\varepsilon_{\theta\theta}\ \varepsilon_{\theta z} \\ \varepsilon_{zr}\varepsilon_{z\theta}\ \varepsilon_{zz} \end{pmatrix}$$

For the tests evaluated in Figure 3-9 conducted at 20°C, the strain energies were calculated to be 0.454 kPa and 1.381 kPa for the uniaxial and confined experiments, respectively. The strain energies for the tests evaluated at 60°C were 0.625 kPa and 6.764 kPa for the uniaxial and confined experiments, respectively. Thus, the ratio of strain energies from confined to uniaxial tests conducted at 60°C were much larger than at 20°C, which supports the hypothesis that the significantly higher calculated versus measured uniaxial compliance at 60°C is due to nonlinear effects introduced by the significantly higher strain energy in the

3.5. Viscoelastic Poisson's ratio

As alluded to previously, there is contradiction in the literature regarding the measurement and prediction of VPR of concrete with time. This uncertainty arises mainly from the way researchers define the VPR function.

As shown by Kassem et al. (2013), in a displacement controlled experiment such as a stress relaxation test where the input axial strain, ε_{11}, is a step function represented as $\varepsilon_{11}(t) = \varepsilon_0 H(t)$, where ε_0 is a constant and $H(t)$ is the Heaviside function, the output transverse strain $\varepsilon_{22}(t)$ is given by

$$\boldsymbol{\varepsilon}_{22}(t) = -\nu(t)\varepsilon_0 . \tag{36}$$

VPR can then be calculated as

$$\nu(t) = -\frac{\boldsymbol{\varepsilon}_{22}(t)}{\boldsymbol{\varepsilon}_0} . \tag{37}$$

On the other hand, in a load controlled experiment, such as a creep test where the input axial stress σ_{11} is a step function represented as $\sigma_{11}(t) = \sigma_o H(t)$, where σ_0 is a constant, the output axial strain is given by

$$\varepsilon_{11}(t) = \int_0^t D(t-t') \frac{\partial \sigma_{11}(t')}{\partial t'} dt' \tag{38}$$

The corresponding output transverse strain is given by

$$\varepsilon_{22}(t) = -\int_0^t \nu(t-t') \frac{\partial \varepsilon_{11}(t')}{\partial t'} dt' . \tag{39}$$

In order to determine $\nu(t)$ using eqn. (39), it is necessary to fit the measured axial strain history to a time dependent function, take the derivative of that function (in terms of the dummy time variable), multiply the derivative by a presumed function for $\nu(t)$ – including phenomenological fit coefficients – and then integrate the product over time. The resulting time dependent function is then fit to the measured transverse strain data to determine the phenomenological fit coefficients included in $\nu(t)$. Many researchers have determined a "creep Poisson's ratio" for concrete by neglecting the history dependence denoted by the convolution integral in eqn. (39); such a creep Poisson's ratio is a function of the stress or strain history of the material and is thus not a constitutive property like the VPR determined in eqn. (37) or (39).

In case of a specimen subjected to a 3D state of stress, such as a confined creep test, the VPR may be determined using the intermoduli conversion in the Laplace domain according to

$$s.\bar{\nu}(s) = \frac{3\bar{K}(s) - 2\bar{G}(s)}{6\bar{K}(s) + 2\bar{G}(s)} . \tag{40}$$

In this study, using the Laplace transformed bulk and shear modulus, the Laplace transformed VPR was determined from eqn. (40). Then, the Laplace transformed VPR was inverted to the time domain to obtain the VPR of the viscoelastic material (see Figure 3-10). *Mathematica* was used to perform the analyses.

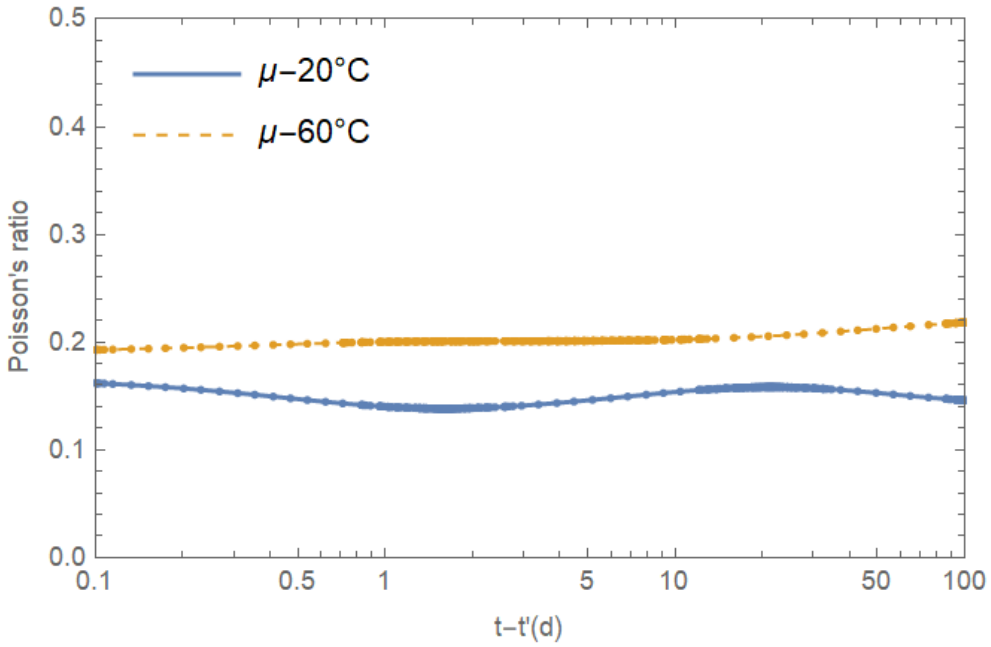

Figure 3-10 Variation of viscoelastic Poisson's ratio of cement mortar as a function of time.

The viscoelastic Poisson's ratio of cement mortar was found to be a relatively constant value of 0.14 at 20ºC and there was a slight increase from 0.17 to 0.19 over a period of 100 days after initial loading at 60ºC. It is interesting to note that the elastic Poisson's ratio is slightly higher at elevated temperatures since the shear modulus decreased more significantly than the bulk modulus when the temperature was increased to 60ºC compared to 20ºC.

If both the dilatational and deviatoric compliance functions show a similar trend (i.e., same rate at all times), then VPR can be considered a constant function with time. From , Figure 3-10 it can be seen that the VPR is largely not time-dependent at 20ºC but at 60ºC, where the rate of increase of deviatoric compliance was higher than the rate of increase of dilatational compliance, VPR was found to increase slightly as a function of time. The same phenomenon is discussed by Bernard et al. and Grasley and Lange, where the reduction in porosity in the sample was suggested to decrease the rate of change of dilatational compliance with time versus the rate of change of deviatoric compliance (Bernard, 2003; Grasley, 2007). If strain energy magnitude strongly affects creep or relaxation rates in concrete as hypothesized in the previous section, it is important to note that – since the VPR is still relatively constant at 60ºC, where the strain energy was significant – the effect of strain energy magnitude on both deviatoric and dilatational relaxation or creep rates is almost the same. The implication is that, while relaxation rates might depend on strain energy magnitude, the VPR can be approximated as largely independent of strain energy magnitude, at least for the magnitudes considered in this study.

3.6. Conclusions

The study describes a simple and cost-effective experiment to conduct a confined creep test on cement mortar using a miniaturized creep frame. This creep test was used to quantify the 3D creep response through direct determination of the full stress and infinitesimal strain tensors. Consequently, the viscoelastic compliance functions and Poisson's ratio of cement mortars were investigated at two different temperatures. The

deformation from the confined experiment was separated into dilatational and deviatoric parts for the determination of dilatational and deviatoric compliance functions. It was observed that the dilatational and deviatoric compliance functions showed a similar trend at 20ºC whereas, at 60ºC, the rate of change of deviatoric compliance was slightly higher compared to dilatational compliance. Using the intermodulus conversion, the viscoelastic Poisson's ratio of cement mortar was found to be a nearly constant value of 0.14 at 20ºC and increased from 0.17 to 0.19 over a period of 100 days after initial loading at 60ºC.

Another critical finding was that the uniaxial compliance calculated from the bulk and shear relaxation moduli was higher than measured directly, with the magnitude of the difference seeming to depend on the magnitude of the strain energy present in the test. Though more testing is recommended, it is hypothesized that the higher strain energy increases the rate of dissolution of hydration products and thus the creep resulting from the requisite stress redistribution. The practical implication of the dependence of the compliance function on strain energy is that the application of moderate lateral stresses can induce non-linearity of the viscoelastic constitutive behavior; this means that one might not be able to utilize creep compliances determined experimentally in a uniaxial test to predict the response in structures with 2D or 3D states of stress. Interestingly, the results in this work indicate that – since the viscoelastic Poisson's ratio remains relatively constant (slightly increasing) as determined from the confined test at 60ºC – the high strain energy affects the dilatational and deviatoric compliances by roughly the same magnitude, indicating they are similarly impacted by enhanced dissolution rates.

References

1. Aili, A., Vandamme, M., Torrenti, J.M. and Masson, B.: Theoretical and practical differences between creep and relaxation Poisson's ratios in linear viscoelasticity. Mech. Time-Depend. Mater. **19** (4), 537-555 (2015).
2. Aili, A., Vandamme, M., Torrenti, J.M. and Masson, B and Sanahuja, J.: Time evolutions of non-aging viscoelastic Poisson's ratio of concrete and implications for creep of CSH. Cem. Conc. Res. **90**, 144-161(2016).
3. Atheel, E., Allos, L.H. and Martin.: Factors affecting Poisson's ratio for concrete. Bldg. Env. **16** (1), 1-9 (1981).
4. Bažant, Z. P.: Theory of Creep and Shrinkage in Concrete Structures: A Precis of Recent Developments. Reprinted from Mech. Today, **2** (1), 1-93 (1975).
5. Bažant, Z P.: Normal and Refractory Concretes for LMFBR Applications-Vol. 1, Review of Literature on High-Temperature Behavior of Portland Cement and Refractory Concretes, EPRI Report NP-2437, Northwestern University and Portland Cement Association, Chicago, Illinois, June (1982).
6. Bažant, Z. P., Cusatis, G. and Cedolin, L.: Temperature Effect on Concrete Creep Modeled by Microprestress-Solidification Theory. J. Eng. Mech. **130** (6), 691-699 (2004).
7. Bernard, O., Ulm, F.-J. and Germaine, J.T.: Volume and deviator creep of calcium-leached cement-based materials. Cem. Concr. Res. **33** (8), 1127–1136 (2003).
8. Charpin, L., Pape, Y. L., Coustabeau, E., Masson, B. and Montalvo, J.: EDF Study of 10-years concrete creep under unidirectional and biaxial loading: Evolution of

poisson coefficient under sealed and unsealed conditions. Concreep 10, Vienna, Austria (2015).

9. Charpin, L. and Sanahuja, J.: Creep and relaxation poisson's ratio: Back to the foundations of linear viscoelasticity. Application to concrete. Int. J. Sol. Struct. 110-111, 2-14 (2017).
10. Cruz, C. R.: Elastic properties of concrete at high temperatures. J. PCA R&D Lab. **8**, 37–45 (1966).
11. EDF: Vercors an experimental mock-up of a reactor containment building. http://researchers.edf.com/research-activities/generation/vercors-an-experimental-mock-up-of-a-reactor-containment-building-290900.htm (2014).
12. Ehm, C.: Experimental Investigations of the Biaxial Strength and Deformation of Concrete at High Temperatures. Dissertation, Technical University of Braunschweig, Germany. (1985).
13. Gopalakrishnan, K., Neville, A. and Ghali, A.: Creep Poisson's ratio of concrete under multiaxial compression. J. Proc., **66**, 1008-1019 (1969).
14. Grasley, Z. and Lange, D.: The viscoelastic response of cement paste to three-dimensional loading. Mech. Time-Depend. Mater. **11**, 27-46 (2007).
15. Hilton, H.H.: Implications and Constraints of Time-Independent Poisson Ratios in Linear Isotropic and Anisotropic Viscoelasticity. J. Elast. **63,** 221–251 (2001).
16. Jordaan, I. J.: Analysis of creep in concrete structures under general states of stress. Seminar on concrete structures subjected to triaxial stresses. Italy, 111-118 (1974).

17. Jordaan, I. and Illston, J.: The creep of sealed concrete under multiaxial compressive stresses. Mag. Concr. Res. **21** (69), 195–204 (1969).

18. Kassem, E., Grasley, Z. and Masad, E.: Viscoelastic poisson's ratio of asphalt mixtures. Int. J. Geomech. **13** (2), 162-169 (2013).

19. Kesler, C. E.: Creep behavior of Portland cement mortar and concrete under biaxial stress. Univ. of Urbana-Champaign (1977).

20. Kim, J. K., Kwon, S.H., Kim, S. Y. and Kim, Y.Y.: Experimental studies on creep of sealed concrete under multiaxial stresses. Mag. Concr. Res. **57** (10), 623-634 (2005).

21. Lakes, R.S.: The time-dependent Poisson's ratio of viscoelastic materials can increase or decrease. Cell. Polym. **11**, 466–469 (1992).

22. Lakes, R. S. and Wineman, A.: On Poisson's ratio in linearly viscoelastic solids. J. Elast. **85** (1), 45-63 (2006).

23. Ma, Z. and Ravi-Chandar, K.: Confined compression: A stable homogeneous deformation for constitutive characterization. Exp. Mech. **40** (1), 38-45 (2000).

24. Nasser, K. W. and Neville, A. M.: Creep of Concrete at Elevated Temperature. ACI J. Proc., **62** (12), 1567-1579 (1965).

25. Neville, A. M. and Dilger, W.: Creep of Concrete: Plain, Reinforced, Prestressed. North-Holland, Amsterdam (1970).

26. NRC: NUREG/CR–7031- A Compilation of Elevated Temperature Concrete Material Property Data and Information for Use in Assessments of Nuclear Power Plant Reinforced Concrete Structures. Naus, D. J. (2010).

27. Odelson, J. B., Kerr, E. A. and Vichit-Vadakan, W.: Young's modulus of cement paste at elevated temperatures. Cem. Conc. Res. **37** (2), 258-263 (2007).

28. Park, S. J. and Roy, K. M.: Simplified bulk experiments and hygrothermal nonlinear viscoelasticity. Mech. Time-Depend. Mater. **8** (4), 303-344 (2004).

29. Parrott, L.: Lateral strains in hardened cement paste under short-and long-term loading. Mag. Concr. Res. **26** (89), 198–202 (1974).

30. Ross, A. D.: Experiments on the creep of concrete under two-dimensional stressing. Mag. Concr. Res. **6** (16), 3-10 (1954).

31. Shoukry, S. N., William, G. W., Downie, B. and Riad, M. Y.: Effect of moisture and temperature on the mechanical properties of concrete. Construc. Bldg Mater. **25** (2), 688-696 (2011).

32. Tschoegl, N. W., Knauss, W.G. and Emri, I.: Poisson's ratio in linear viscoelasticity – a critical review. Mech. Time-Depend. Mater. **7** (6),198-202 (2002).

33. Vidal, T., Sellier, A., Ladaoui, W., and Bourbon, X.: Effect of temperature on basic creep of High-Performance Concretes heated between 20ºC and 80ºC. J. Mat. Civil Eng. **27** (7) (2015).

4. UNIAXIAL CREEP RESPONSE OF CONCRETE

This chapter's focus is to validate the concrete creep model upscaled from the cement mortar properties using the experimental concrete creep data. For that purpose, this chapter describes the concrete creep set-up, measurement and modeling of creep strains. Since the ultimate goal of project was not only to predict creep but also creep induced cracking in nuclear concrete, split tensile test was conducted on virgin concrete as well as concrete that has undergone creep.

4.1. Introduction

Concrete creep has been a topic of interest for several decades especially due to the increasing use of prestressed concrete as the prime structural material in the construction of pressure vessels in nuclear reactors (Nasser and Neville, 1965). At room temperature, creep can be 3-4 times the initial deformation in the first 1-2 years and at elevated temperatures, the effects of creep cannot be ignored. In 1907, Hatt discovered that concrete under a constant load continued to slowly deform and named the phenomenon as creep (Hatt, 1907). Since then, several researchers have studied the behavior of concrete under uniaxial and multiaxial loading. The time-dependent deformation in concrete originates from the hardened Portland cement paste. The aggregates are typically assumed to be linearly elastic and do not contribute to creep.

Although numerous studies have looked into the creep response of concrete (Ross, 1954; Gopalakrishnan, 1968, McDonald, 1975; Kommendant et al., 1976; Kesler, 1977; Wittmann and Roelfstra, 1980; Bazant, 2001; Benjoudjema et al., 2005; Torrenti and Le Roy, 2015; Sellier et al., 2016) , there is limited literature that describes concrete's long-

term basic creep behavior. Past work on long term creep includes that of Hanson (Hanson, 1953), Troxell (Troxell et al., 1958), Browne (Browne and Blundell, 1969), Brooks (Brooks, 2005) and more recently Charpin (Charpin et al., 2018). Some challenges in conducting long-term creep experiments are reliability of creep frames without failing, stress decay over time and availability of personnel to monitor the test. As detailed in section 2.2, it is well known that concrete creep increases as a function of temperature. This introduces the possibility of predicting long-term creep at room temperature by measuring short-term creep at high temperatures using the TTS principle. Nasser and Neville made interesting observations in their study on concrete creep at elevated temperatures that the shape of creep curve with time is the same at elevated temperature as of normal temperature. Secondly, the linearity of stress-strength ratio is the same as room temperature for elevated temperature upto 96°C which indicates that increase in temperature not only enhances creep, but the mechanisms remain the same (Nasser and Neville, 1965). This validates that the TTS principle can be applied for concrete creep strains.

In the current study, the TTS principle is used to model the temperature dependence of basic creep in mature concrete (where aging effects are less significant). The applicability of TTS on mature, cement-based materials exhibiting basic creep is evaluated and discussed in section 2.3. In this chapter, the experimental creep study on concrete samples at room and elevated temperature (i.e. 60°C) is detailed. Using B3 and B4 model, the drying component of creep was subtracted to obtain only basic creep of concrete. The modelled creep compliance is compared to the simulated results from a

companion study to verify the applicability of upscaling technique from mortar creep compliance to concrete creep compliance. Finally, since creep strain has been speculated to contribute to structural failure (Bažant et al. 2012), split tensile tests were performed on virgin concrete as well as concrete that has undergone creep.

4.2. Experimental Design

4.2.1. Mix Design

The concrete mix design selected for this study closely resembles the Électricité de France (EDF) VeRCoRs concrete mix. The concrete samples were prepared using Type I/II cement. The fine aggregates (River sand) was sieved to pass the 4 mm sieve, intermediate aggregates (River gravel) was sieved to pass between 11 mm and 4 mm and coarse aggregate (Limestone) was sieved to pass between 16 mm and 8 mm. All the aggregates were dried for 24 hours before mixing. The water to cement ratio (w/c) by mass for the mix was 0.52 (SSD condition). This is the same w/c ratio as that of VeRCoRs mortar mix used in the study as detailed in Chapter 2. A water-reducing admixture ‘Pozzolith 80’ was administered at a dosage of 4.22 mL per kilogram of cementitious materials. The mixture proportions used are shown in Table 4-1 and referenced in EDF (EDF, 2014).

Table 4-1 Mixture proportions (SSD condition).

Materials	Unit	Mix
Cement (Type I/II)	kg/m^3	320
	lb/yd^3	539
Fine aggregate 0/4 mm (River sand)	kg/m^3	837
	lb/yd^3	1412
Intermediate aggregate 4/11 mm (River gravel)	kg/m^3	456
	lb/yd^3	768
Coarse aggregate 8/16mm (Limestone)	kg/m^3	560
	lb/yd^3	944
Water	kg/m^3	167
	lb/yd3	282
Pozzolith 80	l/m^3	1.35
	oz/yd^3	66

4.2.2. Sample Preparation

4.2.2.1. Creep Samples

Concrete was mixed in accordance with ASTM C192 and immediately cast into 100 mm x 200 mm (4 in. x 8 in.). DEMEC (Demountable Mechanical Strain gage) contact points for measuring strains on the outer edge of sample were drilled in the concrete mold

before pouring the mix. The cylinders were filled in three equal increments and tapped after each increment to minimize air voids. Once filled, the concrete samples were retained in the mold to prevent moisture loss until just prior to the time of testing after 28 days. The demolded samples were immediately sealed with one layer of adhesive-backed aluminum foil to minimize drying. Two cylinders were connected end to end using sulfur capping compound and concrete plugs of 100 mm (4 in.) height were attached to both ends of the sample to ensure uniform compressive stress throughout the cross-section per the St. Venant's principle.

Compressive creep test was performed on concrete cylinders at 20ºC and 60ºC. The cylinders were loaded to 20% of their compressive strength, which was close to 12,000 lbs. Concrete can be assumed to behave linear viscoelastic upto 40% of its compressive strength (Neville et al., 1983). Strain readings were measured using DEMEC dial gage. Figure 4-1 shows the concrete samples stacked on one another with sulfur capping ends.

4.2.2.2. Free Strain Samples

In addition to the uniaxial concrete creep test, companion cylindrical specimens of same dimensions were fabricated to record the free strain due to shrinkage at each temperature for the entire duration of the creep test. The age and test conditions of these load-free specimens were the same as those used in the creep tests. DEMEC contact points were used to record the free strain with time.

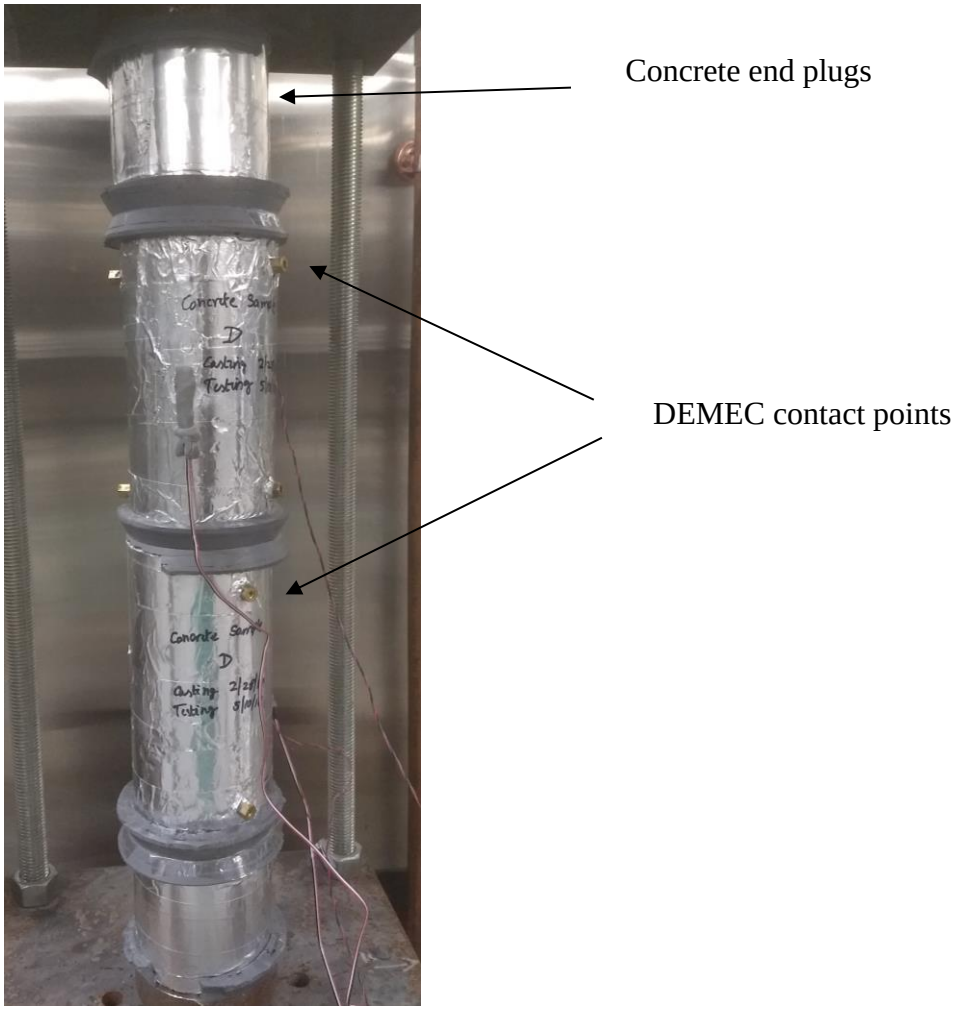

Figure 4-1 Two Concrete sealed cylinders connected end to end with sulfur capping compound.

4.2.3. Uniaxial Creep Test setup

Compressive creep test was performed on concrete cylinders at 20ºC and 60ºC. The concrete samples were loaded at 28 days of age using a hydraulic jack to a constant load of 540 kg (1200 lbs.) which corresponded to 20% of 28-day compressive strength of the concrete. At this loading age and stress magnitude, the mature concrete is approximated as a non-aging, linearly viscoelastic material.

The load was approximated as a stepwise load function given the very short time span of load application relative to the overall duration of the creep test. A load cell was used at the time of jacking the frame which was subsequently removed after the load application. The load was thus assumed to be constant throughout the entire duration of test. This is a reasonable assumption to make as the concrete frames unlike the miniaturized mortar creep frames have tougher springs that maintains the load constant. The creep strains from DEMEC points were recorded once a day for a week, then once a week for a month followed by once a month for a year. As alluded to earlier, creep tests were run at two different temperatures: 20°C (reference temperature) and 60°C. Two replicates of concrete samples were used at each temperature and were heated to the respective test temperature before starting the creep test (to avoid the accumulation of thermal strains during creep). The experiments were conducted in environmental chambers maintaining a constant temperature (Figure 4-2). The relative humidity was consistent at 50% in the 20°C chamber and below 10% in the 60°C chambers.

Figure 4-2 Uniaxial concrete creep test setup.

4.3. Results and Discussion

4.3.1. Concrete Mix Properties

The compressive strength ($f_c^{'}$) and elastic Young's modulus (E) of the concrete were measured at ages of 3, 7, 14, 28 and 90 days in accordance with the test procedures outlined in ASTM C39 and ASTM C469 respectively. The concrete was mixed according to ASTM C192 and immediately cast into 100 mm x 200 mm (4 in. x 8 in.) cylindrical molds. The cylinders were filled in three equal increments and tapped after each increment

to minimize air voids. All samples were kept in the mold until the testing time. Axial deformation was measured using an extensometer with a 100 mm (4 in.) gage length. Three replicates of the mortar samples were tested at each age. The evolution of mean values of $f_c^{'}$ and E of cement mortar with age is shown in **Error! Reference source not found.** along with the standard error for each measurement. As expected the strength and stiffness of concrete increases with age. On comparison to the material property of mortar in Chapter 2, the strength of concrete is lesser than strength of mortar whereas the elastic stiffness of concrete is higher than that of mortar due to the presence of coarse aggregates in concrete.

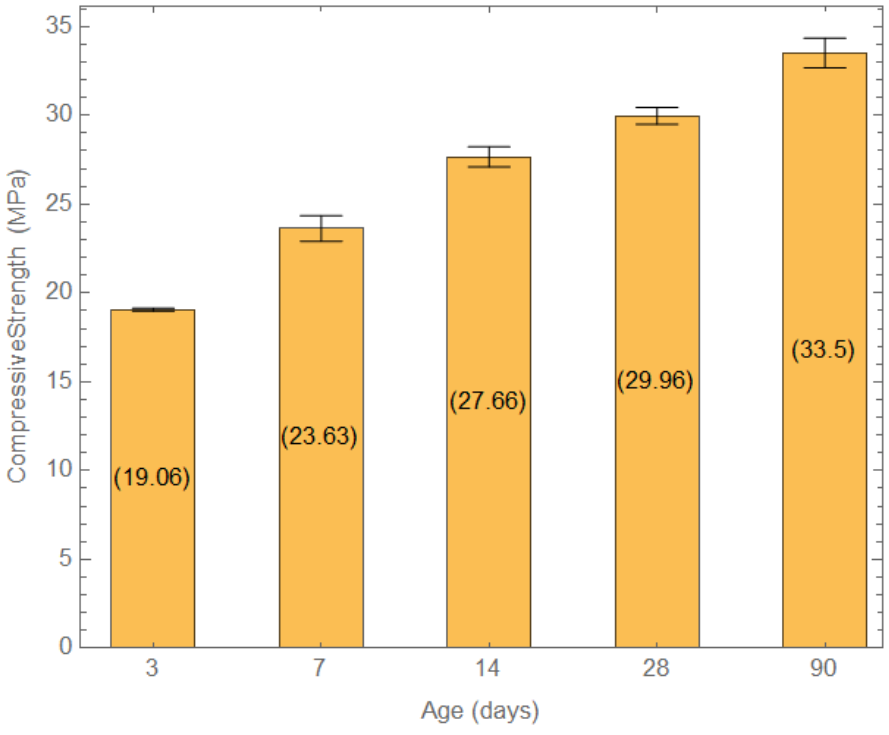

Figure 4-3 Average compressive strength of concrete at different ages along with the standard error for each measurement.

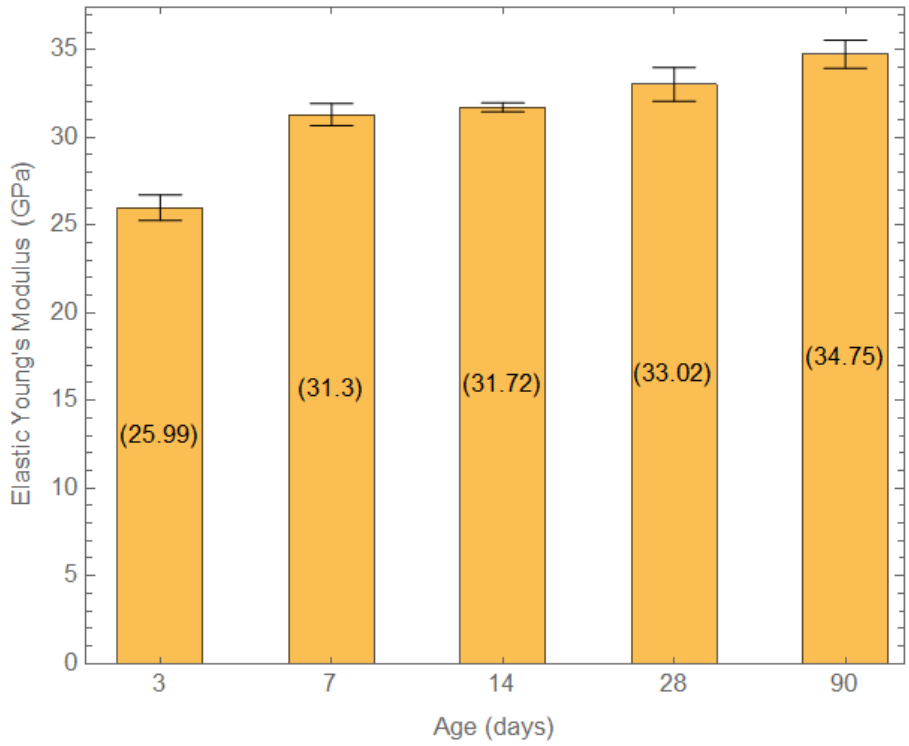

Figure 4-4 Average elastic Young's modulus of concrete at different ages along with the standard error for each measurement.

4.3.2. Free Strain

The free strain (or free shrinkage) data obtained at two different temperatures on the companion specimens are shown in Figure 4-5. Although the samples were sealed using aluminum foil, the author propose that the free shrinkage recorded is a combination of autogenous and drying shrinkage (the foil does not provide a perfect seal). The free strain at 60ºC was higher compared to that at 20ºC, which may be explained by elevated drying at the higher temperature.

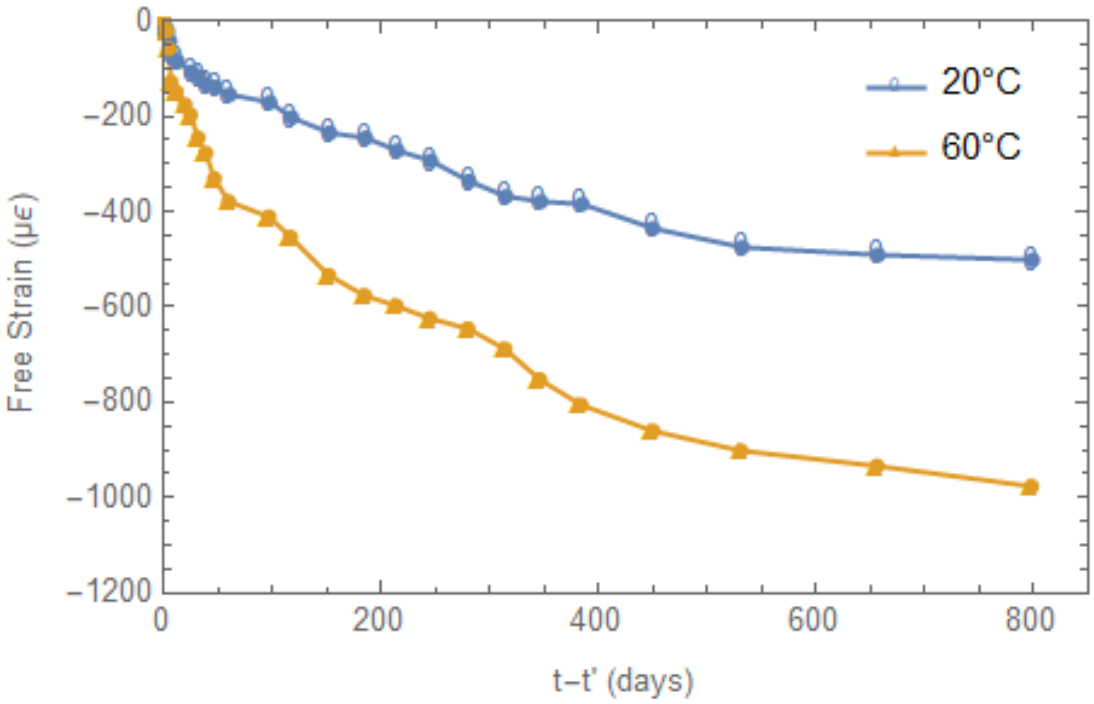

Figure 4-5 Free strain (autogenous+drying shrinkage) data with time at two different temperatures. Here t refers to the present age and t' refers to the age when creep test began.

4.3.3. Uniaxial Creep test

The stress on the concrete samples was calculated as a function of time using the constant load applied and the cross-sectional area of the samples. Figure 4-6 (a) shows a representative fitted stress function of a concrete sample at 20°C.

$$\sigma(t) = 8.722 + 0.0000112e^{-t} + 6.75*10^{-6}e^{\frac{-t}{10}} + 6.04*10^{-6}e^{\frac{-t}{100}} \quad (41)$$

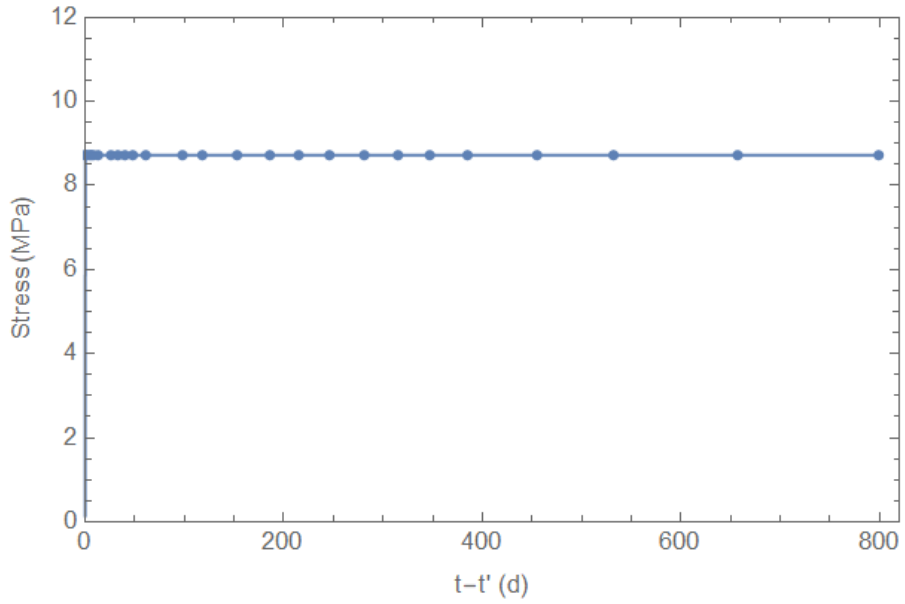

(a)

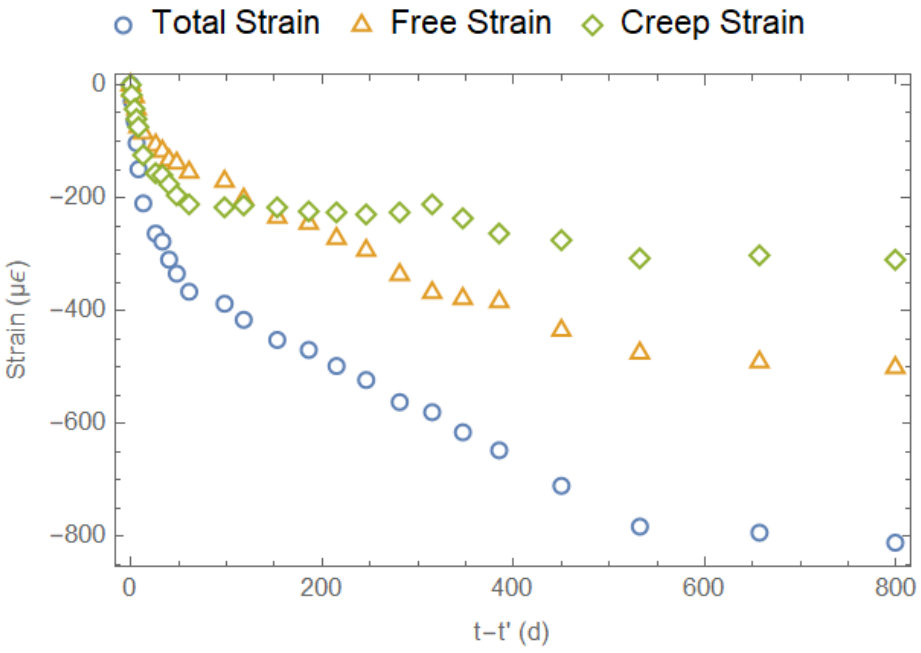

(b)

Figure 4-6 (a) Fitted stress with respect to time under load for a sample at 20°C. (b) Graph showing total strain, free strain and creep strain for a sample under load as a function of time.

Figure 4-6(b) shows the different components of strain in the concrete sample from a creep test. The strain readings represent the average strains recorded for the two replicate specimens. The DEMEC at the exterior of the sample records the total strain. The free strain reading was constantly monitored using DEMEC in an unloaded specimen at the same age and test conditions. Despite the fact that all samples were sealed with an aluminium foil to restrict drying, the free strain measured was mostly from drying shrinkage since autogenous shrinkage is unlikely in a mix design with 0.52 w/c ratio. If drying did occur in the samples during the test as anticipated, the measured creep strain is the sum of basic creep and drying creep in accordance to the Pickett effect. This issue will be addressed later in the study. The creep strain in Figure 4-6(b), which is the primary point of interest in this study, is the difference between the total strain and free strain.

It was observed that after 800 days, the creep strain at 60ºC was 1.6 times higher than that at 20ºC. These multipliers are similar to those recorded in existing literature. Nasser and Neville found that for samples with a stress-strength ratio of 35% loaded at 14 days of age and 15 months under load, the creep at 72ºC was 1.75 times greater than that at 21ºC. (Nasser and Neville 1965). In comparison, McDonald showed that for samples at a stress-strength ratio of 31% loaded at 90 days of age and 12 months under load, the compressive creep of concrete at 66ºC was 1.79 times that observed at 23ºC (McDonald 1975). Using the B4 model, creep at 60ºC was 1.69 times than the corresponding value at 20ºC. The average creep strains obtained at the different test temperatures are plotted in Figure 4-7.

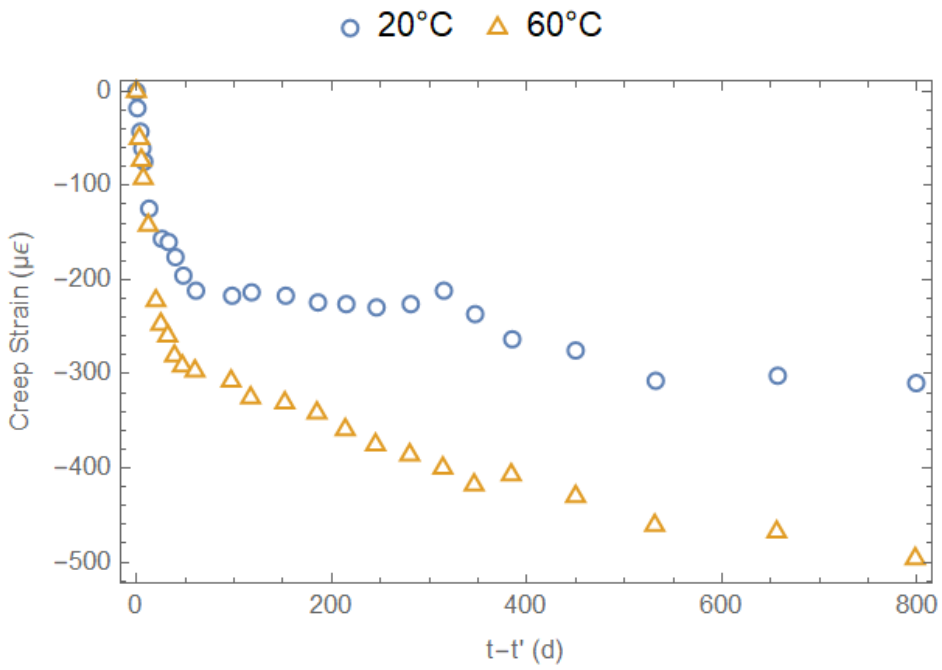

Figure 4-7 Creep strain of concrete at different temperatures.

4.3.3.1. Analysis of methods for determining $J(t)$ from creep results

A more informative way to compare the creep test results at varying temperatures (rather than plotting creep strain) is to assess the creep compliance, $J(t)$. The creep compliance at a constant load is given by dividing the measured creep strain by the applied stress, but the stress-strain relationship is of the integral or differential type for a non-constant stress history. For a non-aging, linearly viscoelastic material, the axial strain ($\varepsilon(t)$) is related to the axial stress $\sigma(t)$ according to

$$\varepsilon(t) = \int_0^t J(t-t') \frac{\partial \sigma(t')}{\partial t'} dt' , \qquad (42)$$

where t is the present time and t' is the dummy time variable. In order to determine $J(t)$ using the constitutive expression given in eq. (4) it is necessary to fit the measured stress

history to a time dependent function, take the derivative of that function (in terms of the dummy time variable), multiply the derivative by a presumed function for $J(t)$ - including phenomenological fit coefficients – and then integrate the product over time. The resulting time dependent function is fit to measured strain data to determine the phenomenological fit coefficients included in $J(t)$. The fitted spring constants and retardation times used in the Kelvin chain are shown in Table 4-2.

Table 4-2 Spring constants and retardation times used in the Kelvin chain at different temperatures.

(a) 20ºC

Specimen 1		Specimen 2	
τ_i	J_i(1/GPa)	τ_i	J_i(1/GPa)
1	0.00343	1	0.00497
10	$1.915*10^{-7}$	10	$5.438*10^{-7}$
100	$2.227*10^{-7}$	100	$1.685*10^{-7}$
1000	0.03343	1000	0.00225

(b) 60ºC

Specimen 1		Specimen 2	
τ_i	J_i(1/GPa)	τ_i	J_i(1/GPa)
1	0.00291	1	0.00743
10	$2.003*10^{-8}$	10	0.00278
100	$5.408*10^{-8}$	100	$1.193*10^{-7}$
1000	0.0573	1000	0.00075

For a relatively constant stress history, eq. (4) may be approximated such that

$$J(t) \approx \frac{\varepsilon(t)}{\sigma_0}. \tag{43}$$

The compliance obtained by simply dividing the strain by the constant stress is called Specific creep compliance. The Specific creep compliance plotted on a log time scale is shown in Figure 4-8 for two different temperatures.

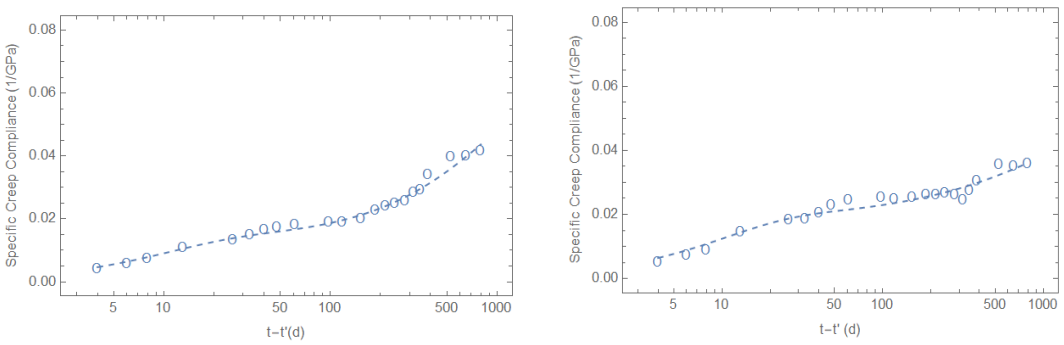

(a) 20ºC

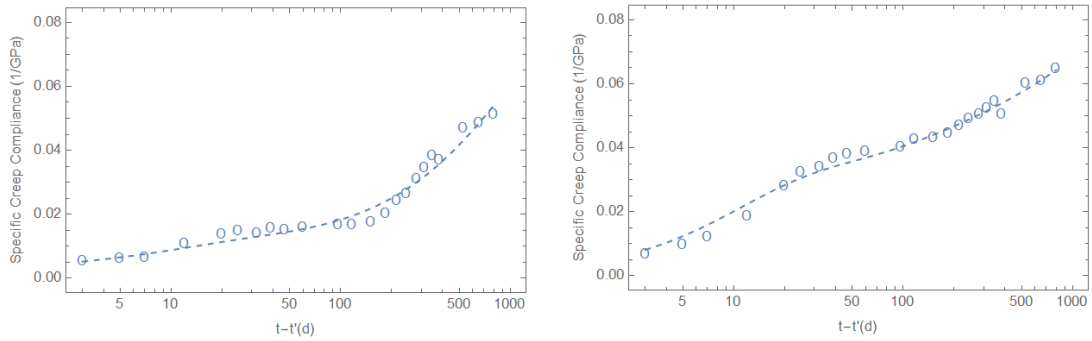

(b) 60ºC

Figure 4-8 Specific creep compliance on a log time scale for three different temperatures.

Figure 4-9 shows the graph of the compliance function at different temperatures obtained using the eqs. (4) -(44). The creep compliance clearly increases with increasing

temperatures due to larger creep strains. There is insignificant variation in the $J(t)$ calculated using the two methods at both the temperatures; this implies that the approximate methods may be used to simplify the calculations.

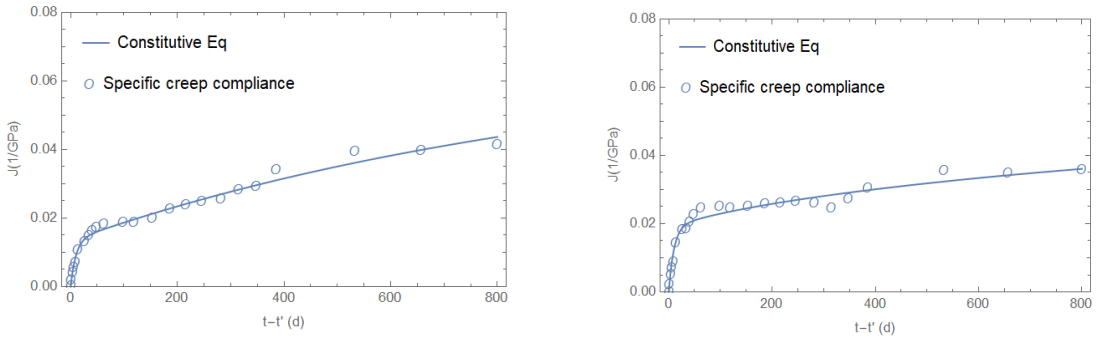

(a) 20ºC

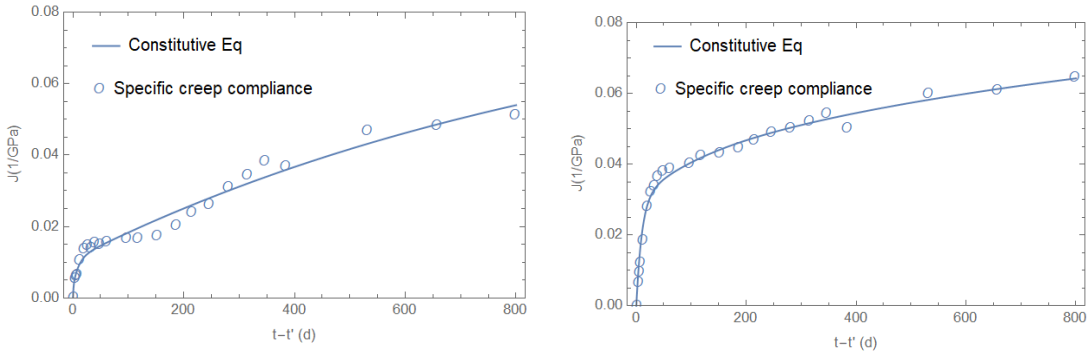

(b) 60ºC

Figure 4-9 Creep compliance functions fitted to the specific creep compliance at 20ºC and 60ºC.

4.4. Evaluation of the Significance of Drying Creep in Concrete Experiments

To assess the significance of the drying creep component in concrete test, the B4 model was used. As detailed in Chapter 2, using the model, the internal moisture history of the samples was back calculated using the constitutive equation relating the free strain to the average humidity history in the B4 model (Bažant et al. 2014). Then using the mix design composition and humidity profile, the basic and drying creep components of compliance were subsequently estimated using the B4 model in order to assess their relative magnitude.

4.4.1. Back Calculation of Humidity Profile

The B4 model uses only the drying shrinkage in the back calculation of spatially averaged relative humidity, h. This approach was recently updated stating that individual shrinkage components cannot be modelled independently and must be considered coupled (Rahimi-Aghdam et al. 2017). Furthermore, as shown by Leung and Grasley both drying and autogenous shrinkage (from self-desiccation) are caused by pore pressure reductions associated with reductions in the internal h (Grasley and Leung 2011). Hence, herein the total free strain obtained from experiments was used in the back calculation of humidity profile according to

$$h = \sqrt[3]{1 - \left(\frac{\varepsilon_{sh,total}(t,t_0)}{\varepsilon_{sh\infty}(t_0) \cdot S(t)} \right)}. \tag{45}$$

Here, $\varepsilon_{sh\infty}(t,t_0)$ is the "ultimate shrinkage," which in the B4 model depends on the mix design composition and the effect of aging on elastic stiffness. $S(t)$ is a time curve dependent on present time (t), the time at onset of drying (t_0) and shrinkage halftime (

τ_{sh}). The variation of h in the concrete samples as a function of time and temperature is shown in Figure 4-10.

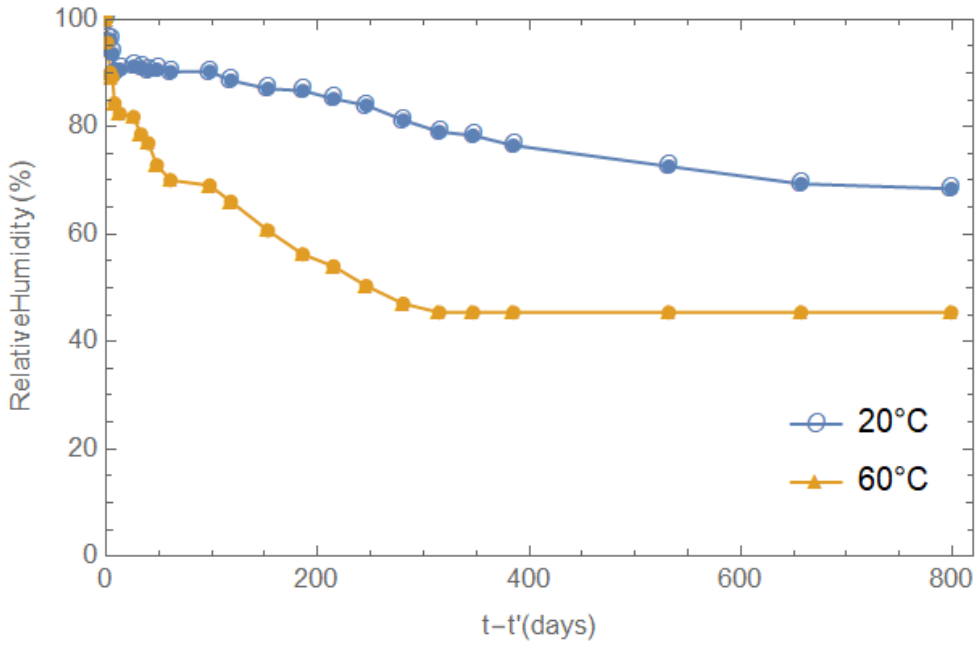

Figure 4-10 Spatially averaged relative humidity (h) inside the concrete samples back-calculated using the free strain history.

4.4.2. Basic and Drying Creep

Bažant's B4 model and B3 model illustrates a step-by-step procedure to calculate the basic and drying creep compliance functions (Bažant et al. 2014; Bažant and Baweja, 2000). Figure 4-11 depicts a comparative representation of the total creep compliance and the basic and drying creep compliance components at 20ºC and 60ºC as predicted by the B4 and B3 model.

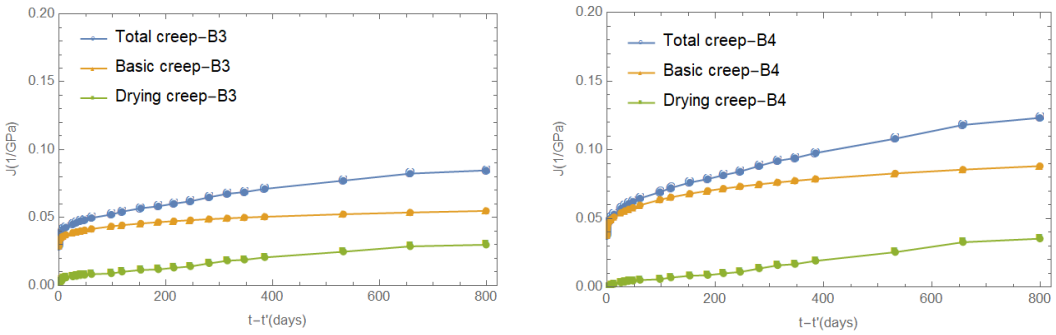

(a) 20ºC

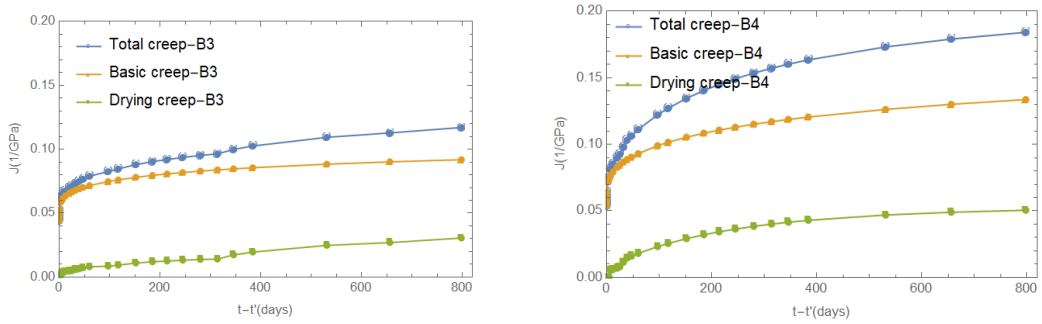

(b) 60ºC

Figure 4-11 B3 and B4 model used to depict the components of creep compliance (i) Total creep, (ii) Basic creep and (iii) Drying creep.

From Figure 4-11, it is clear that the components of compliance are calculated differently in the two models. It is known that the B4 model's drying creep is three times higher than drying creep obtained from B3 model (Bažant and Jirasek, 2018). Now, comparing the experimental data to both the models, we can decide the model that best fits the scenario (Figure 4-12).

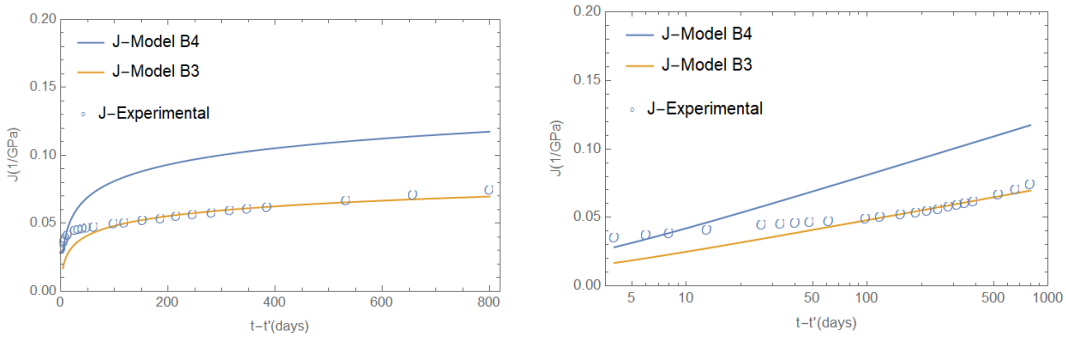

(a) 20ºC

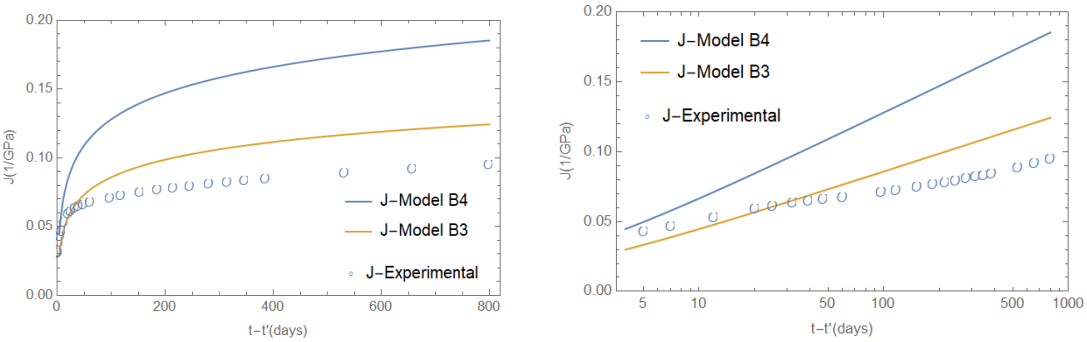

(b) 60ºC

Figure 4-12 The total creep compliance from the experiment plotted against the total creep compliance from the B3 and B4 model in regular and log time scale.

Figure 4-12 shows that the B3 model fits more accurately with the experimental data compared to the B4 model. This is explained in Fig. D10. (a). of the Creep and Hygrothermal Effects in Concrete Structures book (Bažant and Jirasek 2018), which shows that the total creep predicted using B4 model is always higher compared to the B3 model due to differences in the creep parameters used for predicting compliance. Another major finding is that the B3 model seem to closely predict the extrapolated 20°C long-term creep compliance of concrete (Figure 4-12).

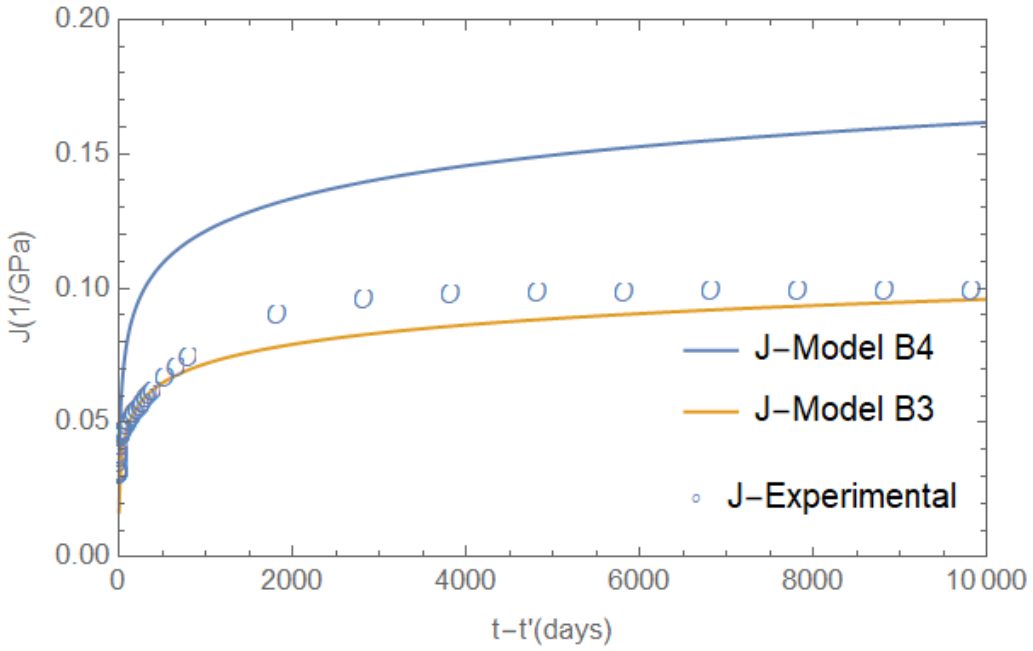

Figure 4-13 Long-term extrapolated creep compliance plotted against the total creep compliance from the B3 and B4 model.

4.5. Creep Compliance Master Curve for Concrete using TTS Principle

Using the B3 model, the drying component of the creep was removed from the total experimental creep compliance to obtain the basic creep compliance. The basic creep curves obtained at 20°C and 60°C were plotted on a logarithmic time axis. It was observed that the creep compliance curves were similar shapes, implying that the material was thermorheologically simple. Hence the creep compliance curve at 60°C was shifted laterally to the right using the TTS principle to obtain a creep compliance master curve at room temperature (20°C) as shown in Figure 4-14.

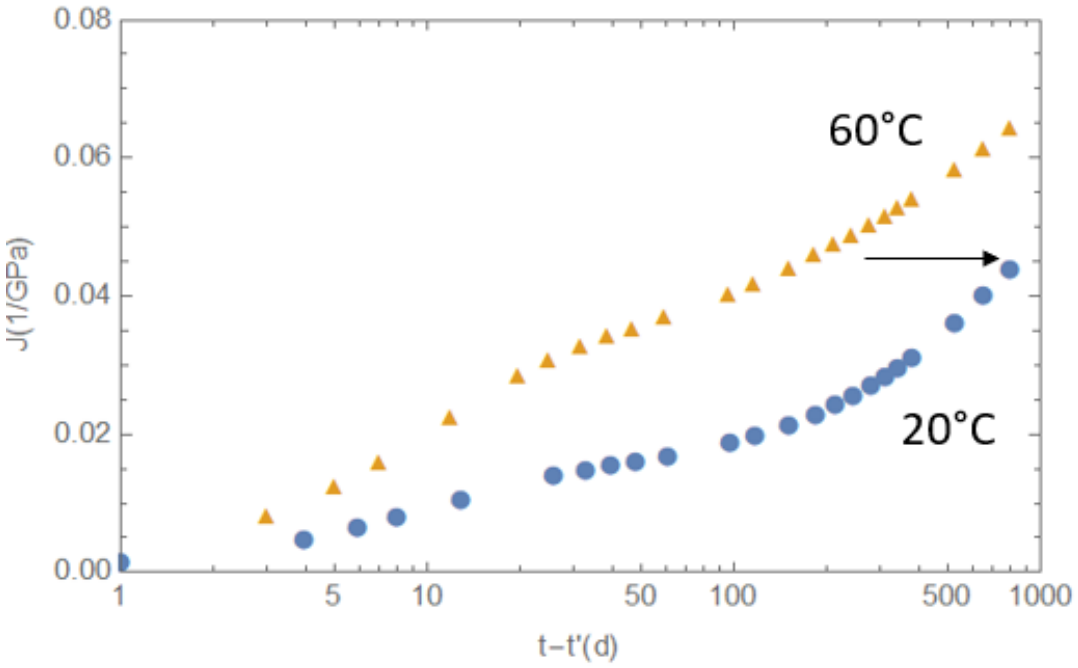

Figure 4-14 Basic creep compliance function at 60°C shifted along the logarithmic time axis to produce a basic creep compliance master curve at 20°C.

The temperature dependent shift factor, β_{Tc} that is needed to shift the curve laterally was calculated as

$$\beta_{Tc} = \frac{t}{t_r}, \tag{46}$$

where t is the present time and t_r is the reduced time. In this study, a β_{Tc} value of 12 was calculated for 60°C to shift the creep compliance data from higher temperatures to 20°C reference temperature (β_{Tc} =1 at 20°C) (Table 4-3).

Table 4-3 Shift factors for concrete at elevated temperature with respect to reference temperature.

Temperature	Shift Factor
20ºC	1
60ºC	12

A basic creep compliance master curve was obtained to predict creep of concrete for up to 9,800 days ~ 27 years using creep experiments performed for 800 days. The shifted data was fitted into a five-unit logarithmic chain shown in equation 9. The creep compliance has units of 1/GPa.

$$J(t) = 0.0047 Log\left[1+t\right] + 2.8379*10^{-9} Log\left[1+\frac{t}{10}\right] + 7.1326*10^{-9} Log\left[1+\frac{t}{100}\right] + 6.9882*10^{-8} Log\left[1+\frac{t}{1000}\right] + 0.0047 Log\left[1+\frac{t}{10000}\right] \quad (47)$$

The creep compliance master curve is presented in Figure 4-15. The master curve allows for predicting creep in structures for several decades beyond the range of the original results obtained using laboratory creep experiments.

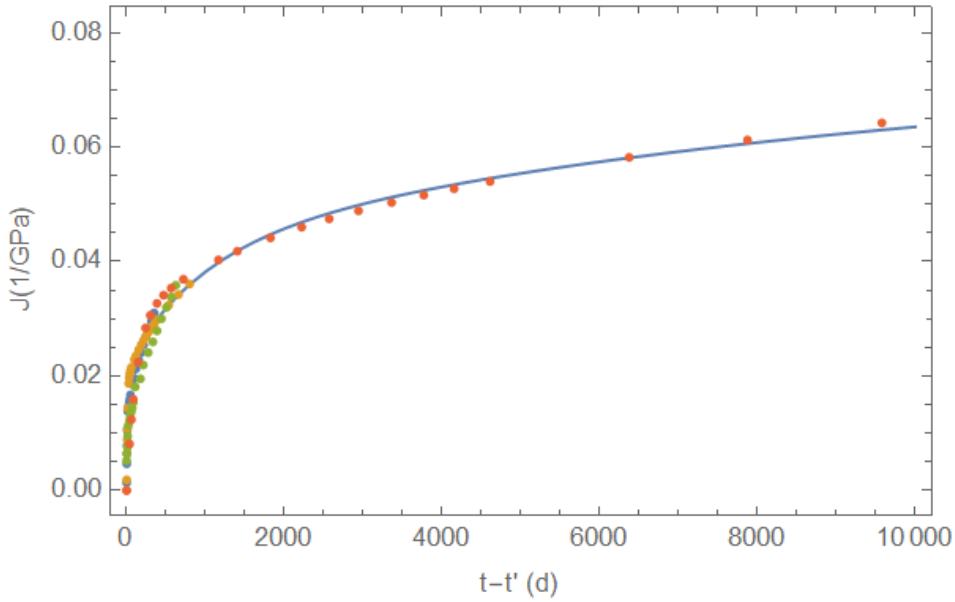

(a)

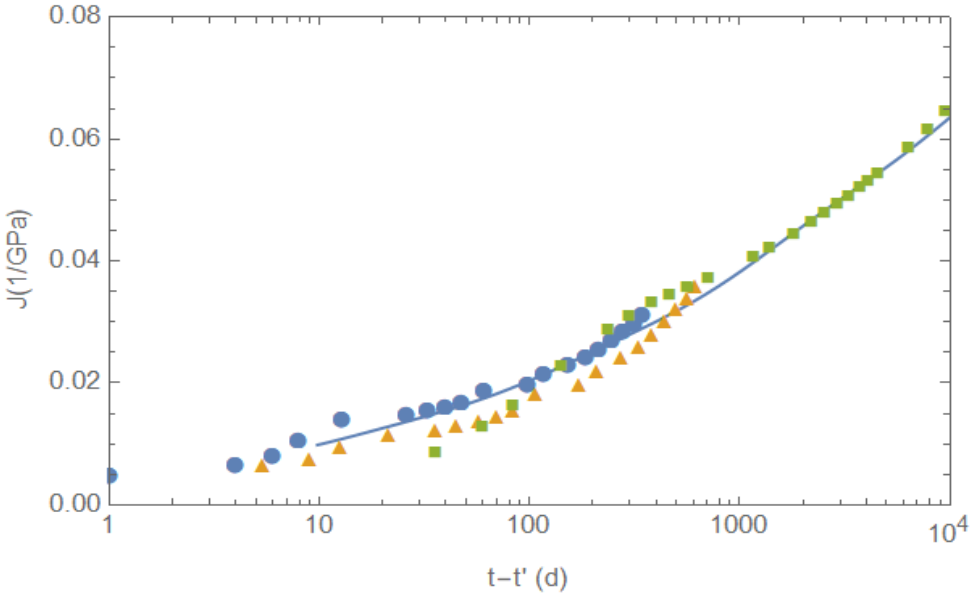

(b)

Figure 4-15 Basic creep compliance master curve in (a) normal time scale and (b) logarithmic time scale.

4.5.1. Comparison of Master Curve with B3 and B4 Model

The basic creep compliance master curve was compared to the basic creep obtained from B3 and B4 model. It can be seen the B3 model is the closest to the master curve. Even though it fits quite well in the first few years, there is a 18% difference in the compliance at 9,800 days (Figure 4-15).

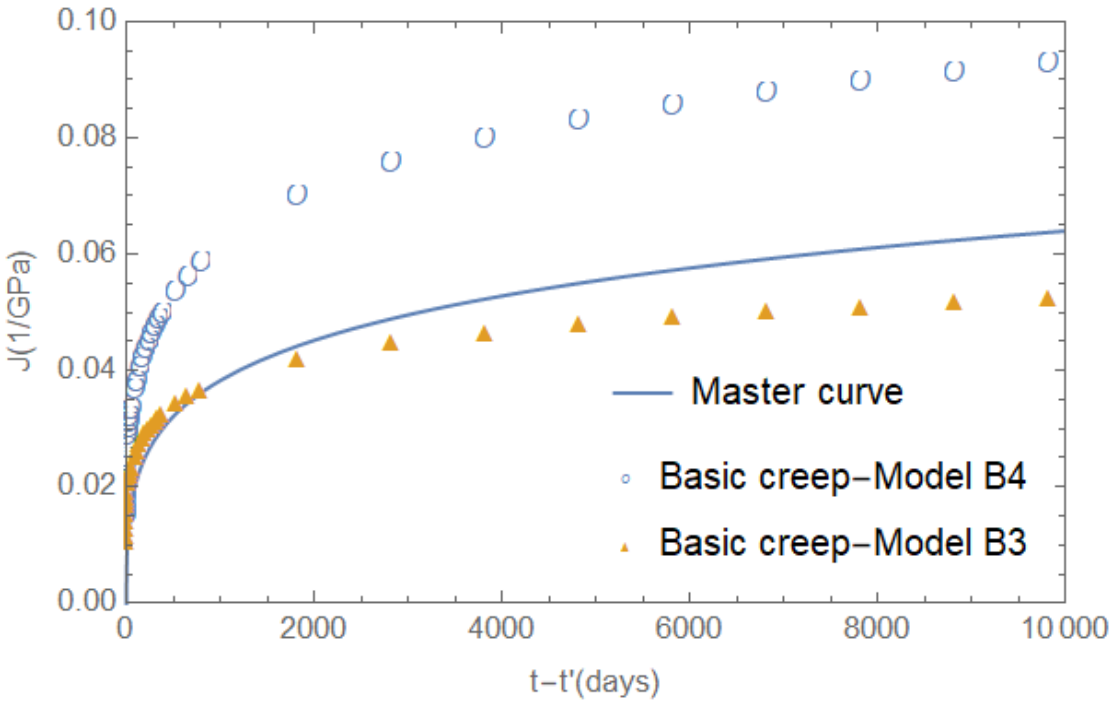

Figure 4-16 Basic creep compliance master curve plotted against basic creep compliance from B3 and B4 model.

4.5.2. Comparison of Master Curve to Upscaled data

The 3D creep data from the confined experiment was upscaled to obtain concrete creep using advanced computational composite models that accounts for the presence of realistic aggregates, their geometry, and distribution as obtained through innovative experimental tomography of real concrete aggregates. Our Collaborator, Ed Garboczi from NIST has

performed extensive work to quantify the shapes of real aggregates using X-Ray CT. He used spherical harmonics function to define the surface of aggregates in a spherical coordinate system. Spherical harmonics was used to recreate the real shapes of aggregates and generate an accurate representation of concrete. The variability in concrete creep due to aggregate distribution and mix design can be captured readily by simulating various 3D microstructures of concrete using this technique. Once the concrete microstructure was simulated, OOF3D software was used for meshing. This mesh was uploaded to Abaqus for finite element analysis where virtual creep experiments were conducted on concrete (Torrence et al., 2019a and 2019b). The viscoelastic material properties of cement mortar from the uniaxial and confined experiments was used as an input here. Aggregates were assumed to behave linear elastic. With this approach, many virtual experiments can be run in matter of few days, whereas the associated concrete creep laboratory experiments would take far longer. For validation purposes, the simulated concrete creep tests are compared to the master curve and the results are shown in Figure 4-15.

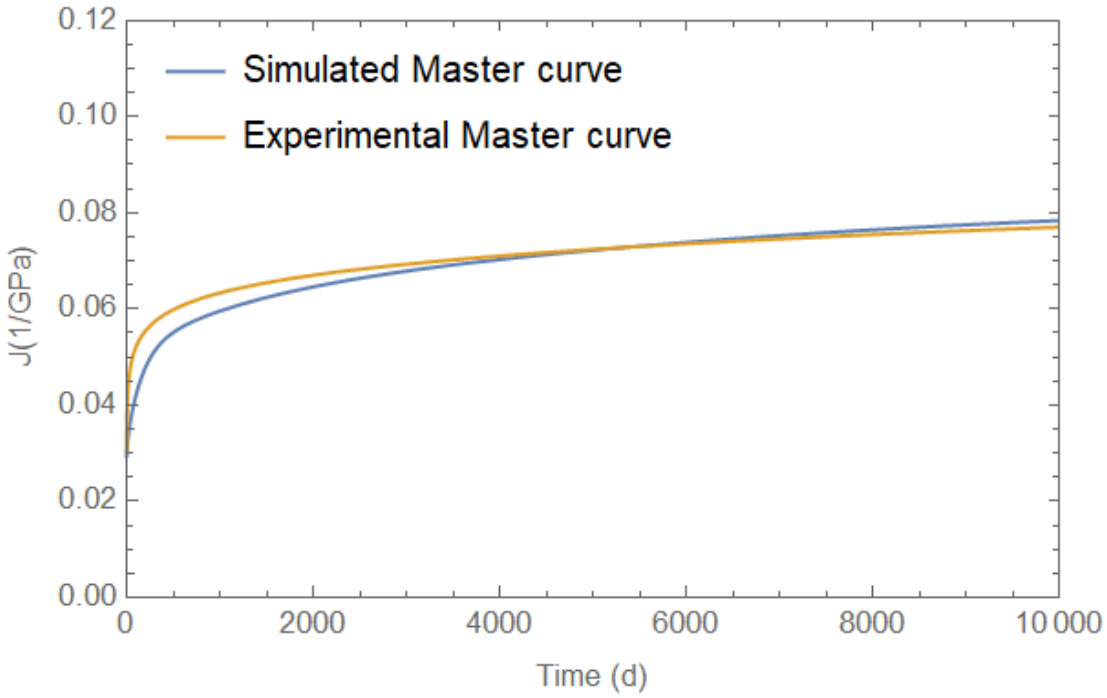

Figure 4-17 Creep compliance master curve plotted against the master curve simulated from upscaling approach.

4.6. Mechanical Properties

It is well known that concrete creep causes prestress losses in steel reinforcement with time. At the time of repairs, it is critical to be aware of the residual mechanical properties of the material that has undergone creep. Hence, in the current study the mechanical properties (i.e. dynamic modulus and tensile strength) of concrete is investigated.

4.6.1. Dynamic Modulus

At the end of creep tests, the concrete cylinders are pulled out and the dynamic modulus of the sample was evaluated in accordance to ASTM C215-19. The experiment is based on the principle of fundamental resonant frequencies using the impact resonance method. In this method, the specimen is struck with an impactor and the response is collected by

an accelerometer. The accelerometer records the fundamental frequency of vibration. Two different modes of vibration were tested: transverse mode and longitudinal mode. In the transverse mode, the impact strikes the specimen on the circumferential surface whereas, in the longitudinal mode, the impactor strikes the surface on end of the sample longitudinally. Once the resonant frequencies are picked up, the dynamic Young's modulus of elasticity, E is calculated as follow:

$$E_T = \frac{1.6067 * L^3 * T * M * n^2}{d^4} \tag{48}$$

where, L is the length of specimen in meters, M is the mass of specimen in kg, n is the fundamental transverse frequency in Hz, d is the diameter of the specimen in meters and T is a correction factor that depends on radius of gyration, Length of specimen and Poisson's ratio.

$$E_L = \frac{5.092 * L * T * M * n'^2}{d^2} \tag{49}$$

where, n' is the fundamental longitudinal frequency in Hz.

The results from the experiment on concrete samples that were unloaded (free) and loaded (undergone creep) are shown in Figure 4-15. It can be seen that there is slight increase in stiffness (around 10%) on concrete samples that had undergone creep for 800 days.

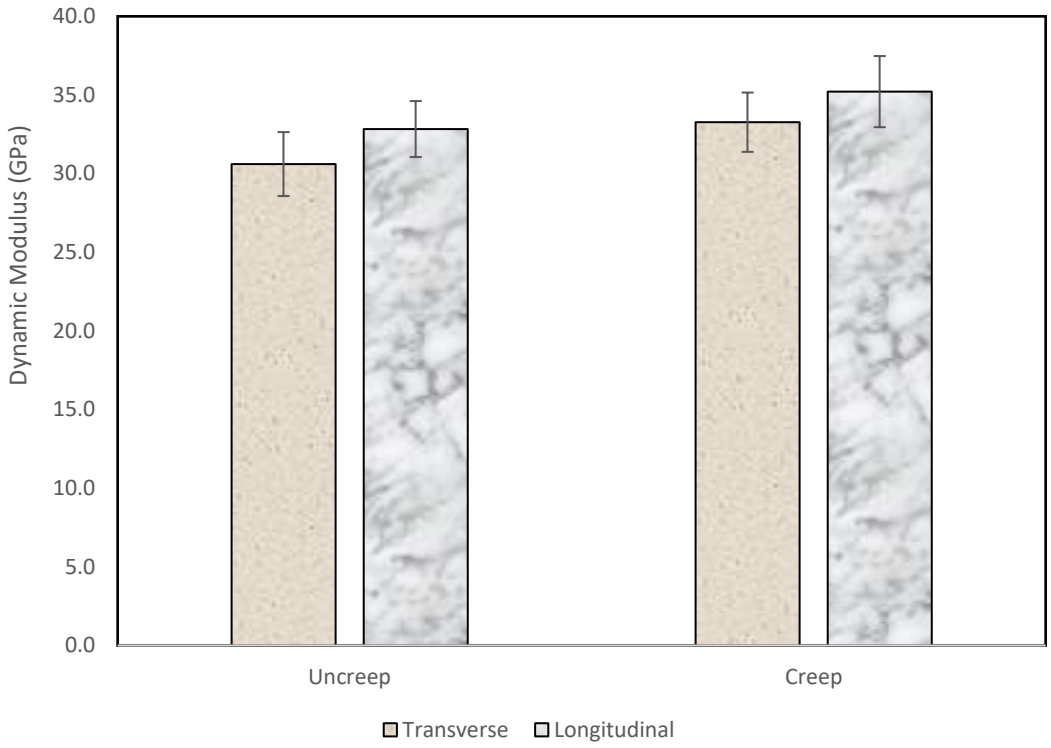

Figure 4-18 Transverse and Longitudinal Dynamic Modulus of concrete on loaded and unloaded specimens.

4.6.2. Split Tensile Test

Since the dynamic modulus test is a non-destructive test, the same samples were broken under split tensile test. The test was conducted in accordance to ASTM C496. Two bearing strips (usually plywood) 3 mm thick, 25 mm wide, and length equal to that of the specimen was used between the specimen and supplemental plates. Load was applied continuously at the rate of 0.7 to 1.4 MPa/min splitting tensile stress until failure. The maximum load applied at failure was noted. The splitting tensile strength of the specimen was calculated as:

$$T = \frac{2P}{\pi ld} \tag{50}$$

where, P is the maximum load applied causing failure in N, l is the length of the specimen in mm and d is the diameter of the specimen in mm. Figure 4-15 shows the experimental set up.

Figure 4-19 Experimental set up of splitting tensile test.

The test was conducted on unloaded (free) specimen as reference and on specimens under load for 800 days. Figure 4-15 shows the mean results of 4 cylinders tested in each category along with standard error. Though creep has not greatly affected the strength of the concrete, there is still a decrease in strength compared to virgin samples. Creep strains

have been known to induce structural failure, especially when the stress levels are very high (Bažant et al. 2012).

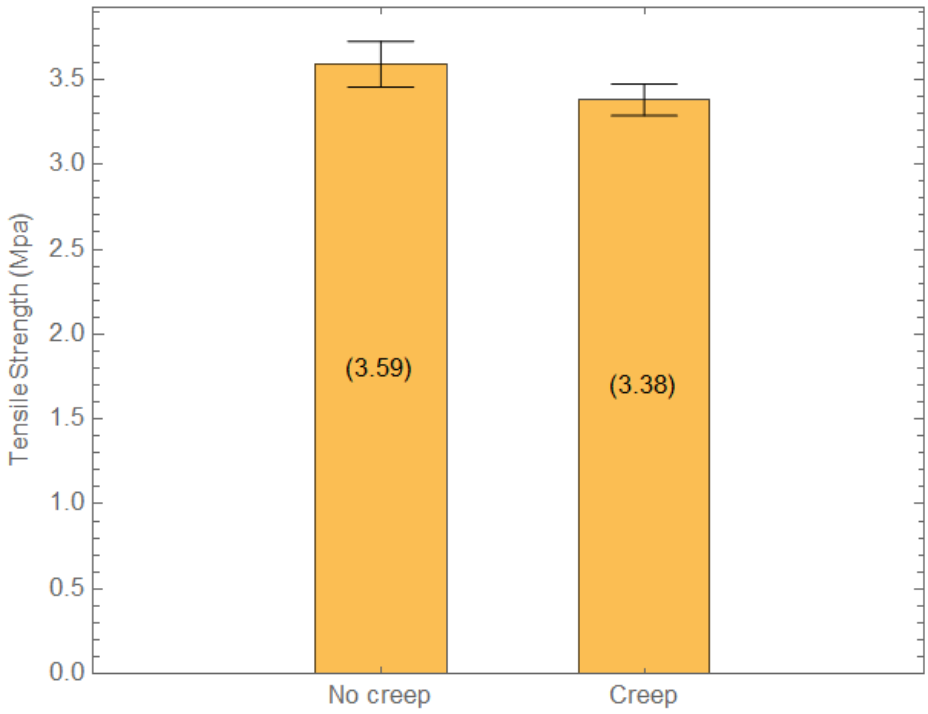

Figure 4-20 Splitting tensile strength of concrete specimens with no creep and creeped sample.

4.7. Summary and Conclusions

This chapter presents the long-term creep response of concrete examined by conducting creep tests using a mix design resembling the VeRCoRs concrete used by EDF. The creep tests were run at 20°C and 60°C for 800 days. The following conclusions can be drawn:

- The magnitude of creep strain measured after 800 days increased by a factor of 1.60 at 60ºC compared to the creep strain at 20ºC.

- Creep compliance was calculated using the simple division method and the constitutive equation utilizing the convolution integral.
- The TTS principle was successfully used to generate a creep compliance master curve to predict concrete creep response for up to 9,800 days (nearly 27 years) at a reference temperature of 20°C. A constitutive equation for creep compliance was also proposed to accompany the master curve. By running creep tests at 60°C, creep at 20°C was predicted at 12 times the time duration of the 60°C test using temperature shifting.
- The Bažant B3 and B4 models were applied to compare the total creep compliance from experiments. The B3 model fitted more accurately with the experimental data compared to the B4 model. The long-term extrapolated creep compliance at 20°C also fitted well with the B3 model. The relative humidity inside the concrete sample was back calculated using the free strain data.
- The compliance was plotted against the simulation results from the upscaling method using 3D constitutive properties of mortar. Though the data obtained and the simulation results did not fit exact during the initial few days, the long-term creep results matched satisfactorily.
- The mechanical properties of the samples that had undergone creep were tested. As expected, the samples showed an increase in stiffness, whereas the split tensile strength was lower compared to the virgin samples.

References

1. Bažant, Z. P. and Baweja, S.: Creep and Shrinkage Prediction Model for Analysis and Design of Concrete Structures: Model B3. Am. Concrete Institute, Michigan, 1–83 (2000).
2. Bažant, Z. P.: Prediction of concrete creep and shrinkage: past, present and future. Northwestern, Nuclear Engineering and Design 203, 27-38 (2001).
3. Bažant, Z. P., Yu., Q. and Li, G.: Excessive Long-Time Deflections of Prestressed Box Girders. I: Record-Span Bridge in Palau and Other Paradigms. J. Struct. Eng. **138**, 676-686 (2012).
4. Bažant Z. P., Hubler, M., Wendner, R.: Model B4 for creep, drying shrinkage and autogenous shrinkage of normal and high-strength concretes with multi-decade applicability. TC-242-MDC multi-decade creep and shrinkage of concrete: material model and structural analysis. RILEM Mater Struct. (2014).
5. Bažant, Z. P., Jirasek, M.: Creep and Hygrothermal Effects in Concrete Structures. Sol. Mech. Appl. **225** (2018).
6. Benboudjema, F., Meftab, F. and Torrenti, J. M.: Interaction between drying, shrinkage, creep and cracking phenomenon in concrete, France..Engineering Structures 27, 239-250. (2005).
7. Brooks, J.J.: 30-year creep and shrinkage of concrete. Mag. Conc. Res. **57** (9), 545-556 (2005).

8. Browne, R. D. and Blundell, R.: The influence of loading age and temperature on the long-term creep behavior of concrete in a sealed, moisture stable state. Mat. Struct. **2** (8), 133-143 (1969).
9. Charpin, L., Le Pape, Y., Coustabeau, E., Toppani, E., Heinfling, G., Le Bellego, C., Masson, B., Montalvo, J., Courtois, A., Sanahuja, J. and Reviron, N.: A 12 year EDF study of concrete creep under uniaxial and biaxial loading. Cem. Conc. Res. **103**, 140-159 (2018).
10. Gopalakrishnan,K.: Creep of concrete under multiaxial compressive stresses. Univ of Calgary, Canada, PhD thesis. (1968).
11. Hanson, J. A.: A 10-year study of creep properties of concrete. Engineering Laboratories Branch, Design and Construction Division (1953).
12. Hatt, W. K.: A Note on the Effect of Time Element in Loading Reinforced Concrete Beams. Engineering News **58**(17): 438–439 (1907).
13. Kesler, C.E.: Creep behavior of portland cement mortar and concrete under biaxial stress. UIUC, (1977).
14. Kommendant, G. J., Polivka, M., and Pirtz, D.: Study of concrete properties for prestressed concrete reactor vessels. Final report UCSESM 76-3 (to General Atomic Company). UC Berkeley (1976).
15. Mc Donald, J. E.: Time dependent deformation of concrete under multiaxial stress conditions. In: Technical Report C-75-4 Concrete Laboratory, US Army Engineering Waterways Experiment Station, Vicksburg, MS (1975).

16. McDonald, J. E.: Creep of concrete under various temperature, moisture, and loading conditions. Final report. Reactor vessels, Illinois Univ.Urbana for ORNL (1975).
17. Nasser, K. W. and Neville, A. M.: Creep of Concrete at Elevated Temperature. ACI J. Proc. **62** (12), 1567-1579 (1965).
18. Neville, A. M., Dilger, W. H., and Brooks, J. J.: Creep of plain and structural concrete. Construction Press. (1983).
19. Ross, A.D.: Experiments on the creep of concrete under two-dimensional stressing. Mag. Conc. Res. 6 (16). pg. 3-10, Univ. of London, King's College, (1954).
20. Sellier, A., Stephane, M., Laurie, B., Vidal, T., Bourbon, X. and Camps, G.: Concrete creep modelling for structural applications: Non-linearity, multi-axiality, temperature and drying effects. France. Cem. Conc. Res. (2016).
21. Torrence, C., Baranikumar, A. and Grasley, Z.: Nuclear concrete microstructure generation and analysis of long-term performance. 19th International Conference on Environmental Degradation of Materials in Nuclear Power Systems – Water Reactors, Boston, August 18-22, American Nuclear Society (2019a).
22. Torrence, C.E., Baranikumar, A. and Grasley, Z.: Homogenization of concrete in nuclear power plants. 25th International Conference on Structural Mechanics in Reactor Technology, Charlotte, August (2019b).
23. Torrenti, J. M. and Le Roy, R.: Analysis and Modelling of Basic Creep. CONCREEP 10, 1400-1409. France (2015).

24. Troxell, G. E., Raphael, J. M. and Davis, R. E.: Long-time creep and shrinkage tests of plain and reinforced concrete. Sixty-first Annual meeting of the Society, June 22-27 (1958).
25. Wittmann, F.H. and Roelfstra, P.E.: Total deformation of loaded drying concrete. Delft. Cem. Conc. Res., 10, pg. 601-610, (1980).

5. SUMMARY AND CONCLUSIONS

5.1. Summary

The primary objective of this research was to predict long-term creep at room temperature, 20°C for up to 60 years in concrete structures part of nuclear containment facilities using laboratory experiments conducted for shorter time periods i.e. less than 2 years. Towards this end, a unique mortar creep frame was designed that is amenable to placement in climatic chambers thereby facilitating creep measurements at higher temperatures namely 60°C and 80°C in addition to measurements at 20°C. The creep measurements recorded at higher temperatures for over 600 days was utilized to develop a master curve to predict creep compliance using the concept of time-temperature superposition. The creep prediction was composed of two phases; a uniaxial creep prediction of cement mortar samples followed by a 3D creep prediction of cement mortar samples of same mix design using confined testing conditions. In the first phase, the uniaxial creep compliance, J(t) was measured and modelled whereas, in the second phase of work, the bulk compliance, B(t), shear compliance, L(t) and viscoelastic Poisson's ratio of cement mortar was measured and modelled. These parameters formed as an input to upscale and predict the creep compliance of concrete using computational algorithms in a parallel study (Torrence et al. 2019a and 2019b). In addition to the tests conducted on cement mortar, uniaxial creep measurements were obtained on concrete samples to experimentally validate the computational predictions obtained by upscaling the creep parameters obtained on cement mortars.

5.2. Conclusions

The primary contribution of this work is the development of a robust, experimentally validated model to predict creep in nuclear concrete structures for up to 60 years using short-term creep data thereby enabling a longer service life of critical facilities and early detection of structural failure.

The significant findings obtained as part of the study include the following:

- Creep increases as a function of temperature. The magnitude of creep strain increased by a factor of 1.50 and 2.40 at 60ºC and 80ºC, respectively, compared to the creep strain at 20ºC measured at 600 days.
- Neglecting the time variance in stress (constant stress method) resulted in a 42% and 60% error (600 days after loading), respectively, at 60ºC and 80ºC. At higher temperatures, it is recommended to properly account for the stress history during the experiment by utilizing the convolution integral constitutive equation when calculating the compliance. Unfortunately, most researchers use the constant stress method which can lead to underprediction of creep compliance.
- For the first time, the TTS principle was successfully used to generate a uniaxial creep compliance master curve to predict mortar creep response for up to 22,500 days (nearly 60 years) at a reference temperature of 20°C.
- By running creep tests at 80°C, creep at 20°C was predicted at 37 times the time duration of the 80°C test using temperature shifting.

- The activation energy for mortar creep is essentially the same as the activation energy for cement hydration. Since hydration rate is suggested to be diffusion controlled, the implication is that long-term creep rate may also be diffusion controlled.
- The confined creep test was used to determine the dilatational and deviatoric compliance functions. It was observed that the dilatational and deviatoric compliance functions showed a similar trend at 20ºC whereas, at 60ºC, the rate of change of deviatoric compliance was slightly higher compared to dilatational compliance.
- Using the intermodulus conversion, the viscoelastic Poisson's ratio of cement mortar was found to be a nearly constant value of 0.14 at 20ºC and increased from 0.17 to 0.19 over a period of 100 days after initial loading at 60ºC.
- The uniaxial compliance calculated from the bulk and shear relaxation moduli was higher than measured directly, with the magnitude of the difference seeming to depend on the magnitude of the strain energy present in the test.
- From the concrete creep test, uniaxial creep compliance master curve was developed that predicts concrete creep response for up to 9,800 days (nearly 27 years) at a reference temperature of 20°C.
- The Bažant B3 and B4 model was used to compare the total creep compliance from the experiments. It was seen that the B3 model fits more accurately with the experimental data compared to the B4 model. The long-term extrapolated creep compliance at 20°C fits well with the B3 model as well.

- The concrete creep compliance from experiments was in good agreement with the simulation results using the upscaling method from cement mortar constitutive properties.
- The concrete samples under creep showed an increase in stiffness, whereas the split tensile strength showed a decrease in strength compared to the virgin samples.

5.3. Limitations of the model

Though the major contribution of this work is the creation of a model that can predict creep of cement mortar for up to 60 years, it is imperative to revisit some of the assumptions made in the study to understand the limitations of the model:

- In this study, the stress levels applied on the cement mortar as well as concrete samples remained well within the linearity range. An assumption was made that the cementitious materials will behave linearly for stress levels up to 0.4 times the compressive strength, but no test was conducted to validate this assumption before the study began. Also, in a nuclear concrete during a repair activity, when there is redistribution of stresses, concrete may undergo stress levels in the non-linearity range. At that time, the model created in the study may not be used.
- The master curve developed in this study is the creep compliance function at room temperature or 20ºC. A nuclear reactor may experience fluctuating temperature gradients with a high temperature close to 300ºC. The creep

compliance will have to be calculated for high temperatures using the shift factors as explained in this dissertation.

- Other deformations in a nuclear reactor such as radiation and thermal aging effect can degrade the concrete structure and affect the rate of creep. In such case, a correction factor may be needed in the model to accelerate creep.

5.4. Recommendations for Future Work

In this section, recommendations for improving the accuracy of experimental concrete creep predictions are made based on the lessons learnt during this work. The key considerations to account for in future studies measuring concrete creep are listed below:

- One of the largest sources of error in the experimental tests conducted herein in this work is the addition of the drying creep component in the total concrete creep. Even though samples were sealed using adhesive backed aluminum foil, it was later realized from other literatures that samples require at least 3 layers of sealing. Though this issue was resolved using B3 and B4 models and separating out the basic creep components, it should be avoided in future studies.
- Creep is sensitive to mix design and stress levels. In this study only one mix design was reviewed and based on the capacity of springs used in the miniaturized creep frames, stress levels corresponding to 10% of maximum compressive strength of cement mortar was used. It would be interesting to see how the constitutive properties especially viscoelastic Poisson's ratio is affected by stress levels.

- The study initially used embedded strain gages for measuring strains in the sample which drifted with time and the results were not reasonable. This prompted us to use the embedded vibrating wire gage which proved to be accurate and reliable.
- The viscoelastic Poisson's ratio was found to be constant at 20ºC but slightly increasing with time at 60ºC. A more extensive test program is necessary to make a firm conclusion on the time and temperature dependence of viscoelastic Poisson's ratio of cementitious materials.

Future work addressing the above said gaps in the experimental methods will be helpful towards developing a more powerful tool for predicting creep and creep cracking in nuclear concrete structures.

References

1. Torrence, C., Baranikumar, A. and Grasley, Z.: Nuclear concrete microstructure generation and analysis of long-term performance. 19th International Conference on Environmental Degradation of Materials in Nuclear Power Systems – Water Reactors, Boston, August 18-22, American Nuclear Society. (2019a).
2. Torrence, C.E., Baranikumar, A. and Grasley, Z.: Homogenization of concrete in nuclear power plants. 25th International Conference on Structural Mechanics in Reactor Technology, Charlotte, August (2019b).

APPENDIX A

RH HISTORY IN SAMPLES TO SUPPORT B3/B4 MODEL

In order to support the analysis from B3 and B4 model on drying creep, three prisms for cement mortar of dimensions 2.54 cm x 2.54 cm x 29.36cm (1"x 1" x 11.56") and three prisms for concrete of dimensions 7.62 cm x 7.62 cm x 29.36cm (3" x 3" x 11.56") were prepared using the mix design specified in Table 2-1 of chapter 2 and Table 4-1 of Chapter 4, respectively. The mass of the samples was continuously monitored for over a year. Parallelly, crushed samples of cement mortar and concrete were placed in desiccators at different relative humidities to obtain a desorption isotherm curve. The standard desiccator method using different salt solutions to generate varying RH environment in the container was employed. This method has been in practice for long time due to its simplicity and reliability. But depending on the material and sample size, the time to reach equilibrium with the surrounding environment can vary anywhere between few days to a year (Johannesson and Janz, 2002). In the current test, big chunks of cement mortar and concrete samples were crushed to small pieces in an attempt to accelerate the tests. Several researchers in the past have successfully utilized crushed or sawn small samples to create desorption isotherm curves (Mikhail et al. 1973; Daian;1988; Baroghel-Bouny et al. 1999; Ishida et al. 2007, Sémété, et al. 2015).

Experimental Procedure

A sample of cement mortar and concrete cylinder was prepared and was sliced into thin discs and placed in a water bath for 28 days. At this age, the sample is assumed to be fully

matured. The thin discs were then taken out and crushed into small pieces (up to one centimeter maximum) which helps to increase the surface area for diffusion. The crushed pieces were placed in a glass petri dish on a rack inside a water bath. The samples were in the water bath for two weeks or until it reached equilibrium such that there was no increase in mass for atleast three consecutive days. This mass was noted as M_{SSD}. In the meantime, nine different salt solutions were prepared according to the international Commission of the European communities (Jowitt and Wagstaffe, 1989). The salt solutions were placed in air tight dessicators. A wireless sensor tag was set in the desiccator to monitor the humidity levels. The salts and the different RH conditions obtained in the desiccators are detailed in Table A - 1 below:

Table A - 1 Saturated salts and their relative humidity

Salts	**RH at 20°C**[2]	**RH obtained**
Silica gel	3%	0-8%
Lithium chloride	11.3%	12%
Magnesium chloride	33.1%	33%
Sodium bromide	59.1%	59%
Sodium chloride	75.5%	75%

[2] Source: L. Greenspan, "Humidity Fixed Points of Binary Saturated Aqueous Solutions", Journal of Research of the National Bureau of Standards - A. Physics and Chemistry, 1977, 81A (1) pp. 89-96.

Table A - 1 Continued.

Salts	RH at 20°C	RH obtained
Potassium chloride	85.1%	86%
Potassium nitrate	94.5%	95%
Potassium sulfate	98%	99%
Deionised water	100%	100%

The entire experiment was conducted in an environmental chamber maintaining constant temperature of 20°C and RH of 50%. The saturated surface dry samples were placed in different desiccators and allowed to dry and reach equilibrium with the surrounding. In the drying process, the samples were weighed regularly by taking it out of the container and placing on an external weighing scale with accuracy of ±0.1 mg. The duration between taking the sample out and putting them back was less than 15 seconds. In order to construct the desorption isotherm curve, a reference dry state was required for the samples. This was obtained by oven-drying the samples at 105°C for 24 hours or until there was no variation in mass. The experimental set up is shown in Figure A- 1.

Figure A- 1 Crushed samples stored in a desiccator at varying RH environments.

Results

The Relative humidity of the salts were constantly monitored throughout the course of experiment using the wireless sensor tags. The RH levels of the salts are shown in the graphs below (Figure A- 2):

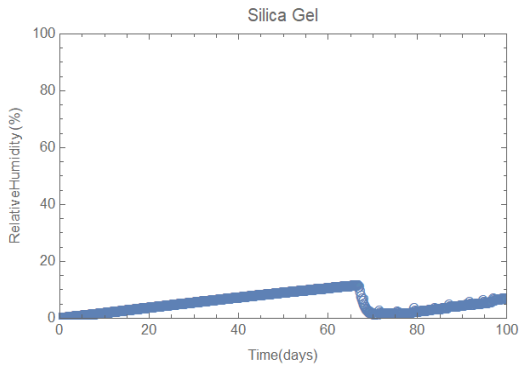
Silica Gel
RelativeHumidity (%)
Time(days)
0
20
40
60
80
100

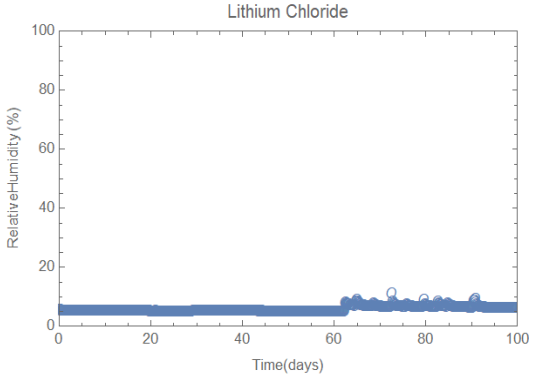
Lithium Chloride
RelativeHumidity (%)
Time(days)
0
20
40
60
80
100

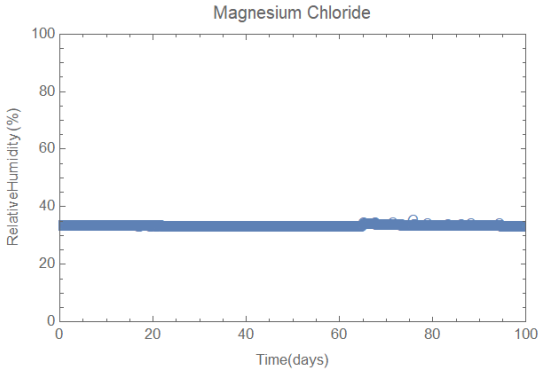
Magnesium Chloride
RelativeHumidity (%)
Time(days)
0
20
40
60
80
100

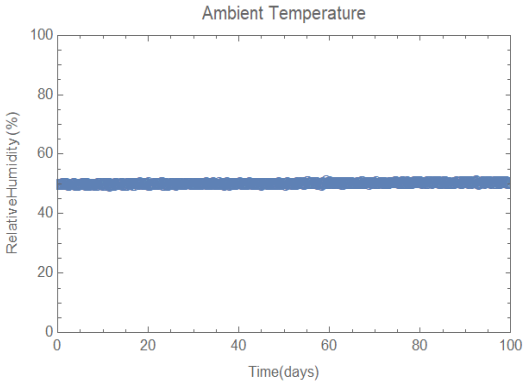
Ambient Temperature
RelativeHumidity (%)
Time(days)
0
20
40
60
80
100

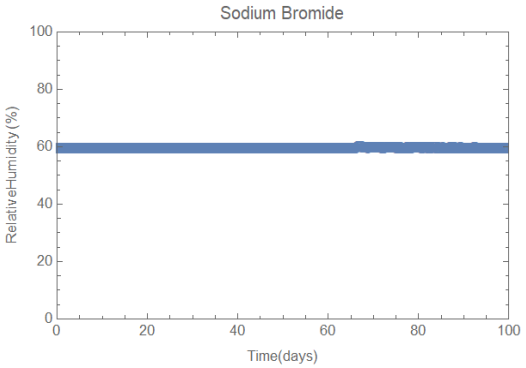
Sodium Bromide
RelativeHumidity (%)
Time(days)
0
20
40
60
80
100

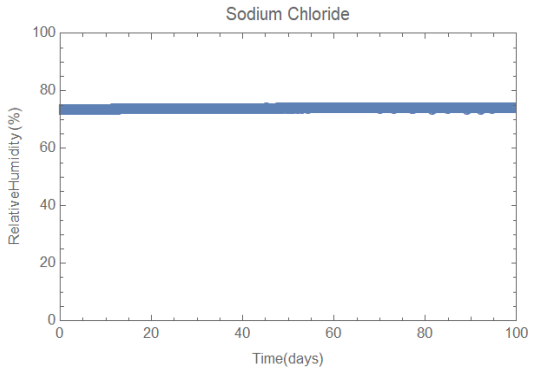
Sodium Chloride
RelativeHumidity (%)
Time(days)
0
20
40
60
80
100

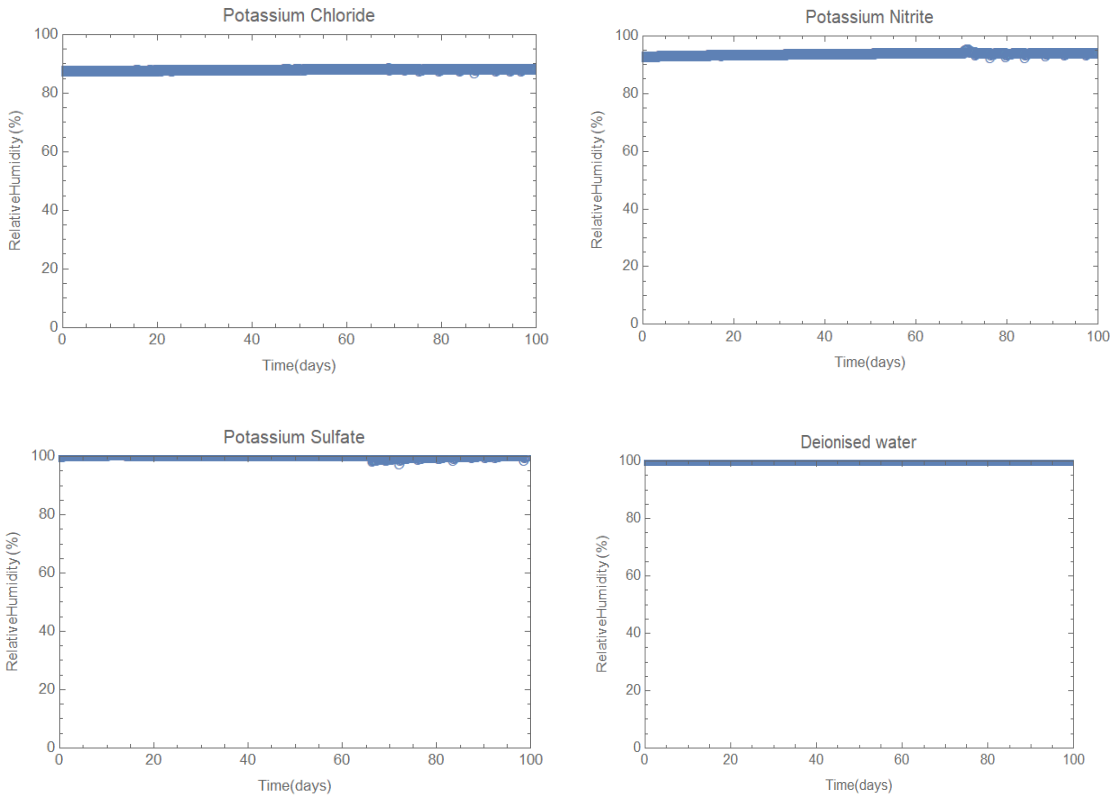

Figure A- 2 RH levels of various salts monitored throughout the experiment.

The mass loss from periodic mass measurements at various RH environments can be expressed as:

$$\left(\frac{\Delta m}{m}\right)(t) = \frac{m(t) - m_0}{m_0} \tag{51}$$

where m(t) is the mass at present time and m_0 is the initial saturated mass. The results are shown in the graph below for cement mortar and concrete:

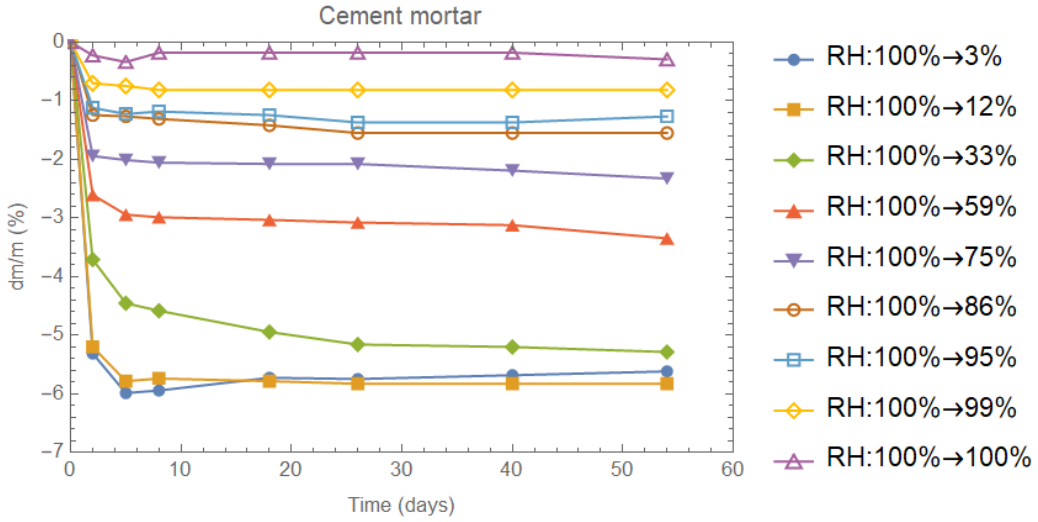

(a)

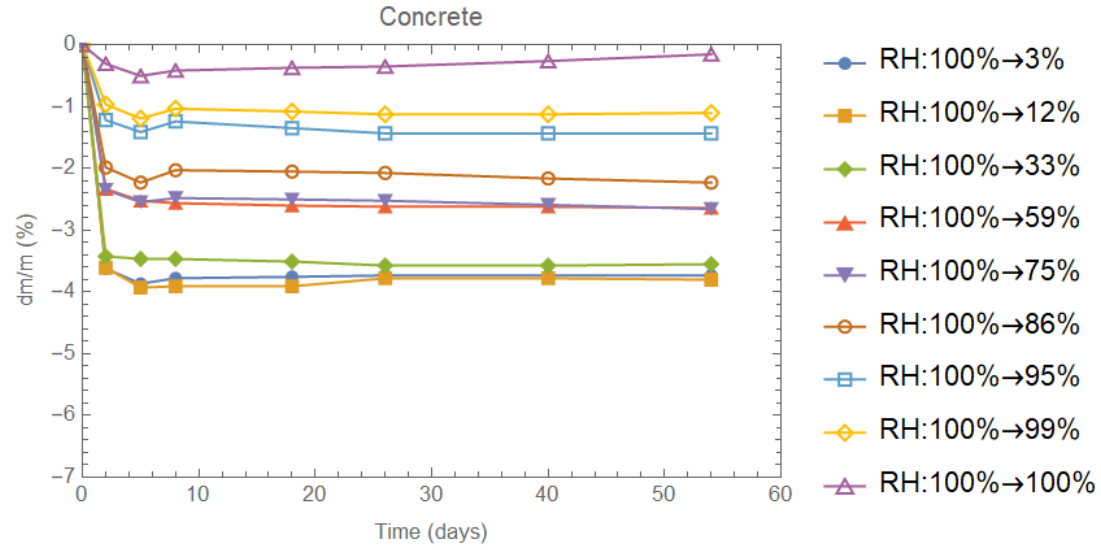

(b)

Figure A- 3 Relative variation in mass with time.

The Figure A- 3 depicts the mas loss curves for cement mortar and concrete subjected to varying RH 100%→3%. It can be noticed that there is a maximum of 6%

mass loss for cement mortar at the lowest RH environment, whereas the maximum mass loss for concrete at that RH is 4%. Another observation is that the change in mass loss occurs within the first few days and thereafter shows an asymptotic curve.

The saturation degree is defined as the ratio of the volume occupied by water to the volume occupied by pores. The degree of saturation can be expressed as:

$$S = \frac{m_{RH} - m_{OD}}{m_{SSD} - m_{OD}} \tag{52}$$

where m_{RH} is the equilibrium mass of sample at particular relative humidity, m_{SSD} is the mass of sample at saturated surface dry state and m_{OD} is the mass of sample at oven dried state. The equation yields single data point for each RH. The desorption isotherm of cement mortar and concrete is shown in Figure A- 4.

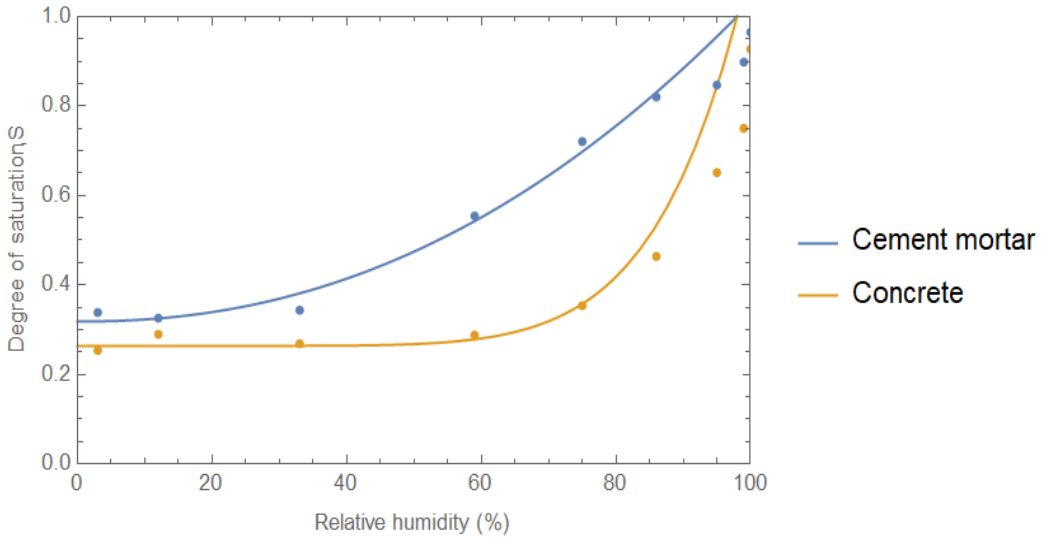

Figure A- 4 Desorption isotherm of cement mortar and concrete.

The degree of saturation curve was fitted with respect to RH following the relation presented by Bazant and Baweja (Bazant and Baweja, 1995):

$$S = 1 - a\left(1 - \frac{RH}{98}\right)^{b} \tag{53}$$

where, a and b are fitting coefficients. The coefficients used in this study are shown in Table A - 2 below:

Table A - 2 Fitting coefficients for Saturation curve as a function of RH.

	Cement Mortar	**Concrete**
a	0.68	0.74
b	2.2	7.7

In the meantime, the mass of the cement mortar and concrete prisms were measured continuously for over a year at different temperatures. Figure A- 5 shows the average mass loss observed over time. Here t represents the present time and t' is the time testing started, i.e., 28 days.

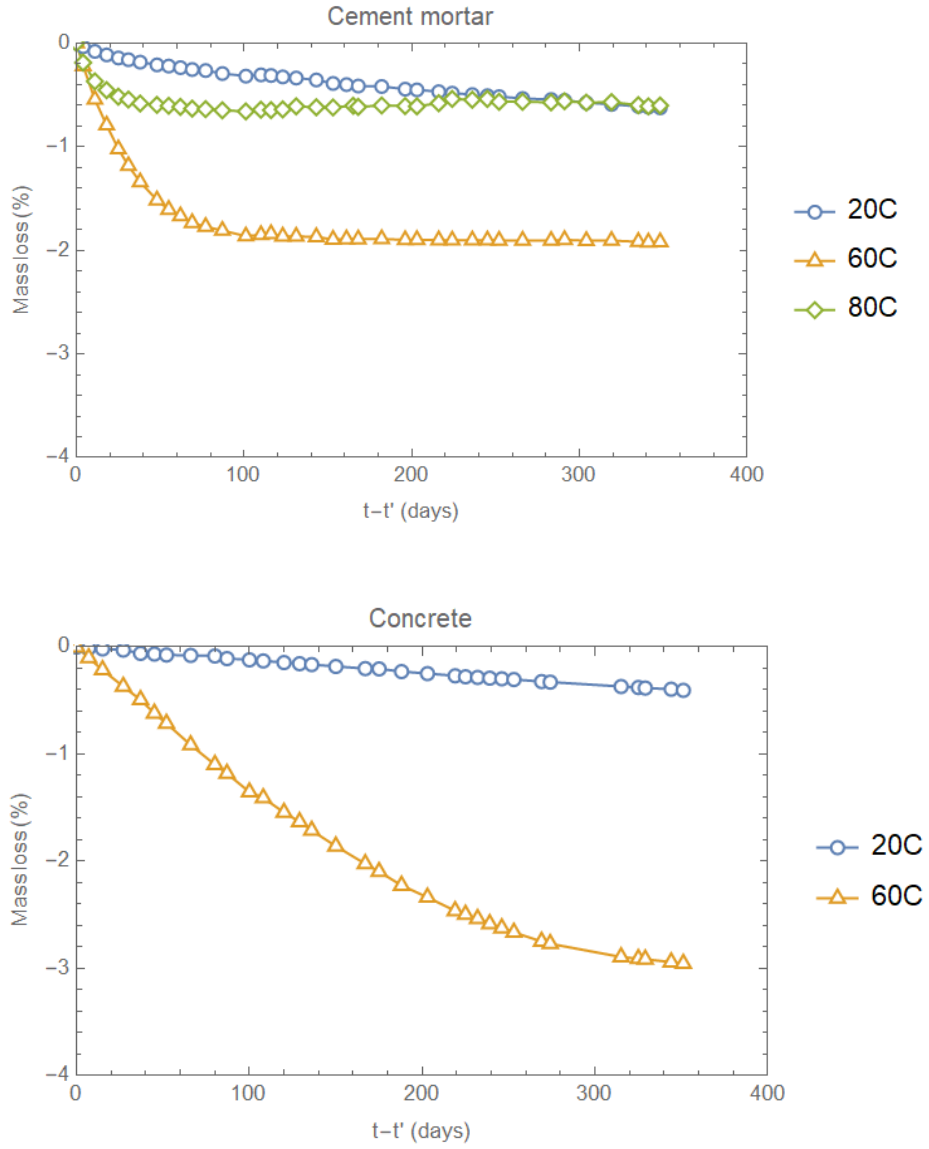

Figure A- 5 Mass loss observed in cement mortar and concrete prisms.

From the graph, it is interesting to note that the mass loss in cement mortar at 60°C is the highest with 1.9% indicating that the samples at that temperature have the least degree of saturation, whereas the mass loss in cement mortar at 80°C is close to 0.7% and comparable to 20°C curve. This could be attributed to the fact that since the readings began

at 28 days, the samples in 80°C underwent significant mass loss initially and started to asymptote after 28 days. To prove this hypothesis, the mass loss curves for all samples from day 1 is shown in Figure A- 6.

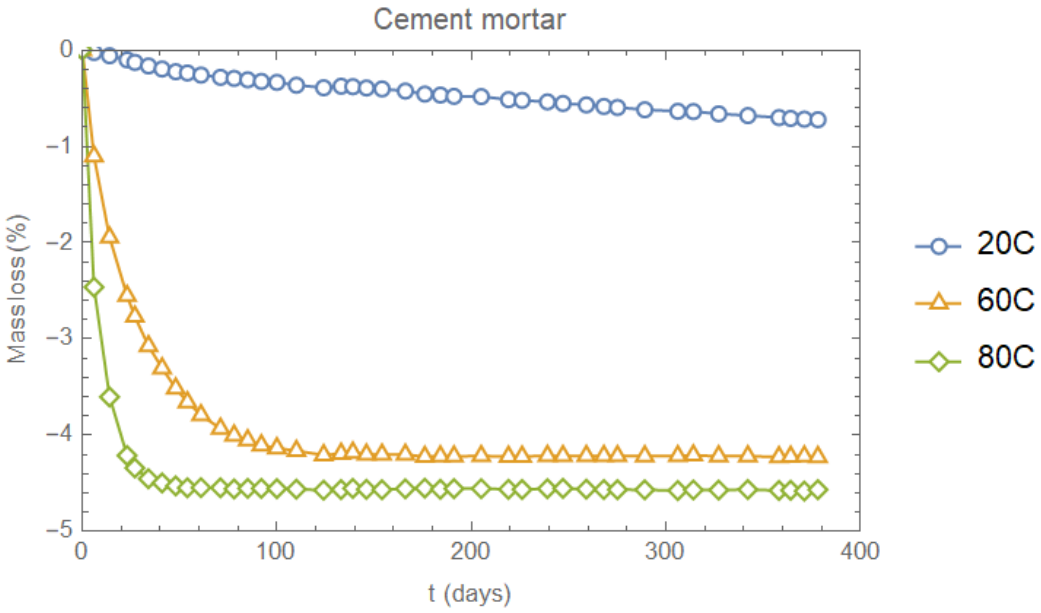

Figure A- 6 Mass loss observed in cement mortar from day 1.

The mass loss in concrete at 60°C is close to 3% compared to mass loss in concrete at 20°C is 0.5%. All the samples were placed in water bath before starting the experiment to record the m_{SSD} and the samples were placed in an oven for 24 hours at the end of the experiment to record the m_{OD}. The mass readings recorded in between these two conditions represent the m_{RH} depending on the humidity levels in the pores. Using eq. (52) the saturation curve with respect to time is obtained.

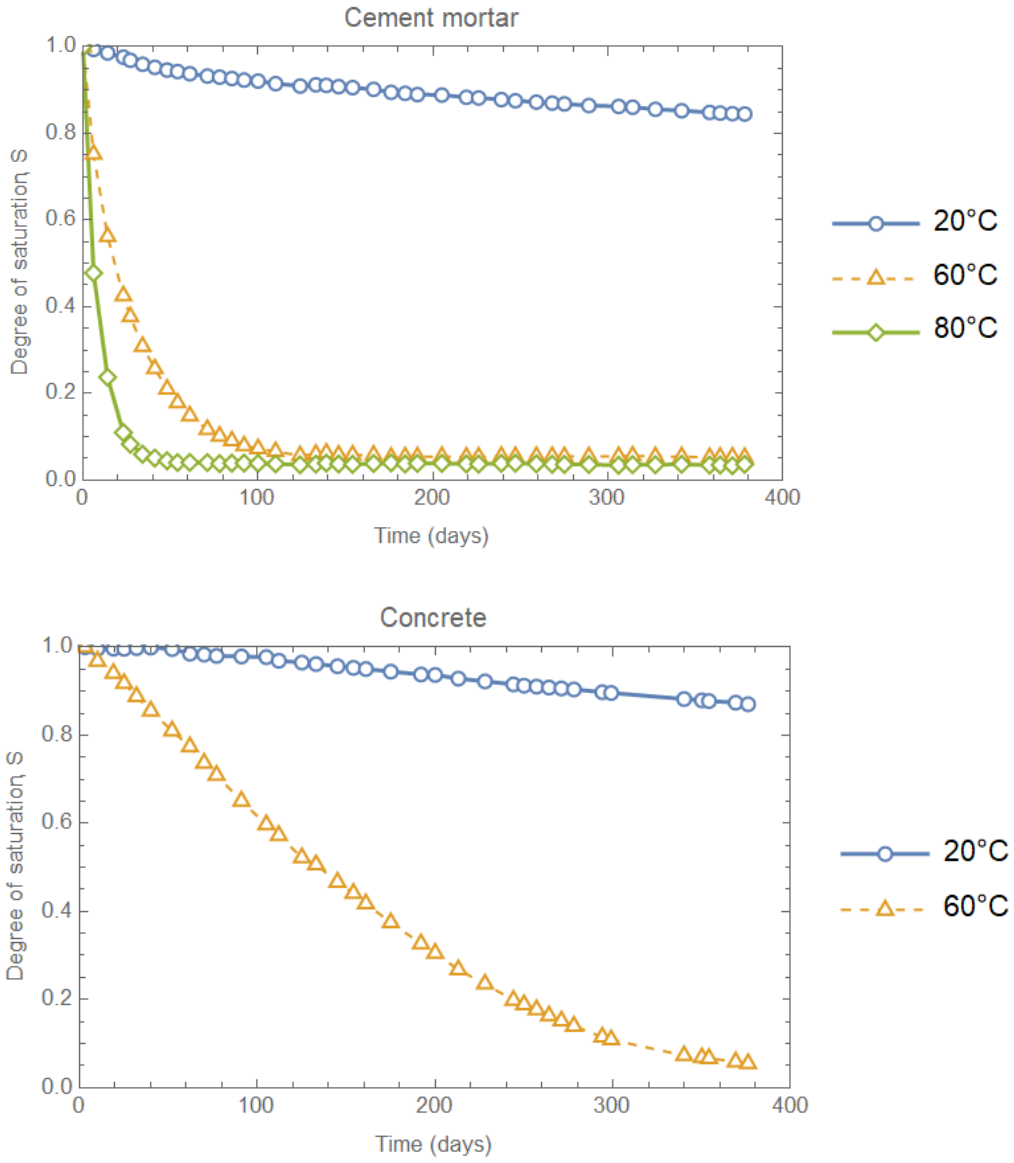

Figure A- 7 Average Degree of Saturation with time.

As expected, the degree of saturation for cement mortar and concrete is low at higher temperatures due to significant drying as well as enhanced hydration reaction at that temperature leading to consumption of water in the pores. Using eq. (53), the

saturation curve is converted to RH curve with respect to time. Figure A- 8 shows the relative humidity profile with time. Few points from the graph to be noted:

1. Since the degree of saturation is close to 0.1 at 60°C and 80°C for cement mortar, the RH inside the pores drops to less than 20%. Since the desorption isotherm curve flattens for saturation below 0.3, the RH profile is assumed to be constant after reaching that value.
2. All the changes in the relative humidity and drying is significant within the first 28 days. That means when the creep tests start after 28 days, the drying creep becomes insignificant and the strain observed in the specimen due to loading is all basic creep.
3. This was the same observation seen in the case of using B3 model which shows a good fit with the experimental results, which illustrates the drying creep component to be very small and negligible at that loading age of samples.
4. In the case of concrete, as the sample sizes are bigger, drying occurs slowly and hence drying may be an issue even after 28 days especially at 60°C. B3 model also suggested the same and hence, the drying creep component was subtracted from the total creep to obtain the basic creep.

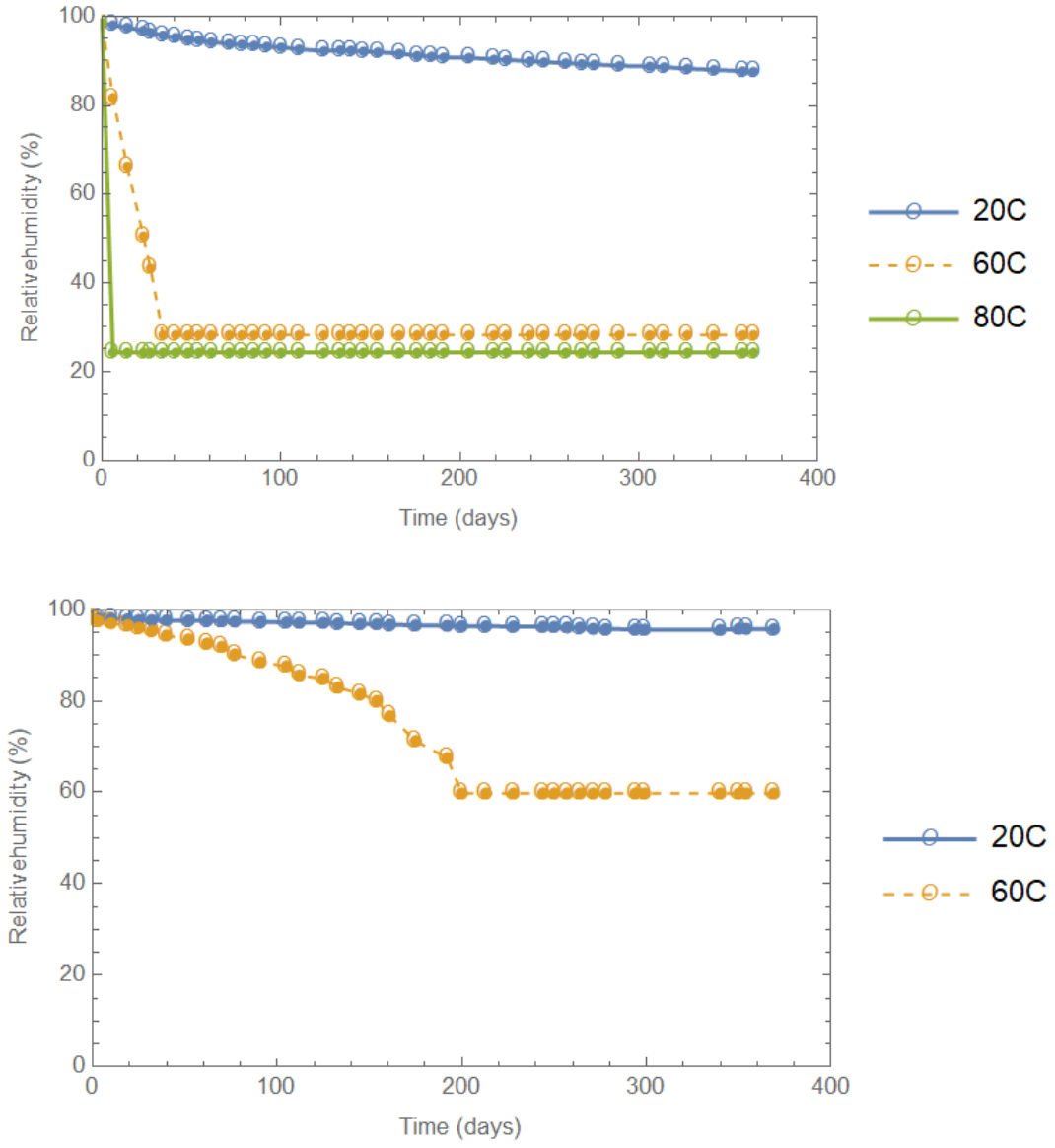

Figure A- 8 Average relative humidity with time.

References

1. Baroghel-Bouny, V., Mainguy, M., Lassabatere, T., and Coussy, O.: Characterization and identification of equilibrium and transfer moisture properties for ordinary and high-performance cementitious materials. Cem. Conc. Res., 29, 1225–1238 (1999).

2. Bazant, Z. P. and Baweja, S.: Justification and refinements of Model B3 for concrete creep and shrinkage. 1. Statistics and sensitivity." Mat. and Struct. 28(181), 415-430 (1995).
3. Daïan, J. F.: Condensation and isothermal water transfer in cement mortar, part I - pore size distribution, equilibrium, water condensation and imbibition. Transp. Por. Media 3(6) 563-589 (1988).
4. Greenspan, L.: Humidity Fixed Points of Binary Saturated Aqueous Solutions. J. Res. Nat. Bureau Stds - A. Physics and Chemistry, 81A (1) pp. 89-96 (1977).
5. Ishida, T., Maekawa, K. and Kishi, T.: Enhanced modeling of moisture equilibrium and transport in cementitious materials under arbitrary temperature and relative humidity history, Cem. Conc. Res. 37(4) 565-578 (2007).
6. Johannesson, B. and Janz, M.: Test of four different experimental methods to determine sorption isotherms. J. Mats. Civ. Eng. 14, 471–477 (2002).
7. Jowitt, R. and Wagstaffe, P. J.: The certification of the water content of microcrystalline cellulose (MCC) at 10 water activities - CRM 302. Luxembourg, Office for Official Publications of the European Communities. 1-54 (1989).
8. Mikhail, R. S. and Oweimreen, G. A.: Surface area and pore structure of compressed low porosity cement pastes. Cem. Conc. Res. 3(5) 561-573 (1973).
9. Sémété, P., Février, B., Le Pape, Y., Delorme, J., Sanahuja, J. and Legrix, A.: Concrete desorption isotherms and pe rmeability determination: effects of the sample geometry. European Journal of Environmental and Civil Engineering. 1-21, 42-62 (2015).

APPENDIX B

DATA ACQUISITION

Vibrating wire gage was used in this study to record strains in the sample. It works on the principle of resonant frequency. The fundamental frequency (resonant frequency) of vibration of wire is given by equation:

$$f = \frac{1}{2L_w}\sqrt{\frac{F}{m}}$$

*w*here,

L_w = length of wire (inches)

F = wire tension (lbs)

M = mass of wire per unit length (lbs) $m = \frac{W}{L_W\, g}$ and $W = \rho a L_w$

where,

W = weight of wire (lbs)

g = acceleration of gravity (386 in./sec^2)

ρ = wire material density (0.283 lb./in.^{3})

a = cross-sectional area of wire (in.^{2})

Combining the equations:

$$f = \frac{1}{2L_w}\sqrt{\frac{Fg}{\rho a}}$$

Tension can be expressed in terms of strain as:

$F = \varepsilon_w E a$

where,

ε = wire strain (in./in.)

E = young's modulus of wire (30 x 10^6 Psi)

Inserting this in the equation and substituting values for E, g and ρ,

$$f = \frac{1}{2L_w}\sqrt{\frac{\varepsilon_w Eg}{\rho}}$$

$$f = \frac{101142}{L_W}\sqrt{\varepsilon_w}$$

The period of vibration, T = $\frac{10^6}{f}$

Therefore,

$$\varepsilon_w = \frac{97.75\ L_w 2}{T^2}$$

The equation must be expressed in terms of strain in the surface of the body to which gage is attached. Since, the deformation in the body is equal to the deformation in the wire,

$$\varepsilon_w L_w = \varepsilon L_g$$

ε = strain the body

L_g = gage length (in.)

Thus,

$$\varepsilon = \frac{97.75\ L_w 3}{T^2\ L_g}$$

For vibrating wire gage model 4202,

L_w = 2 inches

L_g = 2 inches

$$\varepsilon = \frac{391}{T^2}$$

Digits, R = $\frac{f2}{1000}$

Theoretical Gage Factor, G = 0.391

Batch Factor, B = 0.968

$\Delta\mu\varepsilon = (R_1\text{-}R_0) * B * G$

Where,

R_0 = Initial digit reading

R_1 =Subsequent digit reading

All vibrating wire gage is calibrated by the manufactured and a report is generated for each of them as shown below:

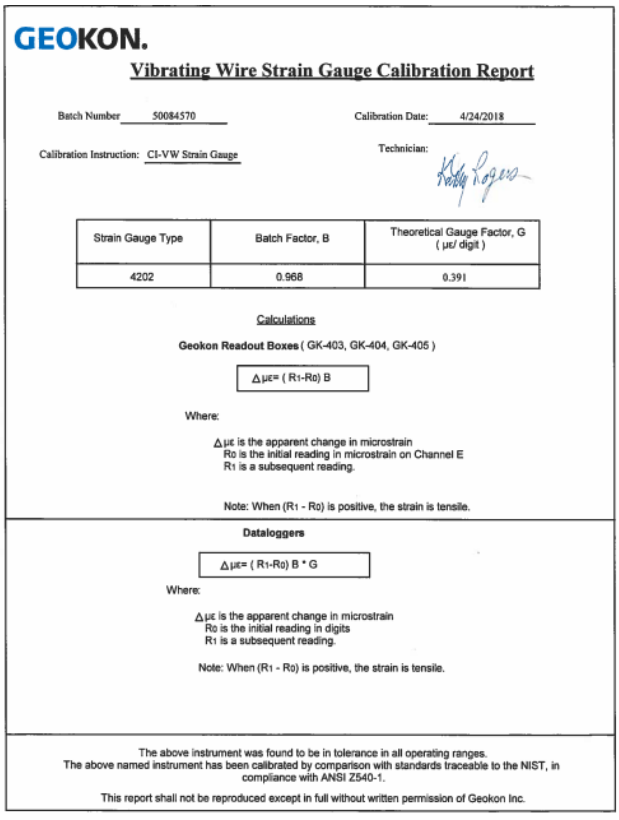

GEOKON.

Vibrating Wire Strain Gauge Calibration Report

Batch Number 50084570 Calibration Date: 4/24/2018

Calibration Instruction: CI-VW Strain Gauge Technician:

Strain Gauge Type	Batch Factor, B	Theoretical Gauge Factor, G (με/ digit)
4202	0.968	0.391

Calculations

Geokon Readout Boxes (GK-403, GK-404, GK-405)

Δμε= (R1-R0) B

Where:

Δμε is the apparent change in microstrain
R0 is the initial reading in microstrain on Channel E
R1 is a subsequent reading.

Note: When (R1 - R0) is positive, the strain is tensile.

Dataloggers

Δμε= (R1-R0) B * G

Where:

Δμε is the apparent change in microstrain
R0 is the initial reading in digits
R1 is a subsequent reading.

Note: When (R1 - R0) is positive, the strain is tensile.

The above instrument was found to be in tolerance in all operating ranges.
The above named instrument has been calibrated by comparison with standards traceable to the NIST, in compliance with ANSI Z540-1.

Figure B - 1 Calibration report of vibrating wire gage from Geokon.

The sensors such as embedded strain gages, foil gages and load cell are connected to a CR 300 datalogger which stores the data in its memory. A CR300 datalogger has three ports to connect to a sensor. It is also Wifi enabled, meaning we can connect to the datalogger from the computer using Loggernet software through Wifi. This is particularly useful, when we have tests running at 60°C in a chamber and it is not necessary to physically be present in the room to connect the datalogger to computer. In order to extend the DAQ to a more number of sensors, AM 16/32B Multiplexer (MUX) was used. The Multiplexer is connected to one of the ports in CR300 and the MUX can connect to 16 sensors. Atmost three MUX can be connected to a CR300 in each of its ports, thus enabling us to connect 48 sensors at a time. Figure B-2, B-3 shows the CR300 and MUX used in the study.

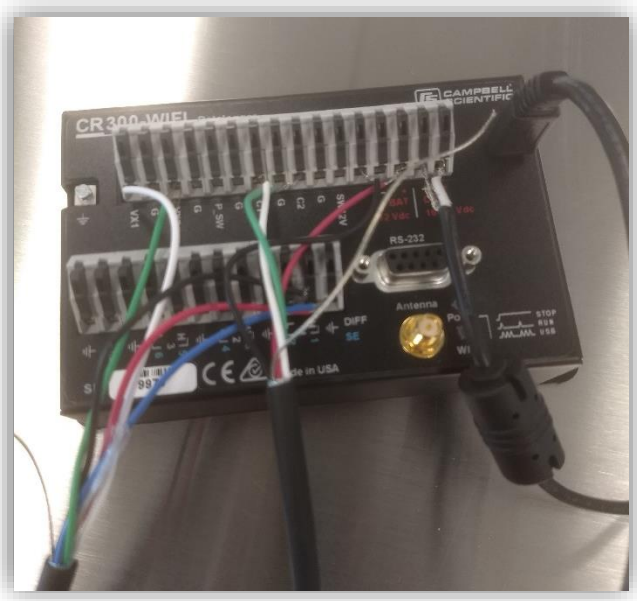

Figure B - 2 CR300 Datalogger.

Figure B - 3 AM16/32B Multiplexer.

NOTE: Load cells have full bridge circuit in them, so they can be connected to a port on the Multiplexer, whereas embedded strain gage or foil gage requires a 4WFBS120 completion module to connect to multiplexer.

In order to connect vibrating wire gage to the datalogger, AVW200 is needed as an intermediate step between the datalogger and multiplexer. AVW200 is equipped to pick up the resonant frequency signals and convert them to digits and strain. It has 2 ports allowing them to connect to 2 MUX and ultimately 32 vibrating wire gages. A picture of it is shown in Figure B-4. The CR300 datalogger stores the data in its memory, and the data can be retrieved once a month or so. The connections needed between each of the data acquisition is shown later in this appendix.

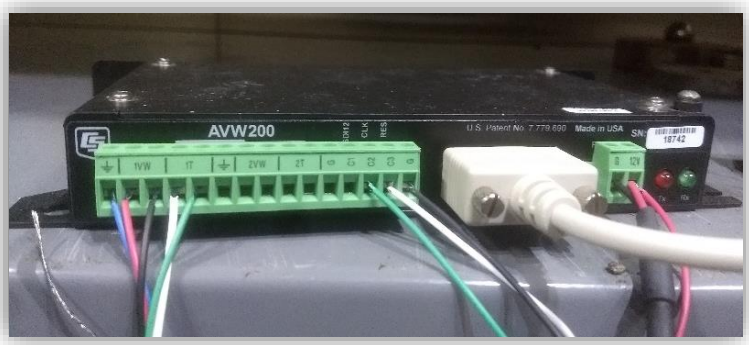

Figure B - 4 AVW200.

In case the sensors are in a concrete block in the field and we do not have access to power, then a battery operated VWAnalyzer can be used to record data from vibrating wire gage. VWAnalyzer contained 5 colored pins to be matched to the same colored wires on the vibrating wire gage sensor. The sensor information can be stored, recorded and retrieved easily using a USB connection. Figure B-5 shows a picture of it.

Figure B - 5 VWAnalyzer.

Another DAQ to record foil gage sensors is using Student D4 from Micro Measurements. This has a complete full bridge in it and the foil gages can be easily connected to the DAQ using RJ45 pins. It gives a direct strain reading using Micro measurements software. Figure B-6 shows the student D4 DAQ.

Figure B - 6 Student D4 DAQ for foil gages.

Wiring diagram

- Step 1: Data Logger CR300 is connected to Multiplexer AM16/32B to increase the number the sensors the data logger can measure

CR300	**AM16/32B**
12V	12V
G	G
C1	CLK
C2	RES

CR300	AM16/32B
1H	COM ODD H
1L	COM ODD L
VX1	COM EVEN H
G	COM G

- Step 2: Embedded strain gages/ Foil gages require completion module 4WFBS120 before connecting to AM16/32B

Foil Gages	4WFBS120
A Common	H
A Common	L
B	G
4WFBS120	**AM16/32B**
_H pin	1H
_L pin	1L
_G pin	G
_Black	2H

- Step 3: Load cells are connected to AM16/32B

Load Cell	AM16/32B
Red	1H
Black	1L
Green	G
White/Yellow	2H

- Step 4: AVW200 will communicate with CR300 through RS232 port using a null modem cable

CR300	AVW200
SW12	12V
G	G
RS232	RS232

- Step 5: AVW200 is connected to Multiplexer AM16/32B to increase the number the sensors the data logger can measure

AVW200	AM16/32B
12V	12V
G	G
C2	CLK

AVW200	AM16/32B
C3	RES
1V+	COM ODD H
1V-	COM ODD L
1T+	COM EVEN H
1T-	COM EVEN L
G	G

- Step 6: Vibrating wire gages are connected to the Multiplexer AM16/32B

AM16/32B	VWG
1H	V+
1L	V-
2H	T+
2L	T-
G	G
3H	V+
3L	V-
4H	T+
4L	T-
G	G

1. **Program for collecting load cells and embedded strain gages data using CR300 and AM 16/32B**

‘3 load cells wired to AM16/32B, and 12 strain gage wired to AM16/32B using 4WFBS120 completion module’

```
Public BattV
Public FCLoaded
Public PTemp_C
Public CReps
Public ZMode
Public QBSSMode
Public CIndex
Public CAvg
Public LCount
Public Strain(12)
Public Vr1000(15)    'VR1000 1-12 are for strain gauges, VR1000 13-15 will hold the load cell readings
Public GFAdj(12)
Public BrZero(12)
Public CKnown(12)
Public GFsRaw(12)={2.1,2.1,2.1,2.1,2.1,2.1,2.1,2.1,2.1,2.1,2.1,2.1}

Public Load_1   :Units Load_1 = lbs     'Load Cell 1 in lbs
Public Load_2   :Units Load_2 = lbs     'Load Cell 2 in lbs
Public Load_3   :Units Load_3 = bls     'Load Cell 3 in lbs


Alias Vr1000(13) = LoadCell_1
```

```
Alias Vr1000(14) = LoadCell_2
Alias Vr1000(15) = LoadCell_3

DataTable(Table1,True,-1)
  Sample(1,PTemp_C,FP2)
  Sample(1,Strain(1),IEEE4)
  Sample(1,Vr1000(1),IEEE4)
  Sample(1,Strain(2),IEEE4)
  Sample(1,Vr1000(2),IEEE4)
  Sample(1,Strain(3),IEEE4)
  Sample(1,Vr1000(3),IEEE4)
  Sample(1,Strain(4),IEEE4)
  Sample(1,Vr1000(4),IEEE4)
  Sample(1,Strain(5),IEEE4)
  Sample(1,Vr1000(5),IEEE4)
  Sample(1,Strain(6),IEEE4)
  Sample(1,Vr1000(6),IEEE4)
  Sample(1,Strain(7),IEEE4)
  Sample(1,Vr1000(7),IEEE4)
  Sample(1,Strain(8),IEEE4)
  Sample(1,Vr1000(8),IEEE4)
  Sample(1,Strain(9),IEEE4)
  Sample(1,Vr1000(9),IEEE4)
  Sample(1,Strain(10),IEEE4)
  Sample(1,Vr1000(10),IEEE4)
  Sample(1,Strain(11),IEEE4)
  Sample(1,Vr1000(11),IEEE4)
  Sample(1,Strain(12),IEEE4)
  Sample(1,Vr1000(12),IEEE4)
```

```
  Sample (1,Load_1,IEEE4)
  Sample (1,Load_2,IEEE4)
  Sample (1,Load_3,IEEE4)
EndTable

DataTable(Table2,True,-1)
        DataInterval(0,1440,Min,10)
        Minimum(1,BattV,FP2,False,True)
EndTable

'Calibration history table
DataTable(CalHist,NewFieldCal,10)
  SampleFieldCal
EndTable

BeginProg

  SW12 (1 )      'turn on power to mux, not enough room in the Batt+ for both wires

  Delay (0,500,mSec)      'delay for mux power up

  'Initialize calibration variables for
  'Quarter Bridge Strain, 3-wire 120 ohm with 4WFBS120 TIM measurement 'Vr1000()'
  CIndex=1 : CAvg=1 : CReps=12
  For LCount = 1 To 12
    GFAdj(LCount)=GFsRaw(LCount)
  Next

  'Load the most recent calibration values from the CalHist table
```

```
FCLoaded=LoadFieldCal(True)

Scan (30,Min,3,0)

  LCount=1

  MuxSelect(C1,C2,5,1,1) ' selects the mux to channel 4 in B Mode

  SubScan (0,mSec,15)    ' the first 12 subscans will measure strain guages, the next three will measure load cells

    BrFull(Vr1000(LCount),1,mv34,1,Vx1,1,2500,True,True,1000,60,1,0)

   PulsePort(C1,5000) ' advance the mux

   LCount=LCount+1

  NextSubScan

  PortSet(C2,0)'turn off mux

  Delay(0,150,mSec)

  'Calculated strain result 'Strain' for
  'Quarter Bridge Strain, 3-wire 120 ohm with 4WFBS120 TIM measurement 'Vr1000'
  StrainCalc(Strain(),12,Vr1000(),BrZero(),-1,GFAdj(),0)
  'Quarter bridge strain shunt calibration for
  'Quarter Bridge Strain, 3-wire 120 ohm with 4WFBS120 TIM measurement 'Vr1000'
```

```
FieldCalStrain(13,Strain(),1,GFAdj(),0,QBSSMode,CKnown(),CIndex,CAvg,GFsRaw()
,0)
   'Zeroing calibration for
   'Quarter Bridge Strain, 3-wire 120 ohm with 4WFBS120 TIM measurement 'Vr1000'
   FieldCalStrain(10,Vr1000(),CReps,0,BrZero(),ZMode,0,CIndex,CAvg,0,Strain())

   'Convert Load Cell reading to lbs
    Load_1 = ((Vr1000(13))+0.014)/-0.0009    'Aishwarya came up with the relationship
(voltage + 0.014)/-0.0009 the 2.5
    Load_2 = ((Vr1000(14))+0.012)/-0.0009            'cancels out the reference portion of
a full bridge measurement
    Load_3 = ((Vr1000(15))+0.0165)/-0.0009
    Load_4 = ((Vr1000(11))+0.0008)/0.0003
    Load_5 = ((Vr1000(12))+0.0044)/0.0003
    Load_6 = ((Vr1000(10))+0.0008)/0.0003



   CallTable Table1
   CallTable Table2
   CallTable CalHist

 NextScan

EndProg
```

2. Program for collecting Vibrating Wire gage data using AVW200

```
Added AVW200 with mux and 4 VW sensors;
```

```
'load cells wired into AM16/32B.
'AVW200 instructions, AVW200 will communicate over the CR300's RS232 port with a null modem cable (pn 18663)

Public BattV
Public FCLoaded
Public PTemp_C
Public CReps
Public ZMode
Public QBSSMode
Public CIndex
Public CAvg
Public LCount
Public j
Public Strain(4)
Public Vr1000(10)    'VR1000 1-13 are for strain gauges, VR1000 14-16 will hold the load cell readings
Public GFAdj(4)
Public BrZero(4)
Public CKnown(4)
Public GFsRaw(4)={2.1,2.1,2.1,2.1}

Public Dst(9,6)       'VW variable array
Public result(9)      'AVW result code

Public Load_60C_1   :Units Load_60C_1 = lbs     'Load Cell 1 in lbs
Public Load_60C_2   :Units Load_60C_2 = lbs     'Load Cell 2 in lbs
Public Load_60C_3   :Units Load_60C_3 = bls     'Load Cell 3 in lbs
Public Load_80C_1   :Units Load_80C_1 = lbs     'Load Cell 2 in lbs
```

```
Public Load_80C_3   :Units Load_80C_3 = lbs     'Load Cell 3 in lbs
Public Load_60C_4   :Units Load_60C_4 = lbs     'Load Cell 4 in lbs

Alias Vr1000(5) = LoadCell_60C_1
Alias Vr1000(6) = LoadCell_60C_2
Alias Vr1000(7) = LoadCell_60C_3
Alias Vr1000(8) = LoadCell_80C_1
Alias Vr1000(9) = LoadCell_80C_3
Alias Vr1000(10) = LoadCell_60C_4

DataTable(Mux_1,True,-1)
  DataInterval (0,1,Hr,10)
  Sample(1,PTemp_C,FP2)
  Sample(1,Strain(1),IEEE4)
  Sample(1,Vr1000(1),IEEE4)
  Sample(1,Strain(2),IEEE4)
  Sample(1,Vr1000(2),IEEE4)
  Sample(1,Strain(3),IEEE4)
  Sample(1,Vr1000(3),IEEE4)
  Sample(1,Strain(4),IEEE4)
  Sample(1,Vr1000(4),IEEE4)
  Sample (1,Load_60C_1,IEEE4)
  Sample (1,Load_60C_2,IEEE4)
  Sample (1,Load_60C_3,IEEE4)
  Sample (1,Load_80C_1,IEEE4)
  Sample (1,Load_80C_3,IEEE4)
  Sample (1,Load_60C_4,IEEE4)
EndTable
```

```
DataTable (AVW200_Data,1,-1) 'stores data from both VW sensors into a table named AVW200
  DataInterval (0,1,Hr,10)
  Sample (6,Dst(1,1),IEEE4)
  Sample (6,Dst(2,1),IEEE4)
  Sample (6,Dst(3,1),IEEE4)
  Sample (6,Dst(4,1),IEEE4)
  Sample (6,Dst(5,1),IEEE4)
  Sample (6,Dst(6,1),IEEE4)
  Sample (6,Dst(7,1),IEEE4)
  Sample (6,Dst(8,1),IEEE4)
  Sample (6,Dst(9,1),IEEE4)
EndTable

DataTable(Daily,True,-1)
  DataInterval(0,1440,Min,10)
  Minimum(1,BattV,FP2,False,True)
  Maximum (1,BattV,FP2,False,False)
  Minimum (1,PTemp_C,FP2,False,False)
  Maximum (1,PTemp_C,FP2,False,False)
EndTable

'Calibration history table
DataTable(CalHist,NewFieldCal,10)
  SampleFieldCal
EndTable

BeginProg
```

```
SW12 (1 )      'turn on power to mux, not enough room in the Batt+ for both wires
SerialOpen (ComRS232,38400,0,0,0)    'config com port for AVW200
Delay (0,500,mSec)      'delay for mux power up
'Initialize calibration variables for
'Quarter Bridge Strain, 3-wire 120 ohm with 4WFBS120 TIM measurement 'Vr1000()'
CIndex=1 : CAvg=1 : CReps=4
For LCount = 1 To 4
  GFAdj(LCount)=GFsRaw(LCount)
Next
'Load the most recent calibration values from the CalHist table
FCLoaded=LoadFieldCal(True)

Scan (1,Hr,3,0)

  LCount=1
  MuxSelect(C1,C2,5,1,1) ' selects the mux to channel 4 in B Mode

  SubScan (0,mSec,16)    ' the first 13 subscans will measure strain guages, the next
three will measure load cells

    BrFull(Vr1000(LCount),1,mv34,1,Vx1,1,2500,True,True,1000,60,1,0)
    PulsePort(C1,5000) ' advance the mux
    LCount=LCount+1

  NextSubScan

  PortSet(C2,0)'turn off mux
  Delay(0,150,mSec)
```

```
    'Calculated strain result 'Strain' for
    'Quarter Bridge Strain, 3-wire 120 ohm with 4WFBS120 TIM measurement 'Vr1000'
    StrainCalc(Strain(),4,Vr1000(),BrZero(),-1,GFAdj(),0)
    'Quarter bridge strain shunt calibration for
    'Quarter Bridge Strain, 3-wire 120 ohm with 4WFBS120 TIM measurement 'Vr1000'

FieldCalStrain(13,Strain(),1,GFAdj(),0,QBSSMode,CKnown(),CIndex,CAvg,GFsRaw()
,0)
    'Zeroing calibration for
    'Quarter Bridge Strain, 3-wire 120 ohm with 4WFBS120 TIM measurement 'Vr1000'
    FieldCalStrain(10,Vr1000(),CReps,0,BrZero(),ZMode,0,CIndex,CAvg,0,Strain())

    'Convert Load Cell reading to lbs
    Load_60C_1 = Vr1000(5)/-0.0009    'Aishwarya came up with the relationship
(voltage + 0.014)/-0.0009 the 2.5
    Load_60C_2 = Vr1000(6)/-0.0009            'cancels out the reference portion of a full
bridge measurement
    Load_60C_3 = Vr1000(7)/-0.0009
    Load_80C_1 = Vr1000(8)/0.0009
    Load_80C_3 = Vr1000(9)/0.0009
    Load_60C_4 = (Vr1000(10)+0.0044)/0.0003

'Result,comport,neighbor,PBA,Dst,chan,muxchan,reps,begFreq,endFreq,Vx,Integration
Time,Mult,Offset,sensor 1-4, channel 1
    For j = 1 To 9 Step 1
    AVW200(result(j),ComRS232,0,200,Dst(j,1),1,j,1,450,3500,1,_60HZ,1,0)
    Next j

    CallTable Mux_1
```

```
    CallTable Daily
    CallTable CalHist
    CallTable AVW200_Data

  NextScan

EndProg
```

APPENDIX C

LOAD CELL CALIBRATION

Before utilizing the load cells, they have to be calibrated to understand the relation between the load applied and the output voltage. Hence, here all ten load cells were calibrated and the relation between load and voltage is shown in the graphs below.

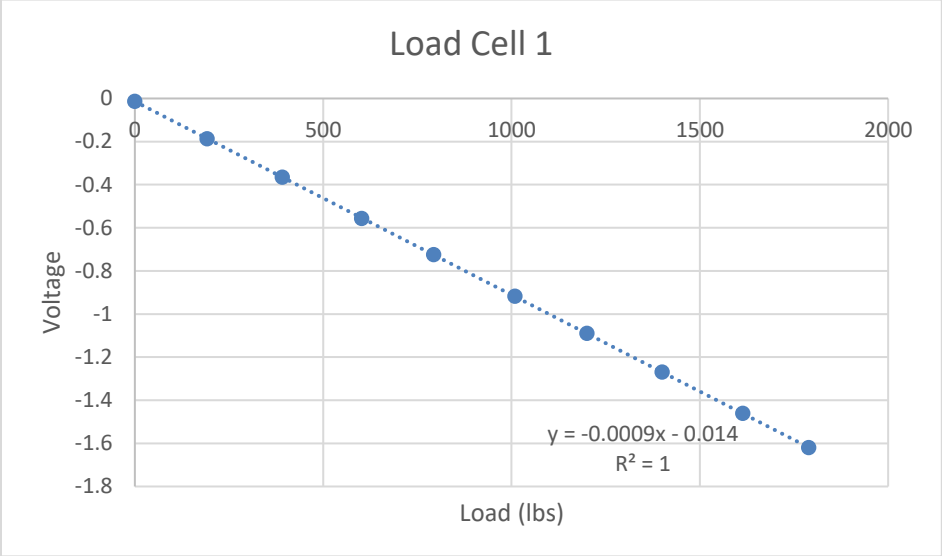

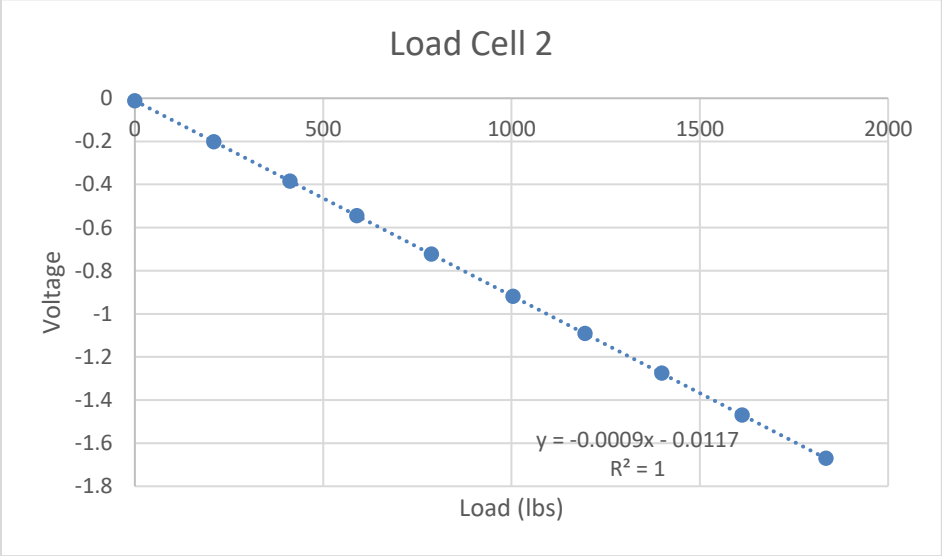

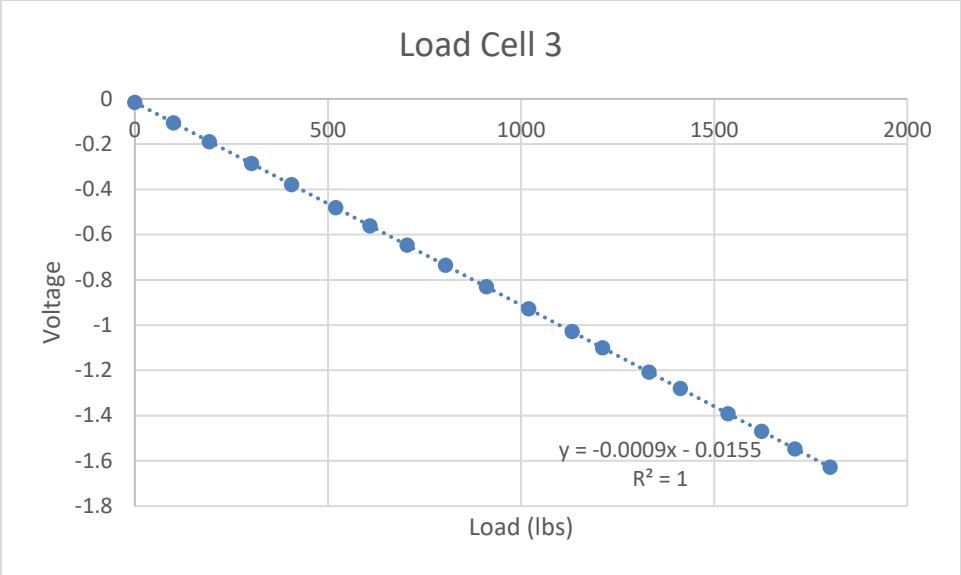
Load Cell 3
0
-0.2
-0.4
-0.6
-0.8
-1
-1.2
-1.4
-1.6
-1.8
Voltage
0
500
1000
1500
2000
Load (lbs)
y = -0.0009x - 0.0155
R² = 1

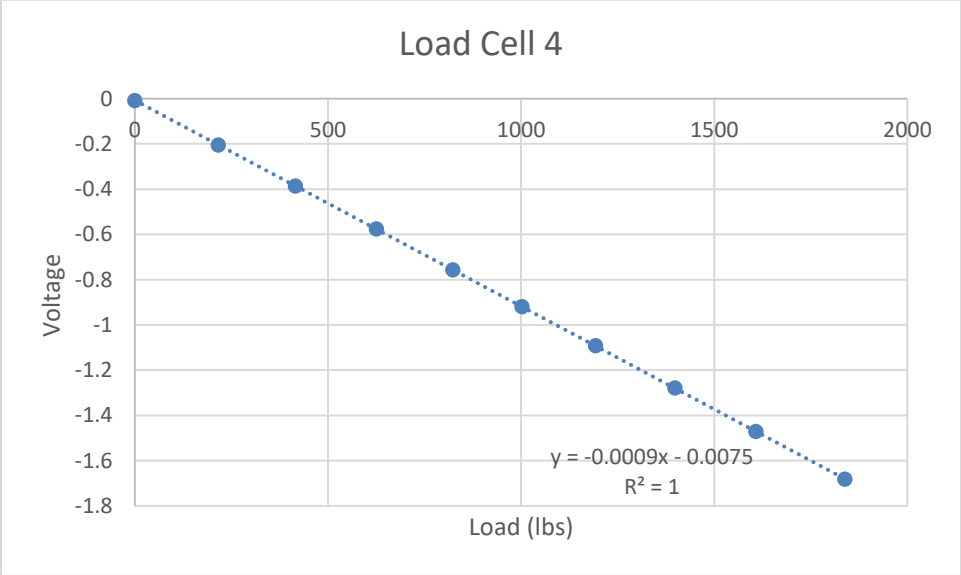
Load Cell 4
0
-0.2
-0.4
-0.6
-0.8
-1
-1.2
-1.4
-1.6
-1.8
Voltage
0
500
1000
1500
2000
Load (lbs)
y = -0.0009x - 0.0075
R² = 1

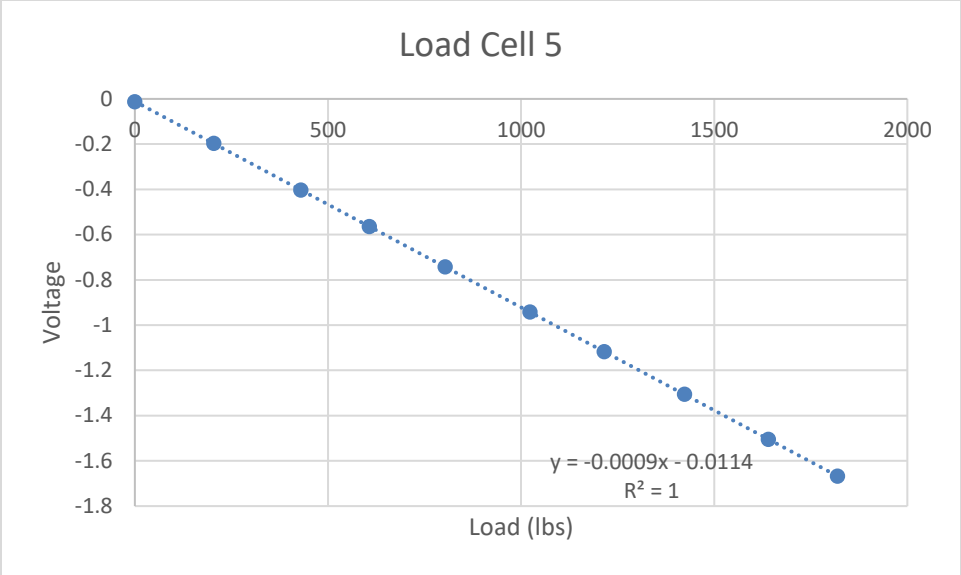
Load Cell 5
0
-0.2
-0.4
-0.6
-0.8
-1
-1.2
-1.4
-1.6
-1.8
Voltage
0
500
1000
1500
2000
Load (lbs)
y = -0.0009x - 0.0114
R² = 1

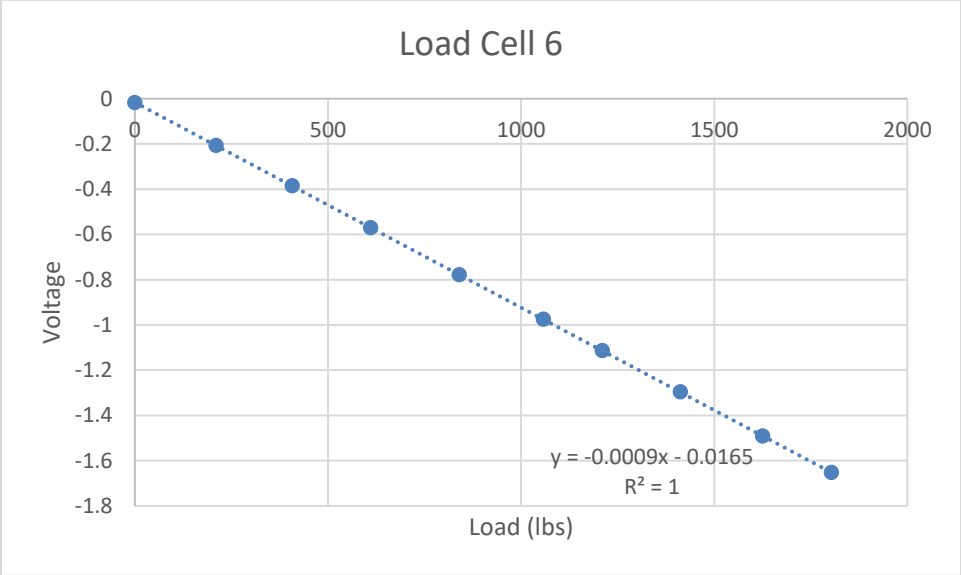
Load Cell 6
0
-0.2
-0.4
-0.6
-0.8
-1
-1.2
-1.4
-1.6
-1.8
Voltage
0
500
1000
1500
2000
Load (lbs)
y = -0.0009x - 0.0165
R² = 1

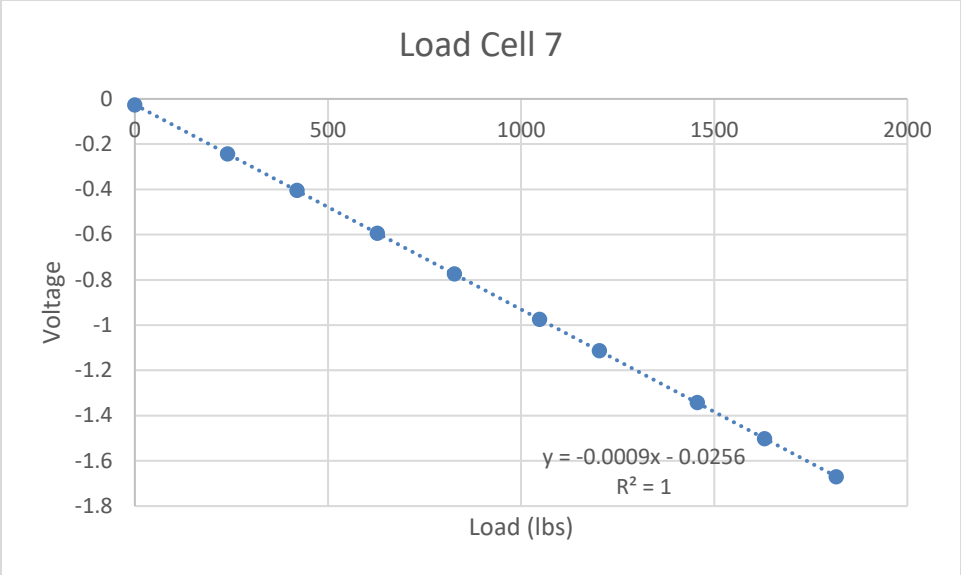
Load Cell 7
0
-0.2
-0.4
-0.6
-0.8
-1
-1.2
-1.4
-1.6
-1.8
Voltage
0
500
1000
1500
2000
Load (lbs)
y = -0.0009x - 0.0256
R² = 1

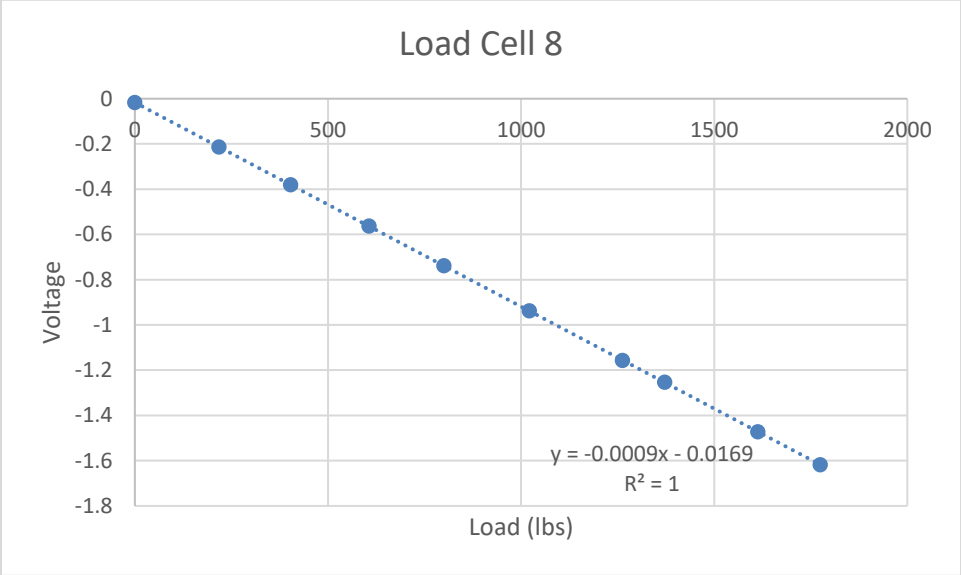
Load Cell 8
0
-0.2
-0.4
-0.6
-0.8
-1
-1.2
-1.4
-1.6
-1.8
Voltage
0
500
1000
1500
2000
Load (lbs)
y = -0.0009x - 0.0169
R² = 1

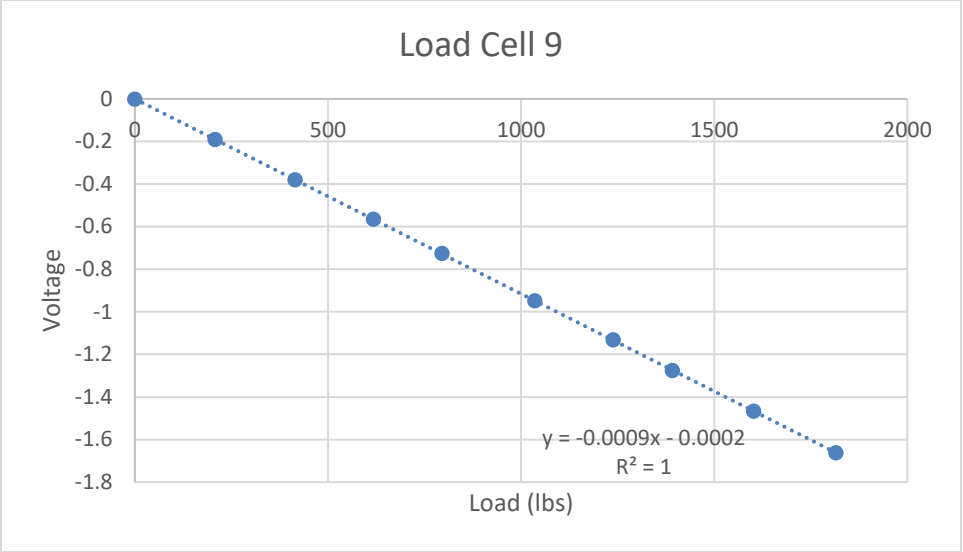
Load Cell 9
0
-0.2
-0.4
-0.6
-0.8
-1
-1.2
-1.4
-1.6
-1.8
Voltage
0
500
1000
1500
2000
Load (lbs)
y = -0.0009x - 0.0002
R² = 1

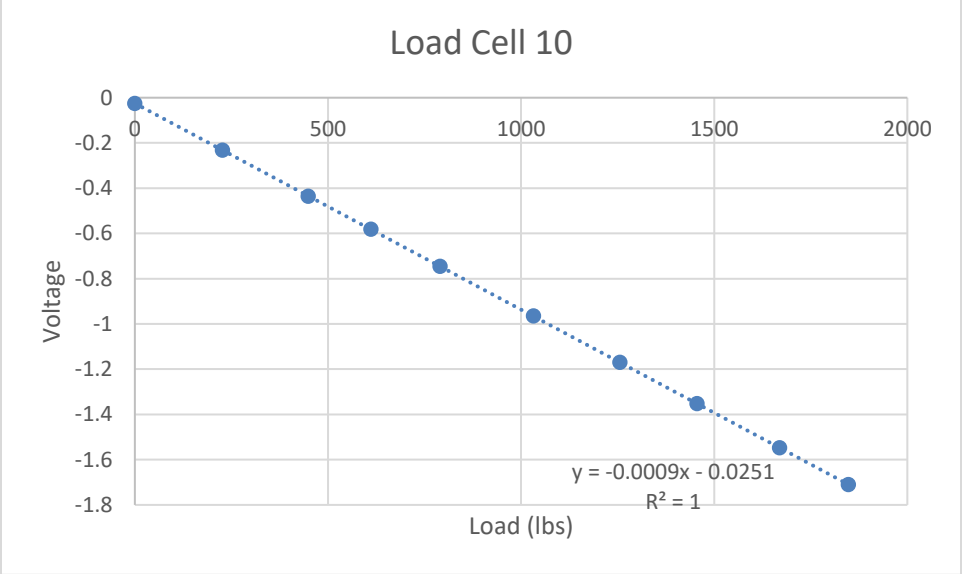
Load Cell 10
0
-0.2
-0.4
-0.6
-0.8
-1
-1.2
-1.4
-1.6
-1.8
Voltage
0
500
1000
1500
2000
Load (lbs)
y = -0.0009x - 0.0251
R² = 1